Mn^{2+} in semiconductor nanocrystals

Vladimir A Vlaskin

A dissertation
submitted in partial fulfillment of the
requirements for the degree of

Doctor of Philosophy

University of Washington
2014

Reading Committee:
Daniel Gamelin, Chair
David Ginger
Dennis Heinekey

Program Authorized to Offer Degree:
Chemistry

University of Washington

Vladimir A Vlaskin

Mn^{2+} in semiconductor nanocrystals

Abstract

The following chapters describe the state of II-VI semiconductor nanocrystal preparation. Introduction of transition metal dopants gave rise to new materials and provided an insight into both physical and chemical properties of these semiconductor nanocrystals. Mn^{2+} and Co^{2+} dopants were used to probe the spatial position of an exciton inside Mn^{2+}:ZnSe/CdSe core/shell nanocrystals and to show that p-d exchange still dominates s-d exchange, consistent with bulk analogues. Energy transfer between Mn^{2+} and excitonic states in Mn^{2+}:ZnSe/CdZnSe with various compositions was shown to result in temperature dependent dual emission. The use of multishell ZnS/CdS/ZnS heterostructures, were shown to give both stability against chemical degradation and allowed tunability of the excitonic states. The discovery of a method to completely suppress Ostwald ripening at temperatures that still allow cations to assume their thermodynamic distributions inside the samples has laid the first step in the coming revolution of nanocrystal synthesis. Independent control over morphology and composition has settled the debate on “doping impossibility” and nanocrystals seen through the new Overton window can be placed in a dynamic equilibrium with their environment.

Table of Contents

Page

Chapter 3: Tunable Dual Emission in Doped Semiconductor Nanocrystals

Chapter 4: ZnS/CdS/ZnS Multishell Heterostrucutres; A New Generation of Dual Emitting Nanocrystals

Chapter 5: Doping Nanocrystals by Diffusion

List of Figures

Figure number Page number

Chapter 1: Introduction II-VI Semiconductor Nanocrystals

1.1 Uniform II-VI semiconductor nanocrystals: existence and uniqueness

One of the greatest achievements of the 20th century had been the discovery of quantum mechanics, the development of the theoretical machinery to understand it, and the inevitable resignation to the minds of fysicists. Recent advances in manipulation and characterization of materials at the nanometer scale have created the field of nanotechnology, where chemists control the quantum states and poke them with spins. The revolutionary breakthrough in preparation of nanoscale semiconductors took place in the late 1980's in the Brus and later in the Bawendi groups, establishing methods for obtaining colloidal nanometer sized CdSe crystallites of narrow monodispersity.[1-3] The qualitative difference between the new syntheses that have laid the foundation for the next 20 years and those that came before was the size and shape uniformity of the resulting nanoparticles. These structures are only one step away from the world of elements, where uniformity is a physical property, making them subject to statistics of large numbers that smear the quantum into the classical. Uniformity is what separates an ensemble of quantum objects from very fine dust. Energy transfer between the electric field and an exciton in a semiconductor, is completely determined by the environment of the electron/hole pair that constitutes the exciton. In this quantum confined regime, size and shape of the nanoscale semiconductor become the dominant terms in the Hamiltonian describing the exciton. Size dependent absorption and emission spectra of these nanocrystalites were a striking demonstration of excitonic quantum confinement.[4]

1.2 The general synthetic problem within the rapidly evolving field

Spontaneous crystal formation from elemental precursors dissolved in solution leads to a large distribution of crystal morphologies in the resulting precipitate. Controlling this process is the general problem of nanoscale synthesis and can be divided into two stages, nucleation and growth.[5] The most common strategy applied for the synthesis of II-VI semiconductor nanocrystals involves rapid mixing of two hydrophobic solutions segregating the anionic and cationic precursors at a high temperature, a process that has become known as "the hot injection". At the moment of mixing, the system far from equilibrium, begins to evolve in the direction dominated by processes with the lowest activation barriers. The activation barrier for crystal nucleation is high because of the instability of small clusters, which makes the successful nucleation event contingent of the formation of a large number of new bonds faster than dissolution. The nucleation stage is thus restricted to a short time interval immediately after mixing. More precise control over nucleation is often achieved by using chelating ligands, such as carboxylic and phosphonic acids that have a high affinity for the cation precursor, thus driving the nucleation equilibrium toward dissolution. Once the ensemble of nanocrystals is established in the nucleation stage a significantly more diverse growth stage begins. This stage consists of a series of equilibria describing the dynamic distribution of cationic and anionic precursors and

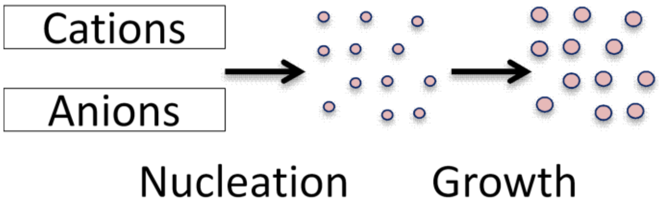

Scheme 1. The "hot injection", nucleation and growth stages.

ligands bearing an array of functional groups mediating these transfers between the nanocrystal surface and solution.[8]

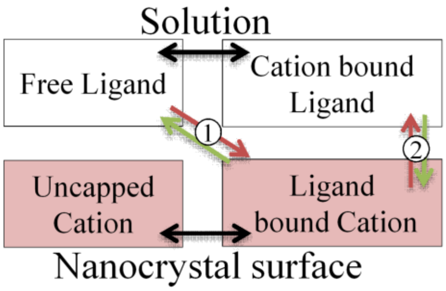

Scheme 2. The processes affecting crystal growth. Equilibrium (1) is the deposition(red) and dissociation(green) of ligands from the surface. Equilibrium (2) is the deposition(green) and dissociation(red)of a ligand together with a cation. There exists a completely analogous set of equilibria for anions, together these determine whether nanocrystals grow or dissolve.

Steps necessary for growth, such as the dissociation of a cationic precursor from a ligand are slow at room temperature, thus the growth stage can be terminated or attenuated at any point when the ensemble of nanocrystals possesses the desired properties.

1.2.A. Diffusion and reaction limited growth

Diffusion limited growth, where concentration of precursors in solution is high relative to the equilibrium value, occurs early in the growth stage and can be prolonged with the addition of precursors following the nucleation event.[6,7] The precursors are rapidly transfered onto the growing nanocrystals from solution, resulting in the formation of a depletion layer in direct proximity to the nanocrystal surface. Under these conditions size focusing can be achieved, driven by faster growth rates of smaller nanocrystals in the ensemble. Under usual conditions both dissolution and deposition rates for a given nanocrystal are proportional to its surface area. In the presence of the depletion layer the deposition rate is directly proportional to the radius of the nanocrystal, consequently dissolution increases more rapidly with increasing radius than deposition. This nanocrystal ensemble behavior is known as “focusing”.

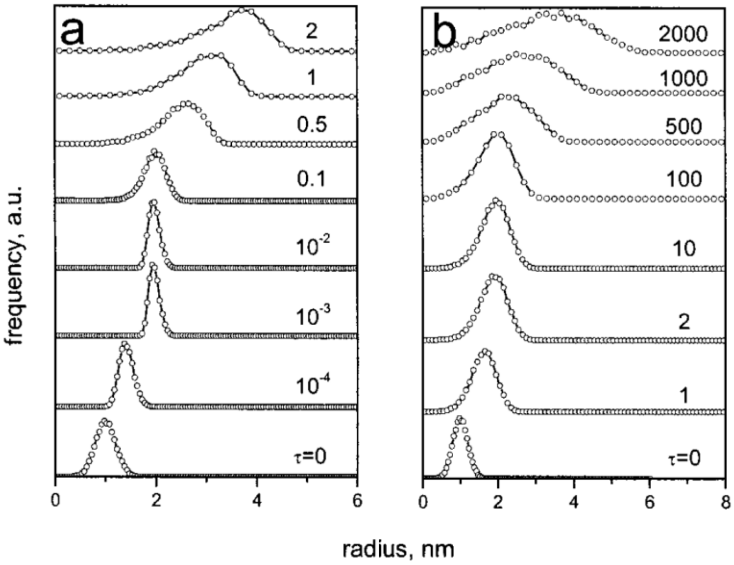

Figure 1.1 Evolution of the nanocrystal ensemble under diffusion (a) and reaction (b) limited growth conditions. Figure adapted from Ref. 7

In the event that the nanocrystal ensemble is not kinetically trapped and the growth stage is allowed to proceed indefinitely, precursor concentrations in solution reach their equilibrium values. During reaction limited growth, deposition and dissolution continue as precursors are randomly shuttled between individual nanocrystals resulting in increased ensemble inhomogeneity. In contrast to the size focusing regime described above, Ostwald ripening, driven by the faster growth rate of the larger nanocrystals in the ensemble, leads to a broadening of the size distribution. The increased stability of substituent ions found in the internal volume, relative to the surface of the nanocrystal, leads to preferential dissolution of nanocrystals with a large surface to volume ratio, as explained by Wilhelm Ostwald in 1901.[9]

1.2.B. Synthetic control by mediating ligands

The major parameter space available, that has proven to be an effective mediator of nanocrystal nucleation, growth and post-processing, are the functional groups on the ligands selected for a given set of nanocrystals, these mediate the majority of chemical processes that can take place. Tri-alkylphosphines are the most ubiquitous ligands, present in the majority of syntheses over the last 20 years.[10] These have the ability to bind both anionic and cationic precursors as well as the nanocrystals themselves. Tri-alkylphosphines have been employed for two major reasons, to reduce elemental sulfur and selenium to the S^{2-} and Se^{2-} anion precursors and to eliminate excitonic traps, presumably via a reduction of an oxidizing species on the surface of the nanocrystal. As phosphines are oxidized the resulting phosphine oxides continue to ligate cations in solution and the surface of the nanocrystals.

Trioctylphosphine/trioctylphosphine oxide ligand combination has been the mainstay in the field popularized by M.G. Bawendi since his work in the Brus group in 1989.[11] The early search for hydrophobic Cd^{2+} precursors converged on dimethyl cadmium, a highly toxic chemical which greatly limited the number of research laboratories able to produce high quality particles. Eventually negatively charged ligands such as n-alkyl phosphonic acid and long chain fatty acids were used to dissolve cadmium oxide at elevated temperatures, the resulting hydrophobic solutions have became the most popular Cd^{2+} precursors used in a variety of syntheses.[12] Owing to their strong binding of cations, these ligands have a significant effect on the equilibria governing both nucleation and growth even at low concentrations, at higher concentrations these can completely prevent nanocrystal nucleation and represent the most potent drivers of ensemble evolution. The synthesis of CdSe nanocrystals of a pure wurtzite crystal structure, the thermodynamically stable phase, is a striking example of thermodynamic control, where growth temperature and phosphonic acid concentration are simultaneously increased.[13] At the maximum temperature of 380°C, above which ligands readily degrade, the ensemble evolution of CdSe nanocrystals is still precisely controlled by phosphonic acids.

In 2001 D.V. Talapin and coworkers showed that addition of hexadecylamine to the trioctylphosphine/trioctlyphosphine oxide ligand mixture improved both, monodispersity and excitonic luminescence quantum yields in the resulting nanocrystals.[14] With a few notable exceptions amine and phosphine ligands have always been used together with ligands that have a higher affinity for cations and are able to solubilize them in a hydrophobic solution. The two effects these ligands have during the reaction, are to make the environment more reducing, which increases the concentration of anions in solution and on the surface of the growing nanocrystals and to scavenge protons off of acidic functional groups activating them toward cations located in solution and on the surface of the growing nanocrystals. Long chain amines and tri-alkyl phosphine oxide ligands have often been used as solvents in syntheses that require the equilibrium to be shifted toward deposition, their inability to strongly bind the cations prevents them from dissolving the nanocrystals faster than they are formed. Syntheses that require deposition to completly dominate dissolution, as is the case for doping and nanoscale heterostructure fabrication, employ non-coordinating solvents such as 1-octadecene.

1.3 Morphology control

1.3.A The core/shell motif, distinguishing the carriers

In order to achieve precise control over both nucleation and growth it became necessary to separate these stages into two different solutions. This multistep synthesis gave rise to the core/shell concept and was naturally generalized to produce nanoscale heterostructures, by employing precursors for different materials during the core and the shell formation.[15] The use of wider band gap CdS, ZnSe and ZnS semiconductors as the shell material relative to the CdSe cores, translated into major improvements in excitonic quantum yields and stability over bare core CdSe nanocrystals. Added resistance to oxidation afforded by replacing Se^{2-} with S^{2-}, near the surface of the nanocrystal increased longevity and greatly expanded the set of possible environments where the nanocrystals could retain their physical properties. The use of wider band gap materials for the shell decreased the amplitude of excitonic wave functions near the surface, decreasing the likelihood of charge and/or energy transfer to an outside species.

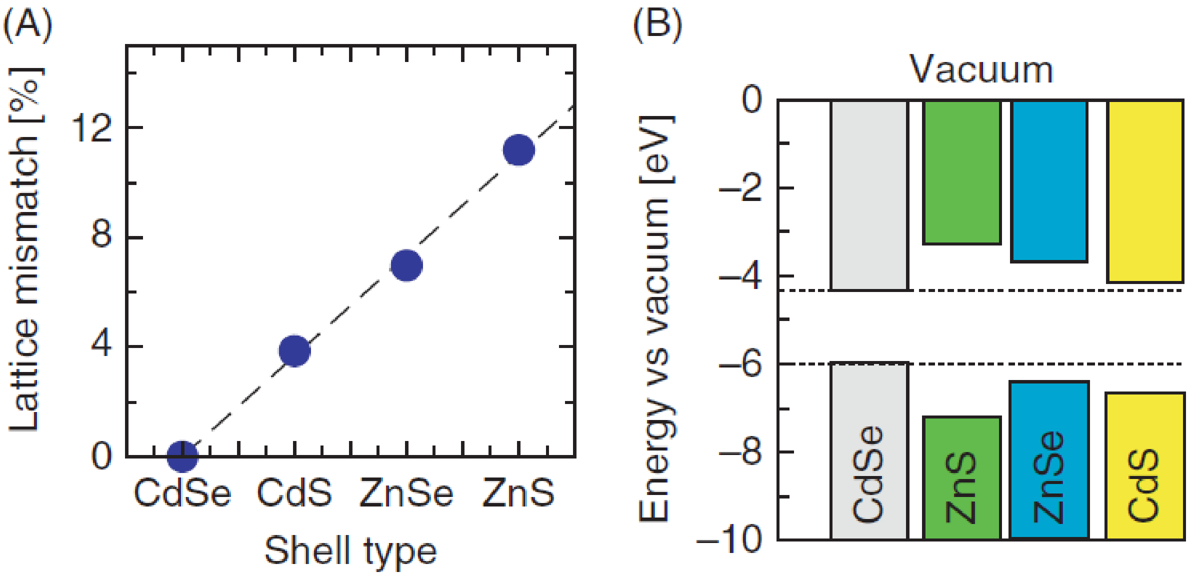

Figure 1.2. (A) Percent lattice miss-match relative to CdSe for common shell materials. (B) Relative bulk conduction band and valence band off-sets . Figure adapted from Ref. 15

Potential energy surfaces inside a nanocrystal composed of two different semiconductor materials are different for the electron and the hole. ZnSe/CdSe core/shell nanocrystals where the electron gains nearly 1 eV of stabilization in the CdSe shell, with the potential barrier for the hole an order of magnitude smaller, exhibit excitonic luminescence life times that increase by an order of magnitude for nanocrystals with core/shell dimensions that result in maximum separation between the carriers.[16] Type II core/shell nanocrystals, such as CdTe/CdSe,[17] ZnTe/ZnSe[18] and CdS/ZnSe[19] where the relative potential energy surfaces are such that the electron and the hole are stabilized on opposite sides of the core/shell interface, have also exhibited increased excitonic emission life times.

1.3.B. Kinetic control through temperature or ligands, anisotropic deposition

The switch from isotropic to anisotropic deposition of CdS onto CdSe nanocrystals with a wurtzite crystal structure has been achieved by a decrease in the reaction temperature from 200°C to 130°C, with an aspect ratio of 3:1 in the resulting nanorods.[20]

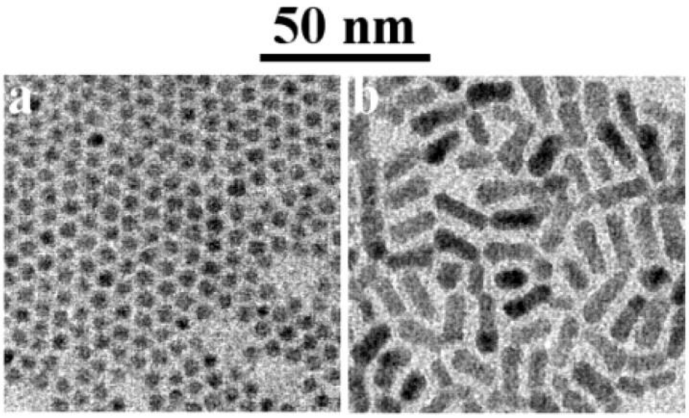

Figure 1.3. (a) CdSe nanocrystals used as cores for (b) CdSe/CdS nanorods. Figure adapted from Ref. 20.

Existence of this deposition mode demonstrates that nanocrystal growth is not simply proportional to the surface area of the nanocrystal. Various facets on the surface of the nanocrystals bear elements of variable valency translating into unique reactivity toward capping ligands and precursors in solution.[13] Cations on the surface of crystal facets perpendicular to the unique axis in wurtzite nanocrystals are able to make three bonds with the underlying layer, which is composed entirely of anions. In contrast, cations on the surface of other crystal facets are able to bond to only two anions of the underlying layer. Consequently, chelating ligands such as phosphonic and fatty acids preferentially bind to cations on the surface of crystal facets not perpendicular to the unique axis. In other words, equilibrium (1) in Scheme 2 is position dependent on the surface of the nanocrystal.

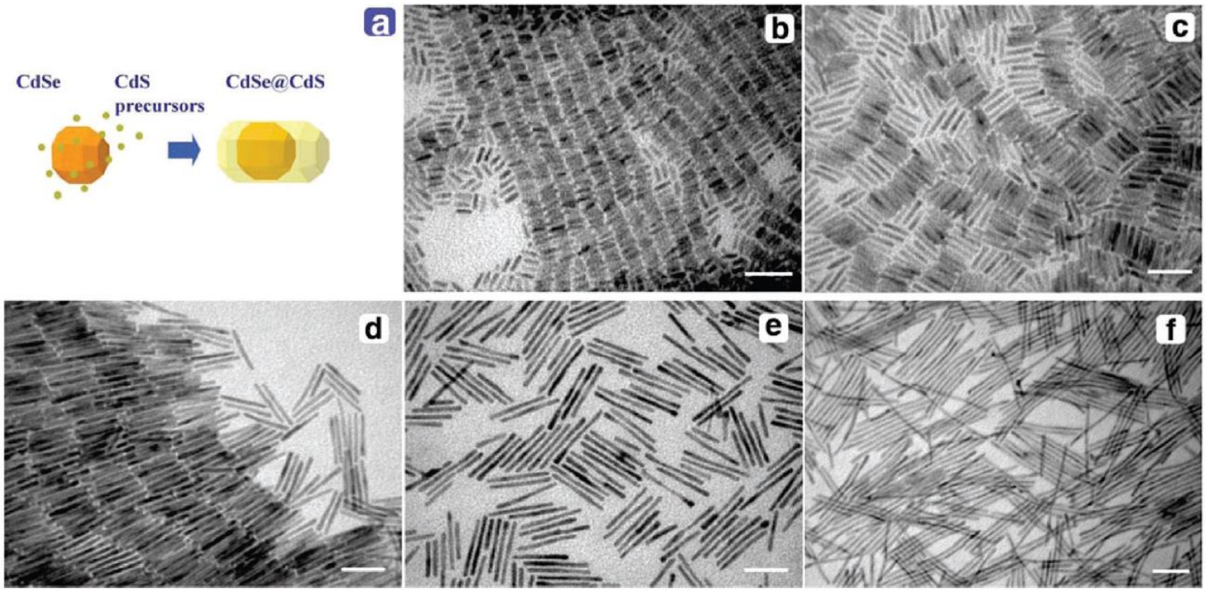

Figure 1.4. High aspect ratio CdSe/CdS nanorods grown at 380°C. Figure adapted from Ref. 13.

Furthermore displacement of these ligands, a critical step for further crystal growth, requires the formation of bonds to anions in the outermost layer that has not yet been formed. Saturating these facets with a mixture of short and long chain phosphonic acids, L. Carbone et. al. achieved precise control over surface reactivity synthesizing highly uniform rods, with 50:1 aspect ratios.[13,21] The resulting nanostructures were either rods or tetrapods, seeded by either wurtzite or zinc blende nanocrystals respectively.[2]

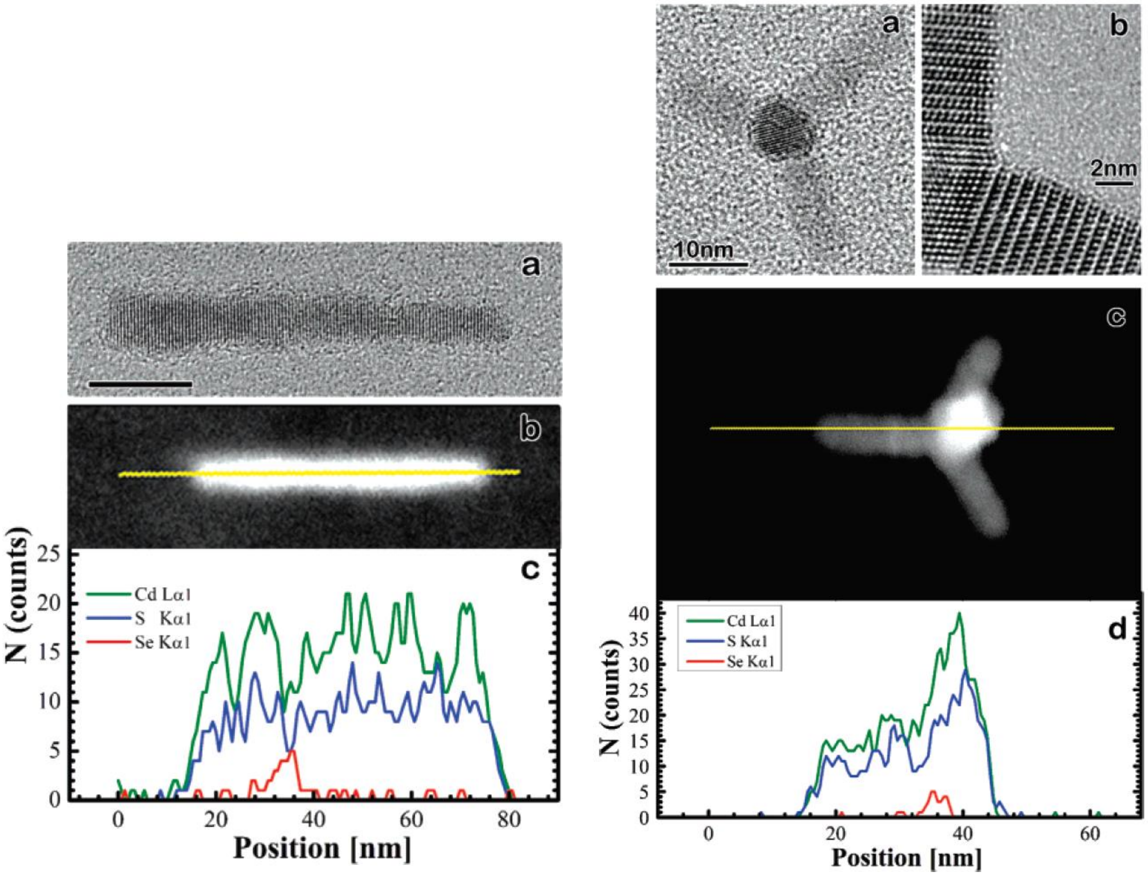

Figure 1.5. CdSe/CdS nanords seeded by wurtzite CdSe(Left Panel). CdSe/CdS tetrapods seeded by zinc blende CdSe(Right Panel). Transmission electron microscopy (TEM) of these nanocrystals (Top). High-angle annular dark field (HAADF), with area of elemental analysis shown with the yellow line (Middle). Elemental composition determined from energy dispersive X-ray intensities. Figure adapted from Ref. 21.

Such a striking connection between morphology and crystal structure is consistent with the chelating ligand mechanism outlined above, as zinc blende nanocrystals possess multiple facets perpendicular to a direction of alternating layers of anions and cations. The total number of rods formed from the surface of zinc blende CdTe nanocrystals was shown to progressively increase in number from two to three to four as the average diameter of the seed nanocrystals was increased from 2.6 nm to 5.0 nm. Strong correlation between morphology of the nanostructure produced with crystal structure and size of the seeding material allows a high level of synthetic control.[23] However, this control is contingent on a level of structural purity and monodispersity of the seeding material that is not necessarily produced by the majority of synthetic procedures available today.

Phosphonic acid mediated seeded growth of various heterostructures has been confirmed for all combinations of ZnSe, ZnTe, CdSe and CdTe as the seed and CdS, CdSe and CdTe as the rod material.[22] Optimal reaction temperatures for rod formation increased with decreasing reactivity of the anionic precursor, with the low of 300°C for CdTe and a high of 380°C for CdS. It is notable that ZnSe and ZnTe are not suitable for rod formation under these conditions. Comparing bond dissociation energies for Zn-Se (136 kJ/mol) and Cd-Se (310 kJ/mol), it is clear that ZnSe undergoes dissolution more readily, an effect further exacerbated by oxygen bearing phosphonic acid ligands, with bond dissociation energies for Zn-O (284 kJ/mol) and Cd-O (142 kJ/mol) consistent with hard/soft acid/base principles.[24] At high temperature, an equilibrium shift toward dissolution significantly increases the number of impacts that nutrients make with the nanocrystal surface for every anion and cation that is eventually incorporated. These conditions do not allow the system to be kinetically trapped, as continuous dissolution and deposition promote formation of the more thermodynamically stable isotropic product with maximized surface to volume ratio.

A 250°C gap in reaction temperature separates the two syntheses that promote the formation of anisotropic, kinetically trapped CdS rods. At 130°C, CdS rod formation took place on the hour time scale, with fresh precursors added slowly during the course of the reaction to maintain their concentrations in solution with the growing nanocrystals close to equilibrium values. Excitonic absorbance spectra showed evidence of a progressive loss of size distribution with time, as expected under reaction limited growth conditions. In a sharp contrast, CdS rod formation at 380°C was complete in 10 minutes, with all precursors and seed nanocrystals rapidly mixed together to start the reaction. Narrow size distributions were achieved under these diffusion limited conditions, and despite the high temperature, the anisotropic product was still kinetically trapped. Preferential ligation of specific crystal facets by phosphonic acid increased the potential barrier for the formation of the isotropic product, which made it possible to run the reaction at a temperature high enough to allow the nutrient concentrations in solution to rapidly reach their equilibrium values. The number of available evolutionary pathways for the ensemble of nanocrystals is inverse to the proximity of the nutrient concentrations in solution to their equilibrium values. Synthetic conditions for rapidly taking a system far from equilibrium to equilibrium, with a fast, precisely controlled initiation, are achieved here using a "hot injection" modified to accommodate nanocrystal seeds. This generalization of the "hot injection" technique should not be dismissed as a matter of convenience in the laboratory, but is a critical component in the overall control of ensemble evolution.

1.4 Nanoscale alloys

1.4.A. The definition problem, between the core/shell and an alloy

Attempts to use precise nanoscale engineering to control the environment of quantum confined excitonic carriers, presented unique conceptual challenges. Identifying a nanoparticle that is ten monolayers thick as either a core/shell or an alloy is not a well defined procedure. There is a distribution of possible levels of alloy homogeneity, given that a significant volume of the nanocrystal can be identified as the interface between the two constituent "pure" materials. Understanding the behavior of this interface under various synthetic conditions for production of nanoscale heterostructures had become important for rationalizing their observed physical properties. Nanocrystaline samples are routinely characterized using x-ray diffraction (XRD) to obtain the crystal structure and alloy composition and transmission electron microscopy (TEM) to determine the size and shape distributions of the ensemble. For a perfectly homogeneous alloy the energy of the exciton is specific to composition and average size of the nanocrystals. For a CdSe/ZnSe core/shell heterostructure excitonic energy is primarily determined by the size of the CdSe core, the red shift observed upon ZnSe shell deposition is small. Monitoring excitonic emission energy of CdSe/ZnSe core/shell heterostructure following 10 minute heat treatments at various temperatures, reveals a sharp alloying point above 270°C.[25] It is important to note that these heat treatments were performed in solutions that contained ligands that could facilitate interparticle nutrient transfer as evidenced by a 10 meV red shift of excitonic emission due to Ostwald ripening.

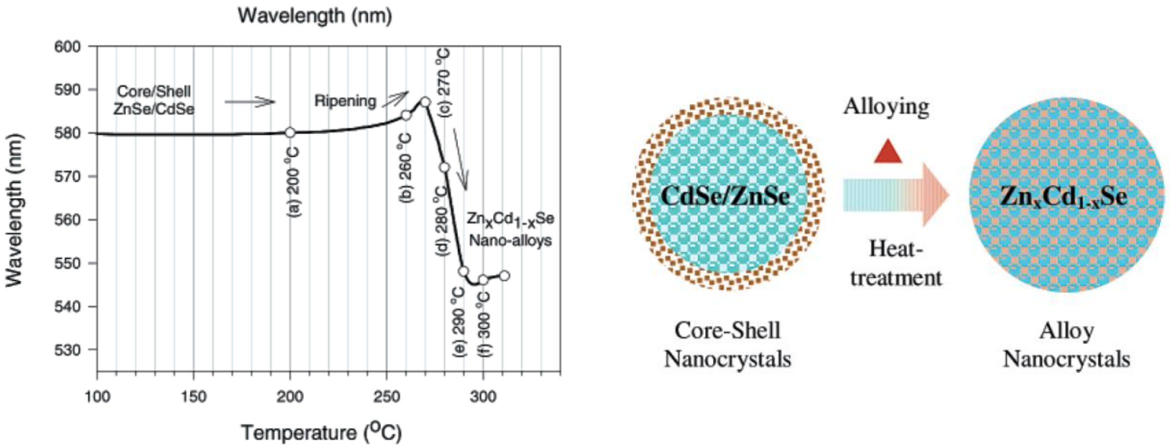

Figure 1.6. Temperature dependent alloying of CdSe/ZnSe core/shell nanocrystals. Figure adapted from Ref. 25.

At various temperatures below 270°C, no major shifts in excitonic energy were observed. At 280°C and 290°C blue shifts of 40 meV and 120 meV respectively were attributed to randomization of cations inside the nanocrystal lattice. Heat treatments above 290°C did not produce larger excitonic blue shifts, implying that complete randomization had been achieved.

This observation of rapid alloy homogenization in the temperature range often used in nanocrystal growth is strong evidence that cations are mobile inside the nanocrystal whose size and shape are defined by the anion lattice. The observation of Ostwald ripening on such short time scales at these temperatures is evidence that equilibrium (2) in Scheme 2 has a significant dissolution component (red arrow). The vision of a nanocrystal under growth conditions that emerges is of a dynamic entity, with cations rapidly cycling between the nanocrystal and solution. This has become known as self-purification of nanocrystals and has far reaching consequences on doping and heterostructure formation.

1.4.B. Solution mediated cation exchange

Exchange of cations between nanocrystals and solution, equilibrium(2) in Scheme 2, is the most important process governing both composition and shape of these nanocrystals, its role in alloying of core/shell heterostructures cannot be ignored. At 220°C cation exchange between ZnSe nanocrystals and a molar equivalent amount of Cd^{2+} in solution has been shown to produce alloys with a 20:1 Cd^{2+} to Zn^{2+} ratio in the nanocrystals.[26,27] A red shift of excitonic absorption and emission features correlated with the expected shift of the XRD pattern for a series of alloys. The initial ZnSe nanocrystals in this study were 3.5 nm in diameter, corresponding to approximately 10 monolayers of ZnSe. In a more recent study it was revealed that 5.7 nm diameter ZnSe nanocrystals do not undergo complete cation exchange under these conditions. Cation exchange at 150°C and 220°C replaced one and two out of five Zn^{2+} cations with Cd^{2+} respectively. Exchange reached its maximum extent on the minute time scale, excitonic energy remained constant on the hour time scale at these temperatures. Addition of more Cd^{2+} to the solution had no effect in cases where maximum alloying extent had already been reached for that temperature. The samples that had reached maximum cation exchange at 220°C were annealed at

250°C for 20 minutes, with an increase of Cd^{2+} to Zn^{2+} cation ratio from 2:5 to 13:7. These observations are explained by dividing the alloying mechanism into two distinct processes. Cation exchange with solution takes places at all temperatures reported, however it is limited to cations that are at or close to the surface of the nanocrystal, with the maximum Zn^{2+} to Cd^{2+} ratios achieved at 220°C consistent with replacement of lightly more than all the cations in the outer most monolayer of a spherical 5.7 nm diameter ZnSe nanocrystal. Given that these nanocrystals are not perfectly spherical with surface to volume ratios higher than the ideal spherical case, it can be assumed that cation exchange stopped once all the Cd^{2+} were depleted from the outermost monolayer.

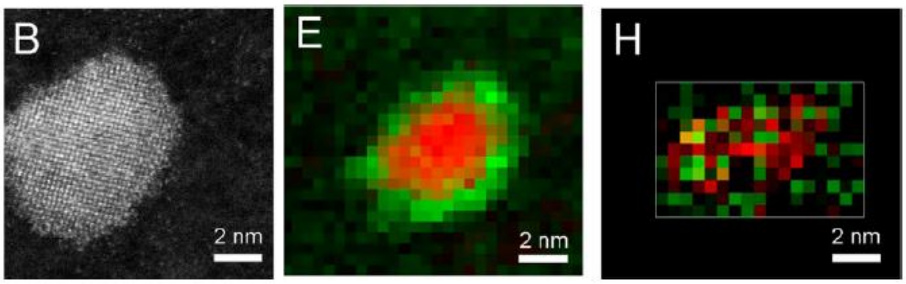

Figure 1.7. TEM of ZnSe/CdSe core/shell (LEFT). Electron energy loss spectroscopy (EELS) derived elemental profile of the nanocrystal shown on the left. Cd and Zn are represented by red and green, respectively. Elemental profile of a ZnSe/CdSe core/shell after 20 minutes at 250°C. Figure adapted from Ref. 26.

Scanning transmission electron microscopy (STEM) coupled with electron energy loss spectroscopy (EELS) spatially resolved the elemental composition of these nanoparticles, showing a clear ZnSe/CdSe core/shell structure. The same analysis performed on the sample annealed at 250°C for 20 minutes, showed a significant degree of cation randomization. As Zn^{2+} in the internal volumes of the nanocrystal are exchanged with surface Cd^{2+}, it becomes available for the faster exchange with the cations in solution.

1.5 Doping II-VI semiconductor nanocrystals

1.5.A. New physical properties through doping

Doping and alloying of nanocrystals are synonyms and are governed by the exact same set of processes. The term “doping” is generally used for impurities that adorn the nanocrystals with qualitatively new physical properties, while the difficulty of doping in relation to alloying also implies that the dopant will be at a low concentration. The unique ability to control energy and spatial distribution of the exciton has placed semiconductor nanocrystal doping at the forefront of scientific research with the promise of new materials and physics.[28] Exciton dopant interactions can be divided into three categories.

The host semiconductor can be used as a sensitizer of the excitonic states of transition metals and lanthanides, exploiting efficient energy transfer from the exciton to the dopant. Tunability of excitonic energy levels by quantum confinement makes it possible to access excitons at energies that are not found in bulk semiconductors, resulting in arrangements of quantum states never before observed. Distinct from energy transfer, charge transfer is a process where the electron or the hole of the exciton reduces or oxidizes the dopant by localizing on it. The decay back to the ground state can occur by reduction or oxidation of the dopant by either the remaining carrier or another species in the environment. Tunability of the excitonic states allows the preparation of electrons and holes of specific energies as well as access to charge transfer transitions not accessible in bulk semiconductors.

The magnetic nature of the exciton allows it to interact with magnetic dopants. Although these perturbations are small in relation to the total energy of the exciton, they carry information about the localization of the exciton within the nanostructure and about the bonding interactions between the host semiconductor and the dopant.

1.5.B. The synthetic challenge, Mn^{2+} doped nanocrystals

Attempts to introduce transition metal dopants into II-VI semiconductor nanocrystals proved to be more challenging than may have been expected based on the vast amount of work done with the analogous bulk materials.[29] Tetrahedral Mn^{2+} became a particularly attractive dopant with extensive studies of its physics in bulk II-VI semiconductors providing a convenient context for interpretation of new results.[30] Incorporation of Mn^{2+} into ZnS[31] and CdS[32] nanoparticles was achieved by addition of Mn^{2+} cations under conditions developed for undoped materials. Mn^{2+} doping of ZnSe and CdSe nanoparticles was not a straight forward extension of previously used synthetic methods, plagued by false positives and Mn^{2+} preferentially residing in solution or the surface of the nanocrystals.[34] At the time that these syntheses were being developed the ability of ZnSe and CdSe nanocrystals to exchange cations with solution had not been appreciated, citing very slow diffusion of Mn^{2+} in bulk CdSe (0.1-0.3 nm per hour).[29] The first report of Mn^{2+} doped ZnSe (Mn^{2+}:ZnSe) nanocrystals described an attempt to shift the equilibrium from solution to the nanocrystals, by removing phosphine oxides and replacing them with amines that have a lower affinity for cations.[33] The maximum Mn^{2+} concentration achieved under these conditions was 0.9%, with an attempt at analogous synthesis of Mn^{2+}:CdSe nanocrystals resulting in 0.14% incorporation.[29] At the highest concentrations Mn^{2+} completely quenched excitonic emission in Mn^{2+}:ZnSe nanocrystals consistent with absence of an undoped subset in the ensemble. The reported concentration of Mn^{2+}:CdSe was so low that a significant fraction of nanocrystals had no Mn^{2+} at all. Even though these initial reports did not end the search for a more effective synthesis of Mn^{2+}:CdSe nanocrystals, the weak-binding hexadecylamine would remain the solvent of choice for future attempts.

1.5.C. The convenient probe, Co^{2+} ligand field

One of the biggest challenges stifling further development of new doping syntheses of nanostructures became sample characterization. The large surface to volume ratio of the nanocrystals provided the dopants with a large number of energetically favorable alternatives to internalization. The most popular and accessible analytical methods were insensitive to the localization of dopants within the sample and became a source of false claims.[34]

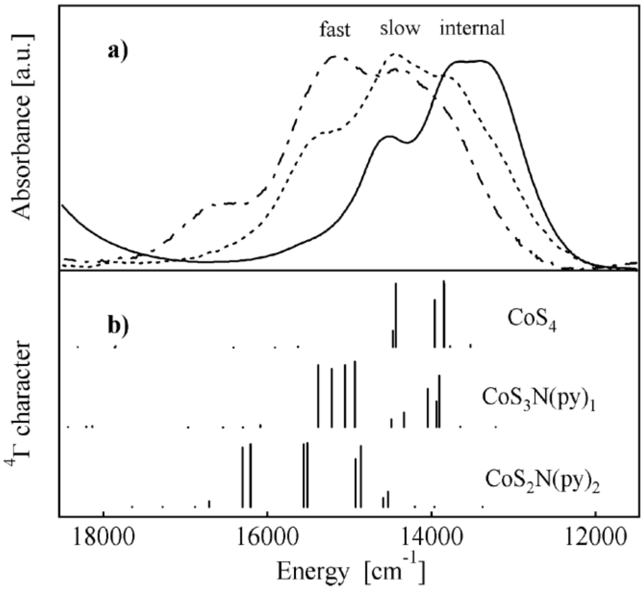

Figure 1.8. Absorbance of $^4A_1 \rightarrow {}^4T_2(P)$ transition of Co^{2+} in different environments. Figure adapted from Ref. 36.

The $^4A_1 \rightarrow {}^4T_2(P)$ ligand field transition of Co^{2+} is a very sensitive to its local bonding environment. Radovanovic P.V. et al. demonstrated the utility of ligand field theory, identifying the various Co^{2+} species present in a sample of nanocrystaline Co^{2+}:CdS, as well as establishing a general procedure for evaluating the effectiveness of various agents for the removal of dopants from the surface of the nanocrystals.[35,36] This work established the unreliability of elemental analysis for the characterization of nanostructures, without meticulous sample purification. In relation to Mn^{2+}, Co^{2+} is a softer Lewis acid, which made it more likely to remain internalized in ZnSe and CdSe nanocrystals under conditions where cation exchange with solution is possible. This relative ease of doping and its unique ability to convey local information from the nanostructures established Co^{2+} as an invaluable tool in nanocrystal doping research.

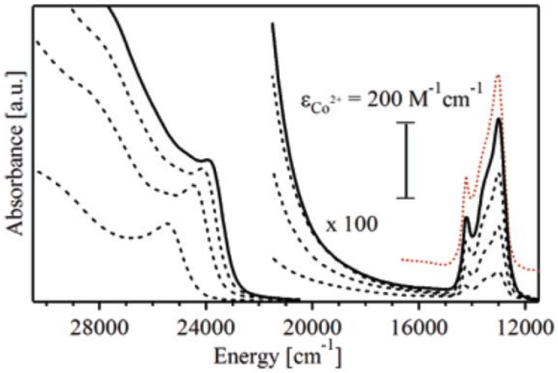

Figure 1.9. Evolving absorbance of Co^{2+} $^4A_1 \rightarrow {}^4T_2(P)$ and the excitonic transition of Co^{2+}:ZnSe nanocrystals as they grow. Figure adapted from Ref. 37.

The conditions chosen for the synthesis of Co^{2+}:ZnSe nanocrystals proved to be seminal for future doping strategies.[37] The choice of a non-coordinating solvent 1-octadecene, the use of a more reactive phosphine, tributylphosphine, a large excess of anionic precursor, the use of a minimal amount of fatty acid to solubilize the cations and the presence of hexadecylamine were all key parameters carried over to future syntheses. Simultaneous monitoring of excitonic and Co^{2+} ligand field transition during growth of the nanocrystals revealed that Co^{2+} incorporation happened only once the nanocrystals reached a critical diameter. This was interpreted as Co^{2+} induced destabilization of small nanoparticles, resulting in their preferential dissolution. The natural corollary to this became the postulation of an undoped core at the nanocrystal center. The existence of this undoped core was also supported by the magnitude of the exchange interaction between Co^{2+} and the exciton, measured using magnetic circular dichroism(MCD) spectroscopy, to be lower than expected based on bulk exchange parameters and the analytical Co^{2+} concentration. The amplitude and sign of the MCD signal was interpreted as the magnitude and ordering of the Zeeman split excitonic states. These splittings are dominated by the exchange interaction with the magnetic dopant and are proportional to the spatial overlap between the exciton and the dopant, making MCD a powerful probe of relative spatial arrangement between the dopants and the exciton in the nanostructure.

The synthesis developed for Co^{2+}:ZnSe nanocrystals was extended to Co^{2+}:CdSe and a series of Co^{2+}:$Zn_{1-x}Cd_xSe$ alloys of different composition.[38] The energy of the excitonic states was raised high enough by quantum confinement in Co^{2+}:CdSe nanocrystals, that for the first time it became possible to observe the Co^{2+} $^4A_1 \rightarrow {}^4T_2(P)$ ligand field transition unobstructed by the excitonic absorption in bulk Co^{2+}:CdSe. The energy position of the $^4A_1 \rightarrow {}^4T_2(P)$ absorption was used to probe the Co^{2+}–Se^{2-} bond-length in Co^{2+}:$Zn_{1-x}Cd_xSe$ alloys throughout the entire range of compositions between the pure endpoints. This analysis revealed a bimodal bond-length distribution inside the nanocrystals with the Cd^{2+}–Se^{2-} and Zn^{2+}–Se^{2-} bond-lengths remaining close to the values found in pure substances, rather than adopting the average bond-length of the alloy, determined by XRD. The formation of this bimodal distribution results from the competition between crystal lattice strain and stabilization due to covalency from bond formation, both of which are bond-length dependent. In the absence of crystal strain, the length of the individual bonds in the alloy would depend only on the identity of the two elements participating in the bond.

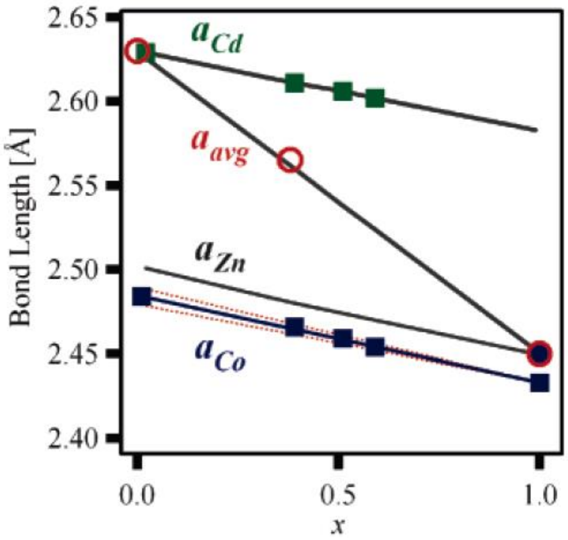

Figure 1.10. Bimodal bondlength distribution in a series of Co^{2+}:$Cd_{1-x}Zn_xSe$ alloys. Blue squares are Co-Se bondlengths determined from the position of the $^4A_1 \rightarrow {}^4T_2(P)$ transition, is shorter than the average bondlength determined from XRD, red circles. Green squares are the Cd-Se bondlength calculated for each alloy with the assumption that Zn and Co have similar bond legths to Se. Figure adapted from Ref. 38.

1.6 The cluster synthesis

A method parallel to the "hot injection", based on the decomposition of Cd^{2+}-Se^{2-} clusters, had been developed for the synthesis of various II-VI semiconductor nanocrystals. Unlike the "hot injection" method that consists of nucleation and growth phases, the cluster synthesis can be described as controlled Ostwald ripening. The phenylthiolate terminated clusters of cadmium and selenium atoms were another possible solution to the hydrophobic Cd^{2+} precursor problem, but were fundamentally different from previous precursors as they were also Se^{2-} and as was subsequently shown S^{2-} precursors.[39] The syntheses consisted of heating these clusters in weakly coordinating solvents, such as hexadecylamine, for various amounts of time ranging from hours to days.[40]

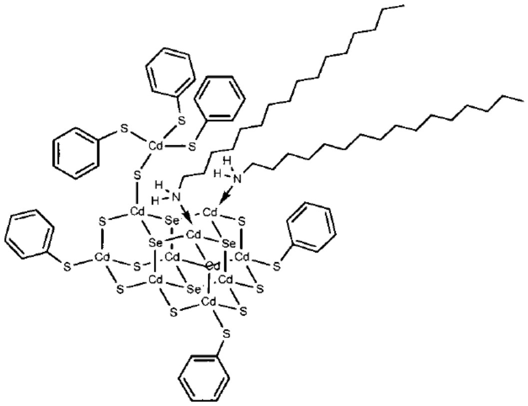

Figure 1.11. Ligation of a cluster by hexadecylamine. Figure adapted from Ref. 40.

Nanocrystal growth likely consisted of a combination of fusion of various clusters as well as decomposition of smaller clusters to give monomeric precursors for deposition onto the growing nanocrystals. Relatively monodisperse ensembles could be prepared by this method, as long as the average diameter remained below 4 nm. The growth rates were slow, the average CdSe nanocrystal ensemble size increase from 3 nm to 4 nm required hours at temperatures below 230°C. Preparation of larger nanocrystals required increased growth temperatures, however this was accompanied by a significant loss of monodispersity.

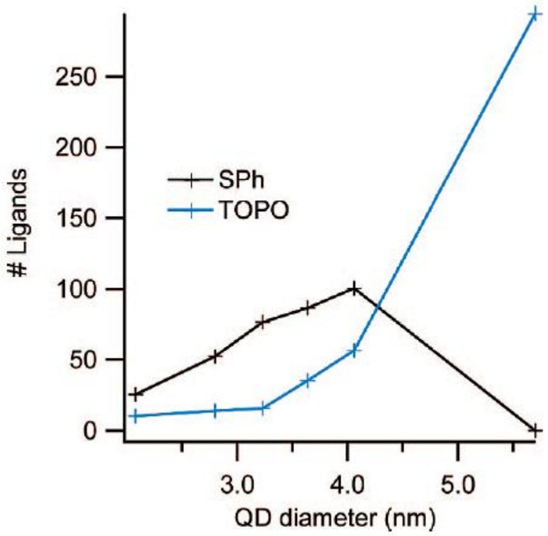

Figure 1.12. Abundance of phenylthiolate vs trioctylphosphineoxide on the surface of the nanocrystal as a function of size. Figure adapted from Ref. 41.

One unique feature of these nanocrystals was the possible termination of the nanocrystal by the phenylthiolates derived from the clusters. It has been shown that the number of phenylthiolates maximizes on the surface of the nanocrystals when the average nanocrystal size in the ensemble is approximately 4 nm.[41] One consequence of this is that deposition of nutrients was not proportional to the surface area of the nanocrystal, with phenylthiolates slowing down the growth of larger particles. This is a possible explanation for the observed ensemble monodispersity under these conditions, in complete analogy to size focusing during diffusion limited growth, where the depletion layer resulted in decreased growth of larger nanocrystals. Size dependent reactivity afforded by phenylthiolates is also similar to facet dependent reactivity mediated by phosphonic acids for the synthesis of seeded rods described earlier. The big negative consequence of phenylthiolates on the surface was that high temperature growth of nanocrystals with diameters above 4 nm was inherently reaction limited and required either decomposition or removal of phenylthiolates from the surface of the nanocrystal.

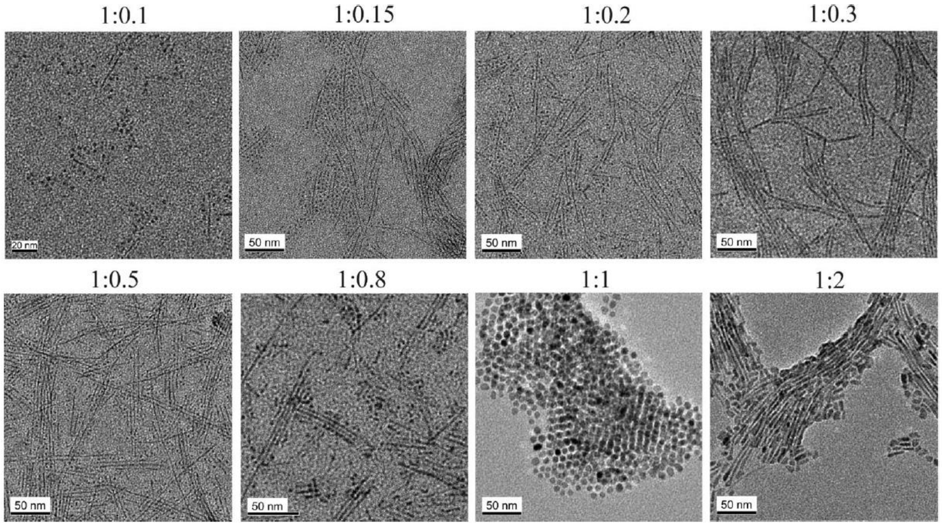

Figure 1.13. TEM of Mn^{2+}:ZnSe grown by the cluster synthesis with variable Zn to Se ratios shown at the top of each panel. Figure adapted from Ref. 42.

The vast morphological variation[42] of nanoparticles produced by the syntheses based on cluster decomposition may also be mediated by the variable concentration of phenylthiolates and phenylselenates, which undoubtedly varies with purity and age of the cluster. These observations make phenylthiolates potentially useful ligands for nanoscale reactivity manipulation divorced from the cluster synthesis, an area that has not yet been explored.

1.6.A. Doping using the cluster synthesis, accidental core/shell

The search for an effective synthesis of nanocrystalline Mn^{2+}:CdSe moved away from the "hot injection method" as the theoretical basis for the large volume of synthetic failures was being developed invoking the inability of Mn^0 to bind the facets of wurtzite nanocrystals.[29] At the same time the unusual properties of these cluster based syntheses gave people hope, that just maybe, all the theory that was being developed to prove the impossibility of doping would not apply to them. The addition of $MnCl_2$ and elemental Se to the standard cluster synthesis resulted in what was described as Mn^{2+}:ZnSe or Mn^{2+}:CdSe, depending on the cation present in the cluster.[43] In order to gain a better understanding of the syntheses it was also extended to Co^{2+}:CdSe, revealing the Co^{2+} $^4A_1 \rightarrow {}^4T_2(P)$ ligand field transition in the resulting material.[44] The absorption feature of this transition had a different line shape and energy position relative to the one observed in Co^{2+}:CdSe nanocrystals synthesized by the "hot injection" method, instead it closely matched the one observed in bulk Co^{2+}:CdS. This observation made a strong case for the core/shell CdSe/Co^{2+}:CdS structure of these nanocrystals, where Co^{2+} ions were present in the particles, but were bonded only to S^{2-}. The inversion of the excitonic MCD signal confirmed the presence of Co^{2+} inside the nanocrystals, however its magnitude was not consistent with the analytical Co^{2+} concentration. The excitonic wavefunction was attenuated inside the Co^{2+}:CdS shell of these nanocrystals, because of the relative band offsets between CdSe and CdS, decreasing the strength of the effective exchange interaction between Co^{2+} and the exciton.

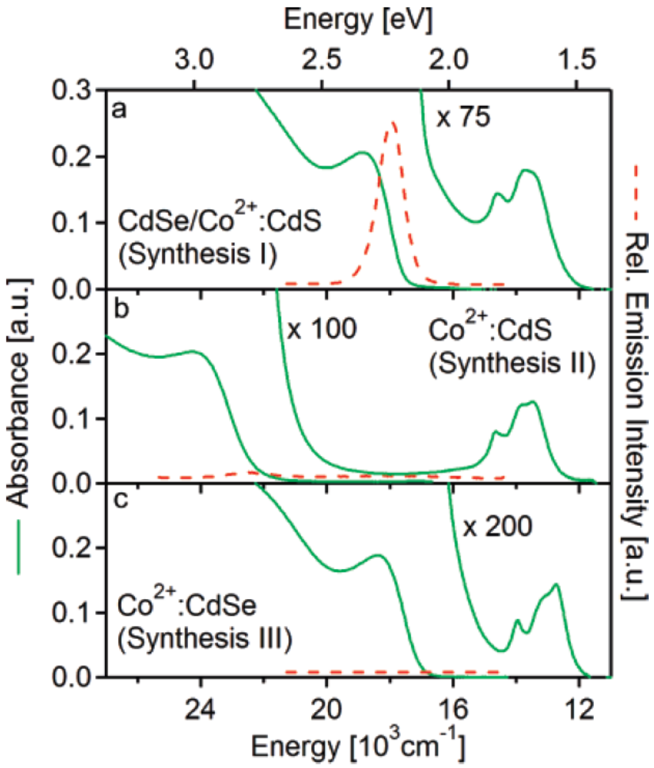

Figure 1.14. (a) CdSe/Co^{2+}:CdS core/shell nanocrystals made using cluster terminated by phenylthiols. (b) Co^{2+}:CdS showing the ${}^4A_1 \rightarrow {}^4T_2(P)$ transition in a similar position as the one above. (c) Co^{2+}:CdSe made using a cluster with phenylthiolates replaces by phenylselenols. Figure adapted from Ref. 44.

This analysis set the precedent for deriving information about the position of the excitonic wavefunction through its interaction with magnetic dopants, probed by MCD spectroscopy. The distribution of anions in the core/shell arrangement, could be explained by the much lower propensity of S^{2-} from the phenylthiolate to integrate into the nanocrystal relative to Se^{2-} in the cluster. The segregation of Co^{2+} into the CdS shell was strong evidence that under these slow growth conditions, the equilibria directing nanocrystal growth are governed by the hard soft acid base (HSAB) properties of the nutrients. The segregation was either the result of Co^{2+} inability to compete with Cd^{2+} for surface Se^{2-} and only became competitive once surface

S^{2-} became available, or by the ability of Co^{2+} and Cd^{2+} cations to redistribute inside the nanocrystal to maximize the overall bond strength. Strong evidence for the latter scenario was provided by the successful syntheses of Co^{2+}:CdSe, Mn^{2+}:ZnSe and Mn^{2+}:CdSe, achieved by the removal of the S^{2-} source, replacing phenylthiolates with phenylselenides.[44,45]

1.6.B. Adaptation, success and limitations

The successful adaptation of the cluster synthesis for nanocrystal doping lead to the observation of spontaneous light-induced magnetization of the Mn^{2+} sublattice and exciton storage by the Mn^{2+} $^4T_1$ state in Mn^{2+}:CdSe.[46] Excitons in Mn^{2+}:CdSe nanocrystals with the $^4T_1$ state of Mn^{2+} higher in energy than the excitonic states, exhibited dynamic stabilization, observed as a time dependent red shift of the excitonic luminescence decay.[47] The magnitude of this red shift had a temperature dependence consistent with Mn^{2+} magnetization, which was both driven by the exchange interaction with the exciton and stabilized the exciton through the exchange interaction. Excitons in Mn^{2+}:CdSe nanocrystals with the $^4T_1$ state of Mn^{2+} lower in energy than the excitonic states, transferred their energy to Mn^{2+} at least 100 times faster than the rate of excitonic emission in undoped CdSe nanocrystals. Thermally activated energy transfer from the long lived $^4T_1$ state of Mn^{2+}, back to the excitonic states with subsequent excitonic emission was the dominant radiative decay pathway, except at cryogenic temperatures where Mn^{2+} $^4T_1 \rightarrow {}^6A_1$ emission could be observed.[48]

Cluster synthesis of Mn^{2+}:ZnSe had a significant advantage over any other Mn^{2+}:ZnSe synthesis available: these were all plagued by low Mn^{2+} concentrations in the resulting nanocrystals. This especially became an issue during core/shell preparations with Mn^{2+}:ZnSe used as the core.[49] Deposition of a shell, required the core nanocrystals to be placed under conditions that allowed cation exchange with solution. Mn^{2+} loss could be mitigated by a judicious choice of ligands, temperatures and anion concentration, however it could not be eliminated completely and at low dopant concentration in the core the production of an undoped subset of nanocrystals was always a possibility. Flexibility afforded by Mn^{2+}:ZnSe cores with many Mn^{2+} dopants, allowed a variety of new Mn^{2+} doped nanocrystals to be synthesized. Energy of the excitonic states in Mn^{2+}:ZnSe/CdSe core/shell nanocrystals could be varied continuously in the 2-3 eV range by varying the thickness of the CdSe shell. This made it possible to not just reach the exciton storage regime, that was first observed in Mn^{2+}:CdSe nanocrystals, but to tune the sensitivity of exciton storage to a specific temperature range anywhere between 77K and 400K.[50] The multishell Mn^{2+}:ZnSe/ZnS/CdS/ZnS nanocrystals combined both stability, afforded by the outer ZnS shell, and attenuation of the alloying induced excitonic drift using the internal ZnS shell as a buffer between ZnSe and CdS layers.[51]

The unique growth conditions of the cluster synthesis, characterized by a very slow growth stage, proved to be effective at allowing dopants to incorporate into the nanocrystals. The slow growth was also accompanied by slow doping and since these stages could not be decoupled, the synthesis of small nanocrystals presented a major challenge. Mn^{2+}:CdSe nanocrystals small enough in diameter to exhibit exciton storage had few dopants per nanocrystals, resulting in a significant undoped subset. The synthesis of large nanocrystals with a narrow size distribution was also a challenge because growth above 4 nm could only be achieved through uncontrolled Ostwald ripening. Samples of Mn^{2+}:ZnSe nanocrystals were always plagued by varying degrees of ensemble inhomogeneity, both in size and morphology. Strong dependence of nanocrystal shape on the Zn:Se ratio in the synthesis was clearly demonstrated, however none of the conditions presented actually produced samples of uniform morphology.

Mn^{2+}:$Zn_{1-x}Cd_xSe$ alloys synthesized using the cluster method allowed a faster preparation of nanocrystals in the exciton storage regime. These alloy nanocrystals were of a variety of morphologies and the authors were able to collect TEM images showing clear evidence of nanocrystal fusion through oriented attachment.[52]

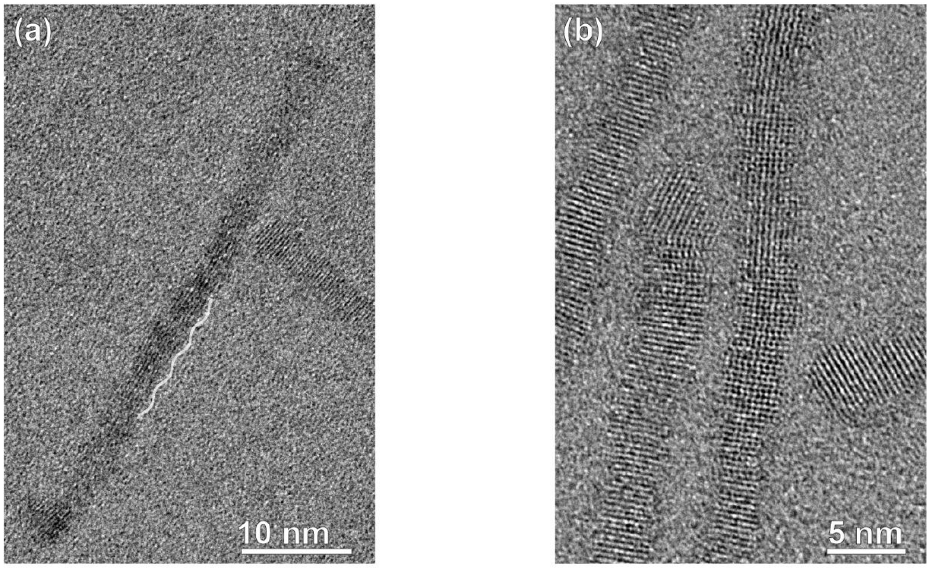

Figure 1.15. Mn^{2+}:$Zn_{1-x}Cd_xSe$ alloys made using the cluster synthesis showing nanorods made from fused nanocrystals. Figure adapted from Ref. 52.

Uniform spherical Mn^{2+}:ZnSe were eventually synthesized through meticulous control of synthetic parameters by Bradshaw, L. R. et. al. Future syntheses of uniform Mn^{2+}:ZnSe will require precise synthetic control in order to reproduce this work.[53] Non-uniformity of nanocrystals to be used as precursors for further syntheses makes any promising result difficult to reproduce and to investigate further. These observations made it clear that the II-VI nanocrystal doping problem had not been completely solved.

1.7 Escaping the delusion of established scientific facts

Reports of core/shell morphologies, existence of undoped cores and extremely low rates of diffusion observed in bulk made it a foregone conclusion that dopant incorporation must occur simultaneously with nanocrystal growth. Groups working on nanocrystal doping failed to recognize the high mobility of cations between the nanocrystals and solution during nanocrystal growth. Paradoxically observations of rapid alloying and significant cation exchange between the nanocrystal and solution were not seen as useful properties that could be exploited for doping. Instead, theoreticians armed with powerful calculation techniques, split into two camps to argue about why doping nanocrystals is impossible. Erwin, S.C. et. al., published their thoughts in a Nature article[29] that has since been cited 659 times, proposing that wurtzite CdSe nanocrystals cannot be doped with Mn^{2+} because adsorption of Mn^0 to the surface of a wurtzite nanocrystal was calculated to be much less favorable than adsorption to the surface of a zinc blende nanocrystal. The fact that most CdSe nanocrystal ensembles contain a significant fraction of both zinc blende and wurtzite crystals, XRD diffraction pattern published in the same paper not withstanding, did not make their argument less convincing. Dalpian G.M. et. al., published their calculations in Physical Review Letters, eventually receiving 226 citations, making their case around the size dependent ability of a nanocrystal to cope with the energetic cost associated with the replacement of a Cd^{2+} atom with a Mn^{2+} atom.[54]

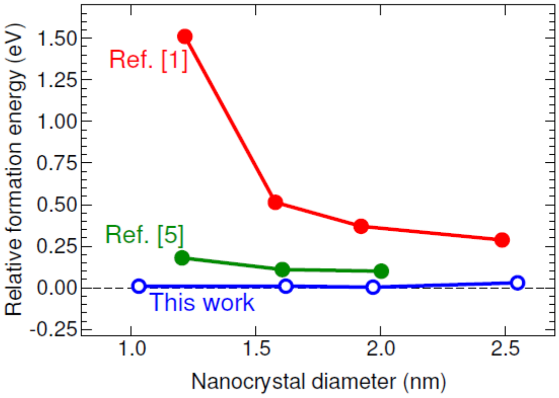

Figure 1.16. Relative formation energy for Mn^{2+} vs Cd^{2+} inside a CdSe nanocrystal as a function of size. Original calculation by Dalpian G.M. et. al. in red. Counter calculation by Erwin, S.C. et. al. in blue. Adjusted calculation by Dalpian G.M. et. al. in green. Figure adapted from Ref. 55.

Erwin, S.C. et.al. showed off the power of DFT to get results in their retort published in a comment to the Dalpian G.M. et. al. PRL article.[55] Their calculations showed that the energetic costs of defects in nanocrystals are essentially independent of size. Reiterating the statements from their Nature paper, Erwin, S.C. et.al. made a firm assertion that diffusion barriers at typical synthetic temperatures cannot be overcome and thermodynamic equilibrium cannot be reached, therefore a nanocrystal that has trapped an impurity has no mechanism by which to purify itself unless it dissolves and reforms. The response by Dalpian G.M. et. al. was to perform the calculation again, admit that the original calculation overestimated formation energies by an order of magnitude, but to hold on to the fact that the size dependent trend still existed and was consistent with calculations performed for many other systems.[56] An important approximation made by Dalpian G.M. et. al. in their original publication was to remove both Cd^{2+} and Mn^{2+} chemical potentials from their calculation of what became essentially relative formation energy of a defect in a nanocrystal removed from reality. Ironically, these chemical potentials are precisely what has been driving solution mediated cation exchange described earlier and synthetic control over these chemical potentials had been the principle behind doping by cation exchange.[57]

Subverted by DFT, big name journals, crowds of good students and a battle between those who got it completely wrong and those who left out the solution to the problem, the theoretical path to Mn^{2+}:CdSe nanocrystals was obscured. The followers of Erwin, S.C. et.al. saw the problem as a question of tricking the dopants to adhere to the surface and then to quickly trap them before they could escape back into solution, once the dopants were trapped the problem was solved. Trapping of dopants by using isocrystalline core/shells had been introduced earlier by Radovanovic P.V. et.al. in a successful CdS/Co^{2+}:CdS synthesis.[36] The desire to trap dopants, instead of just letting them in, had echoes throughout the doping literature. This kinetic trapping approach began to lose its appeal once it became clear that core/shell nanocrystals readily alloy and cations freely move between solution and nanocrystal. The followers of Dalpian G.M. et. al. imagined that to every host semiconductor/dopant combination corresponded a critical nanocrystal diameter below which doping was impossible. This view was weakened once Archer et. al. adapted the cluster synthesis to synthesize, S^{2-} free, Mn^{2+}:CdSe nanocrystals, however. According to G.F Strouse, the cluster synthesis proceded by the fusion of progressively larger clusters resulting in a large number of defects at the interfaces, making Mn^{2+} an insignificant destabilization to the crystal.[40]

Optimized “hot injection” synthesis of Co^{2+}:CdSe nanocrystals allowed high doping concentrations with Cd^{2+} to Co^{2+} ratios as high as 2:1. The Co^{2+} $^4A_1 \rightarrow {}^4T_1(P)$ ligand field transition served as a convenient probe of Co^{2+} concentration and could be monitored simultaneously with the excitonic transition by UV/Vis absorption as a function of growth time. The results were surprising in that the excitonic transition did not red shift with increasing growth time, as expected from decreased quantum confinement with increasing nanocrystal size. At the same time the Co^{2+} ligand field transition increased in intensity signifying Co^{2+} incorporation into the nanocrystals. This apparent independence of nanocrystal growth and doping was not understood and quietly dissmissed. Extension of this optimized synthesis to Mn^{2+} was successful, with Mn^{2+} concentrations of up to 2%. The observation that at the time was misunderstood, but later turned out to be critical was a strong dependence of Mn^{2+}:CdSe ensemble size distribution on the amount of Mn^{2+} precursors used for a given synthesis. If Mn^{2+} (Co^{2+} had a similar effect) was completely removed from the reaction, CdSe growth was rapid and random, producing nanocrystals of all sizes. At the time it was believed that Mn^{2+} bound to the surface and attenuated growth. This explanation would find support from both Erwin S.C. et. al. and Dalpian G.M. et. al., the first would likely argue that Mn^{2+} only bound to some key facets of the nanoparticle surface preventing isotropic growth, while the latter would claim that any Mn^{2+} that was internalized would create such instability that Mn^{2+}:CdSe nanocrystals would contribute strongly to the overall dissolution rate, thus attenuating growth. Increasing the Mn^{2+} concentration in the growth solution eventually disturbed the nucleation stage, where no nuclation was observed or it proceded so slowly that no ensemble homogeneity could be achieved. This view of nanocrystal behaviour during nucleation and doping had been previously put forth in the ZnO nanocrystal literature by D.A. Schwartz and J.D. Bryan.[5] In these syntheses the carboxylic acid was always strictly minimized with respect to the amount of cations used, which made reproduction difficult, with slight changes in absolute ligand concentration translating into significant effects on solubility of both nanocrystals and cations in solution. Evidence for decoupled growth and doping that was observed for Co^{2+}:CdSe, once again appeared as 5 minute and 30 minute growth time produce CdSe of the same size, however longer growth times resulted in higher Mn^{2+} concentrations. Unlike Co^{2+} with its convenient ligand field absorbance, Mn^{2+} concentrations had to be inferred from elemental analysis, which could not differentiate between, surface, solution and internal Mn^{2+} and were viewed with skepticism especially when they supported theories that did not have the support of DFT.

Resolution of this problem required a reproducible Mn^{2+}:CdSe synthesis followed by a lot of meticulous work monitoring Mn^{2+}:CdSe during growth comparing nanocrystal size and concentration of only internal Mn^{2+}. Barrows C.J. made key observations about ligand speciation and evolution in the reaction solution, allowing him to synthesize Mn^{2+}:CdSe with a high degree of reproduciblity and control. These details must be published in the future. He then proceded to prove that growth and doping took place separately using a combination of EPR, elemental analysis and room temperature MCD, which made it unnecessary to attempt simultaneous optimization of reaction conditions for nucleation, growth and doping. Exploration of doping separately from growth yielded unexpeected results that have far reaching consequences in our understanding of what has been happening during nanocrystal growth in all the syntheses performed over the last 20+ years. These results and the first major breakthroughs are described in Chapter 5.[58]

1.8 What has changed and what is to be done

A crystal placed in a solution will dissolve until the concentration of its substituent nutrients reaches a high enough level that deposition exactly balances dissolution. The presense of this equilibrium leads to Ostwald ripening, which is proportional to the concentration of nutrients in solution. The degree to which CdSe nanocrystals dissolve increases with temperature and concentration of ligands that can accommodate Cd^{2+} and Se^{2-} in solution. Complete removal of such ligands would completely suppress Ostwald ripening, however without these ligands the nanocrystals would lose their solubility and leave the solution. At low temperatures it is possible to choose the proper ligand concentration to suspend the nanocrystals and to have no dissolution. As the temperature increases however, the range of possible ligand concentrations to achieve this balance approaches zero. The major synthetic breakthrough that allowed us to demonstrate doping by diffusion, was identification of high tempterature conditions under which nanocrystal dissolution and consequently interparticle cation transfer was suppressed. Ligands saturated with Mn^{2+} cations were found to be capable of maintaining nanocrystal solubility, perhaps binding to the nanocrystals together with a Mn^{2+} cation. However, Cd^{2+} cations were unable to compete with Mn^{2+} for these ligands and consequently had no way to move between different nanocrystals.

The possible uses of this Mn^{2+} saturated ligand system do not end with Mn^{2+} doping applications. Core/shell syntheses described in section 1.3.A., are performed under conditions where the ligand concentration increases during the course of the synthesis as more ligands becomes free with successful transfer of their cations onto the growing nanocrystals. Increased ligand concentrations necessitate the use of lower temperatures to suppress ripening. It should be possible to use the Mn^{2+} saturated ligand set as a buffer to occupy the ligands that build up during core/shell syntheses. This should in turn allow for longer growth times and higher temperatures, while preserving the monodispersity of the nanocrystals. Since this use of Mn^{2+} is not dependent on the ability of Mn^{2+} to dope, it should be applicable to all syntheses that use carboxylic acids and amines to suspend growing nanocrystals. For example the various syntheses of III-V semiconductor nanocrystals.

By synthesizing Mn^{2} :CdSe nanocrystals with a high Mn^{2+} concentration we have settled the long standing debate about why it is impossible. It is no longer necessary to trap dopants, because as it has been shown by numerous doping attempts, ZnSe and CdSe are not a prison for Mn^{2+}. The fact that it took so long to even believe that this is possible shows that we did not understand a fundamental difference between bulk and nanoscale materials. Bimodal bondlength distributions, like the one described in section 1.5.C. for Co^{2+}:$Cd_{1-x}Zn_xSe$ alloys, have also been observed in bulk and are a statement about the ability of a crystal to distort in order to maximize the stabilization energy from its cavalent bonds. At the nanoscale this ability to distort translates into the ability of the nanocrystal to assume conformations that allow cations to move between lattice sites. Furthermore the proximity of nanocrystal surface to the interior of the crystal makes the set of infinite random walks of a cation in bulk, a much smaller set of finite ones in the nanocrystal, with the possibility of a big enthalpic payoff at the end.

The choice of ligands will be critical in future CdSe doping attempts. It is unlikely that hard Lewis acids will be compatible with the current Mn^{2+}/stearic acid/hexadecylamine ligand set used to suppress Ostwald ripening. Under conditions where elemental equilibrium can be reached, Mn^{2+} will outcompete harder Lewis acids for a place inside CdSe. Finding a new ligand set around a cation that is harder than Mn^{2+} would immediately broaden the range of possible dopants. Analogously, CdSe nanocrystals doped with a hard Lewis acid such as Mg^{2+}, would be ideal candidates for doping by cation exchange with any cation that is softer. Inability of CdSe nanocrystal to trap dopants poses significant synthetic problems. Elements that are able to bond with Se^{2-}, but do not prefer a tetrahedral bonding arrangement, such as Cu^{2+} and Ni^{2+}, are likely to migrate to the surface and nucleate new phases. Dopants that are in unstable oxidation states or have high reactivity toward a compound in solution are likely to be lost during high temperature treatments. One exampleof this would be Cr^{2+}, that rapidly makes Cr-Cr dimers in the presense of carboxy groups and will rapidly oxidize to Cr^{3+} in the presence of oxygen. Overall this suggests that doping strategies centered around kinetic trapping are unlikely to be successful in the future.

The ability to move cations internally and to reach elemental equilibrium with solution makes these nanocrystals appear as anionic cages, playing the role of ligands for the cations, similarly to the carboxylic acids in solution. Adopting this view means that a CdSe nanocrystal is a ligand with a dissociation constant tunable by its size, given that large nanocrystals must distort more bonds to achieve a conformation that allows the passage of cations between lattice sites. An experiment where Co^{2+}:CdSe is mixed with undoped CdS at temperatures that allow cations to move, would illustrate this view of CdSe as a ligand with the production of Co^{2+}:CdS.

The concept of doping under this conceptualization of CdSe nanocrystals translates to the formation of a Se^{2-} cage that is too big for all the Cd^{2+} cation that are available. The two currently available methods for forming such a Se^{2-} cage are the removal of Cd^{2+}, known as cation exchange, or deposition of shells consisting of Se^{2-} and a counter ion, that is either the target dopant or is later replaced by a dopant of choice by cation exchange. The latter had been employed in our diffusion doping strategy and has the potential for further generalization, however dopants that are hard Lewis acids and cannot be deposited as counter cations together with Se^{2-} onto CdSe are not compatible. The development of a third way is necessary and it is not at all obvious how this is possible, however all impossibilities are only inside our own minds.

1.9 References

(1) Murray, C. B.; Norris, D. J.; Bawendi, M. G. *J. Am. Chem. Soc.* **1993**, *115*, 8706.

(2) Brus, L. E. *Appl. Phys. A* **1991**,53,465.

(3) Bawendi, M. **G.;** Kortan, A. R.; Steigerwald, M. L.; Brus, L. E**.** *J.Chem. Phys.* **1989**, 91, 7282.

(4) Brus.L.E. *J. Phys. Chem.* **1986,** 90, 2555.

(5) Bryan, J. D.; Gamelin, D.R. *Prog. Inorg. Chem.* **2005**, 54, 47-126.

(6) Sugimoto, T. *Adv. Colloid Interfac. Sci.* **1987**, *28*, 65.

(7) Talapin, V.D.; Rogach, L. A.; Haase, M.; Weller, H**.** *J. Phys. Chem. B,* **2001**,105, 49, 12278-12285.

(8) Garcia-Rodriguez, R.; Liu, H. *J. Am. Chem. Soc.* **2012**, 134, 1400−1403.

(9) Ostwald, W. *Z. Phys. Chem*. **1901**, *37*, 385.

(10) Rosenthal, J. S.; McBride, J.; Pennycook, J. S.; Feldman, C. L. *Surface Science Reports.* **2007,** 62, 111–157.

(11) Bawendi, M. G.; Kortan, A. R.; Steigerwald, M. L.; Brus, L. E. *J. Chem. Phys.* **1989**, 91, 7282.

(12) Peng, Z.A.; Peng, X. *J. Am. Chem. Soc.* **2001**, 123, 183.

(13) Carbone, L. et al. *Nano Letters*. **2007,** 7, 2942-2950.

(14) Talapin, D. V.; Rogach, A. L.; Kornowski, A.; Haase, M.; Weller, H. *Nano Letters,* **2001,** 1, 207.

(15) Embden, J.; Jasieniak, J.; Gómez D. E.;Mulvaney, P.; Michael Giersig, M. Aust. J. Chem. 2007, 60, 457–471.

(16) Balet, L. P.; Ivanov, S. A.; Piryatinski, A.; Achermann, M.; Klimov,V. I. *Nano Letters.***2004,** 4, 1485–1488.
(17) Kim, S.; Fisher, B.; Eisler, H.J.; Bawendi, M. *J. Am. Chem. Soc.***2003,** 125, 11466.
(18) Xie, R.; Zhong, X.; Basche, T. *Adv. Mater.* **2005**, 17, 2741.
(19) Ivanov, S. A.; Piryatinski, A.; Nanda, J.; Tretiak, S.; Zavadil, K. R.; Wallace, W. O.; Werder, D.; Klimov, V. I. *J. Am. Chem. Soc.* **2007**, 129, 11708.
(20) Talapin D.V., et al., *Nano Letters.* **2003**, 3, 1677.
(21) Talapin, D. V.; Nelson, J. H.; Shevchenko, E. V.; Aloni, S.; Sadtler, B.; Alivisatos, A. P. *Nano Letters.* **2007**, 7, 2951–2959.
(22) Fiore A. et. al., *J. Am. Chem. Soc.* **2009**, *131*, 2274–2282.
(23) Zhong, H.; Scholes G. D. *J. Am. Chem. Soc.* **2009.** 131, 26, 9171.
(24) Darwent B.B., National Standard Reference Data Series, NationalBureau of Standards, no. 31, Washington, 1970.
(25) Zhong, X.; Han, M.; Dong, Z.; White, T. J.; Knoll, W. *J. Am. Chem. Soc.* **2003**, 125, 8589.
(26) Groeneveld, E. et. al., *ACS NANO*, **2013**, 7, 7913-7930.
(27) Zhong, X.; Feng, Y.; Zhang, Y.; Gu, Z.; Zou, L. *Nanotechnology*, **2007**, 18, 385606.
(28) Beaulac, R.; Ochsenbein, S. T.; Gamelin, D. R., Colloidal Transition-Metal-Doped Quantum Dots. In *Semiconductor Quantum Dots*, 2nd ed.; Klimov, V. I., Ed. CRC Press: **2010**.
(29) Erwin, S.C., Zu, L.J., Haftel, M.I., Efros, A.L., Kennedy, T.A., & Norris, D.J., Doping semiconductor nanocrystals. *Nature* **2005** 436, 91-94.
(30) Furdyna, J. K.; Kossut, J. *Semiconductors and Semimetals*; Academic: New York, **1988**; Vol. 25.
(31) Bhargava, R. N., Gallagher, D., Hong, X. & Nurmikko, A. Phys. Rev. Lett. 72, 416–-419 (**1994**).
(32) Hoffman, D.M.; Meyer, B.K.; Ekimov, A.I.; Merkulov, I.A.; Efros, A.L.; Rosen, M.; Counio, G.; Gacoin, T.; Boilot, J.-P. Sol. State Comm. **2000**, 114, 547.
(33) Suyver, J. F., Wuister, S. F., Kelly, J. J. & Meijerink, A. Phys. Chem. Chem. Phys. 2, 5445–-5448 (**2000**).
(34) Mikulec, F.V.; Kuno, M.; Bennati, M.; Hall, D.A.; Griffin, R.G.; Bawendi, M.G. J. Am.Chem. Soc. **2000**, 122, 2532.
(35) Radovanovic, P. V.; Gamelin, D. R *J. Am. Chem. Soc.*, **2001**, *123*, 12207-12214.
(36) Radovanovic, P. V.; Gamelin, D. R. Proc. SPIE-Int. Soc. Opt. Eng., **2002**, 4809, 51-61.
(37) Norberg, N. S.; Parks, G. L.; Salley, G. M.; Gamelin, D. R. *J. Am. Chem. Soc.*, **2006**, *128*, 13195-13203.
(38) Santangelo, S. A.; Hinds, E. A.; Vlaskin, V. A.; Archer, P. I.; Gamelin, D. R. J. Am. Chem. Soc., **2007**, 129, 3973-3978.
(39) Dance, I. G.; Choy, A.; Scudder, M. L. J. Am. Chem. Soc. **1984**, 106, 6285-6295.
(40) Cumberland, S.L.; Hanif, K.M.; Javier, A.; Khitrov, G.A.; Strouse, G.F.; Woessner, S.M.; Yun, C.S. *Chem. Mater.,* 14, 1576-1584 (**2002**)
(41) Lovingood, D.D., et. al. *J. Am. Chem. Soc.* **2008,** 130, 17004-11.
(42) Patrick T. K. Chin, Jan W. Stouwdam, and Rene A. J. Janssen. *Nano Lett.* **2009,** 9, 745.
(43) Magana, D.; Perera, S. C.; Harter, A. G.; Dalal, N. S.; Strouse, G. F. J. Am. Chem. Soc. **2006**, 128, 2931-2939.
(44) Archer, P.I.; Santangelo, S.A.; Gamelin, D.R. *J. Am. Chem. Soc.* **2007**, *129,* 9808.

(45) Archer, P.I.; Santangelo, S.A.; Gamelin, D.R. *Nano Lett.* **2007**, *7*, 1037.

(46) Beaulac, R.; Archer, P.I.; Ochsenbein, S.T.; Gamelin, D.R. *Adv. Funct. Mater.* **2008,** 18, 3873.

(47) Beaulac, R.; Schneider, L.; Archer, P. I.; Bacher, G.; Gamelin, D. R. *Science*, **2009**, *325*, 973-976.

(48) Beaulac, R.; Archer, P. I.; van Rijssel, J.; Meijerink, A.; Gamelin, D. R. *Nano Letters*, **2008**, *8*, 2949-2953.

(49) Bussian, D. A.; Crooker, S. A.; Yin, M.; Brynda, M.; Efros, Al. L.; Klimov, V. I. *Nat. Mater.* **2009**, 8, 35–40.

(50) Vlaskin, V. A.; Janssen, N.; van Rijssel, J.; Beaulac, R.; Gamelin,D. R. *Nano Lett.* **2010**, 10, 3670.

(51) McLaurin, E. J.; Vlaskin, V. A.; Gamelin, D. R. J. Am. Chem. Soc. **2011**, 133, 14978.

(52) McLaurin, E. J.; Fataftah, M. S.; Gamelin, D. R. Chem. Commun., **2013**, 49, 39.

(53) Bradshaw, L. R.; Hauser, A.; McLaurin, E. J.; Gamelin, D. R. J. Phys. Chem. C., 2012, 116, 9300.

(54) Gustavo M. Dalpian and James R. Chelikowsky Phys. Rev. Lett. **2006**, 96, 226802.

(55) M.-H. Du, S.C. Erwin, Al.L. Efros, D.J. Norris. Phys. Rev. Lett. **2008**, 100, 179702 .

(56) Gustavo M. Dalpian and James R. Chelikowsky Phys. Rev. Lett. **2008**, 100, 179703.

(57) Dong Hee Son, Steven M. Hughes, Yadong Yin, A. Paul Alivisatos. Science **2004**, 306 1009-1012.

(58) Vlaskin, V. A.; Barrows, C. J.; Erickson, C. S.; Gamelin, D. R. *J. Am. Chem. Soc.*, **2013**, *135*, 14380-14389.

Chapter 2: Dopant-Carrier Magnetic Exchange Coupling in Colloidal Inverted Core/Shell Semiconductor Nanocrystals

2.1 Introduction

The physical properties of colloidal semiconductor nanocrystals can be modified in fascinating ways by growth of conformal epitaxial shell layers.[1,2] Shell growth has been used to passivate surface defects,[3-5] isolate electronic wavefunctions from surface dipoles,[6] reduce luminescence intermittency ("blinking"),[7,8] achieve efficient optical amplification,[9] or even separate charges across the core/shell interface.[10-14] In recent years, many of the shell growth techniques developed to modify colloidal semiconductor nanocrystals have begun to be applied to alter the physical properties of impurity doped semiconductor nanocrystals. Colloidal doped core/shell nanocrystals have now demonstrated interesting properties attractive for spintronics, spin-photonics, bioimaging, energy-efficient lighting, or solar energy conversion technologies. Recent studies of doped core/shell heterostructures have described enhancement of sensitized dopant photoluminescence quantum yields by insulating shell growth,[15-20] phase-templated modification of surface adsorption enthalpies,[21] dual-mode bioimaging,[22] large radial pressure effects,[17,23] and modified dopant-carrier magnetic exchange coupling across core/shell heterointerfaces.[24] Doped isocrystalline core/shell nanocrystals, in which the core and shell materials are the same, have also been explored as synthetic model systems for understanding or improving doping chemistries[25-27] and to improve phosphor performance.[27-29]

Herein, we describe optical MCD results obtained for a series of Co^{2+}- and Mn^{2+}-doped ZnSe core, inverted ZnSe/CdSe core/shell, and ZnSe/ZnSe isocrystalline core/shell colloidal nanocrystals. Manifestations of kinetic *s-d* exchange were not observed in any of these samples.

Electronic structure considerations have led to the conclusion that $Zn_{1-x}TM_xSe$/CdSe inverted core/shell nanocrystals are not suitable for observation of this phenomenon: CdSe shell growth is shown to quench the strong conduction-band confinement proposed to enable kinetic *s-d* exchange, and wavefunction calculations suggest that this heterostructure is unable to reduce h_{VB}^{+} -core overlap sufficiently to isolate the *s-d* exchange interaction. Instead, the magneto-optical changes observed upon shell growth in $Zn_{1-x}Mn_xSe$/CdSe nanocrystals are shown to be largely independent of the electron's wavefunction or even the distinction between homo- and heterointerfaces, arising instead from gradual reduction of dopant-hole overlap due to expansion of the hole wavefunction into the undoped shell volume.

2.2 Apparent observation of large quantum confinement induced s-d exchange

Recently, $Zn_{1-x}Mn_xSe$/CdSe inverted core/shell nanocrystals were reported to display magnetic exchange coupling effects that are fundamentally different from those of their bulk counterpart materials, made possible by the unique combination of strong quantum confinement and wavefunction engineering in these heterostructures.[30] Compared to the large kinetic "*p-d*" exchange interactions between valence band holes (h_{VB}^{+}) and transition-metal dopants that normally dominate the magneto-optics of II-VI and III-V diluted magnetic semiconductors (DMSs),[31] "*s-d*" magnetic exchange between dopant spins and conduction band electrons (e_{CB}^{-}) is generally weak because hybridization between the conduction band wavefunction at $k = 0$ and the transition-metal *d* orbitals is formally forbidden by symmetry, leaving potential exchange as the main coupling mechanism.[31,32] Theory has suggested that quantum confinement can relax this symmetry restriction by introducing $k \neq 0$ components into the conduction-band-edge wavefunction, which may in principle transform the fundamental nature of the electron-dopant "*s-d*" coupling mechanism from potential to kinetic exchange.[33] Such confinement-induced kinetic *s-d* exchange coupling was proposed to become large in DMS quantum wells, and to even rival the dominant kinetic *p-d* exchange magnitude in DMS quantum dots (QDs).[33] Although postulated a decade ago,[33] compelling experimental evidence for kinetic *s-d* exchange had remained elusive[33,34] until recently, when such coupling was concluded to dominate the excitonic Zeeman splittings of colloidal $Zn_{1-x}Mn_xSe$/CdSe inverted core/shell nanocrystals, as detected by optical magnetic circular dichroism (MCD) spectroscopy.[30] In these nanocrystals, *p-d* exchange coupling was minimized by rapid extraction of the holes from the doped ZnSe cores into the CdSe shells, allowing the weaker *s-d* interaction to be observed by MCD at the absorption band edge. From the MCD sign inversion observed upon shell growth, dominant kinetic *s-d* exchange was concluded. The implications of this conclusion extend well beyond this particular inverted core/shell motif, because if true, then *s-d* exchange interactions in both colloidal and self-assembled doped nanocrystals would frequently be opposite in sign from their assumed values, necessitating extensive reinterpretation of literature data. The unique capacity to engineer carrier wavefunctions in inverted core/shell nanocrystals in order to isolate and examine the previously elusive kinetic *s-d* exchange phenomenon motivated us to explore this motif in greater detail using a broader variety of core and core/shell samples and different dopant ions than investigated previously.

2.3 Excitonic Zeeman splittings

The defining feature of a diluted magnetic semiconductor is the existence of "giant" band-edge Zeeman splittings due to exchange coupling between charge carriers the magnetic dopants within the lattice.[31] These Zeeman splittings can be probed in excitonic states using MCD spectroscopy, where the intensity and sign of the MCD dispersion at the absorption edge reflect the magnitude and sign of the excitonic Zeeman splitting (ΔE_{Zeeman}), respectively.[24,36,37,41-45] Microscopically, ΔE_{Zeeman} derives from a combination of intrinsic and exchange effects as described by the mean-field expression of eq 1,[44-46] where g_{int} is the intrinsic excitonic g factor, μ_B is the Bohr magneton, H is the applied field, x is the dopant cation mole fraction, $<S_z>$ is the temperature- and field-dependant spin expectation value of the dopant ensemble within the QDs, and $N_0\alpha$ and $N_0\beta$ describe *s-d* and *p-d* exchange energies, respectively. The coefficients c_e and c_h describe the projections of the e^-_{CB} and h^+_{VB} probability densities onto the dopant spatial coordinates, respectively.

$$\Delta E_{\text{Zeeman}} = g_{\text{int}}\mu_B H + xN_0\left(c_e\alpha - c_h\beta\right)\langle S_z\rangle \qquad (1)$$

The intrinsic contribution to ΔE_{Zeeman} is small and opposite in sign compared to that arising from dopant-carrier exchange interactions when dopants are effectively incorporated within the internal volumes of the nanocrystals,[24,44,46] and it is therefore often neglected. The giant band-edge Zeeman splittings that arise from these dopant-carrier exchange interactions underlie all major potential spintronics or spin-photonics applications of this class of materials.

Low-temperature electronic absorption and MCD spectra of representative $Zn_{1-x}Mn_xSe$ nanocrystals are shown in Fig. 2.2A(dashed). This and related core samples all show derivative-shaped MCD dispersion at the band edge. The positive sign of the leading edge of this MCD dispersion contrasts with the negative sign typical of undoped semiconductor nanocrystals and confirms that the excitonic Zeeman splittings are dominated by *sp-d* exchange coupling.[44] This coupling is also readily seen from the magnetic field dependence of the excitonic MCD intensity, which displays $S = 5/2$ saturation magnetization that reflects the magnetization of the Mn^{2+} $^6A_1$ ground state (Fig. 2A, inset).

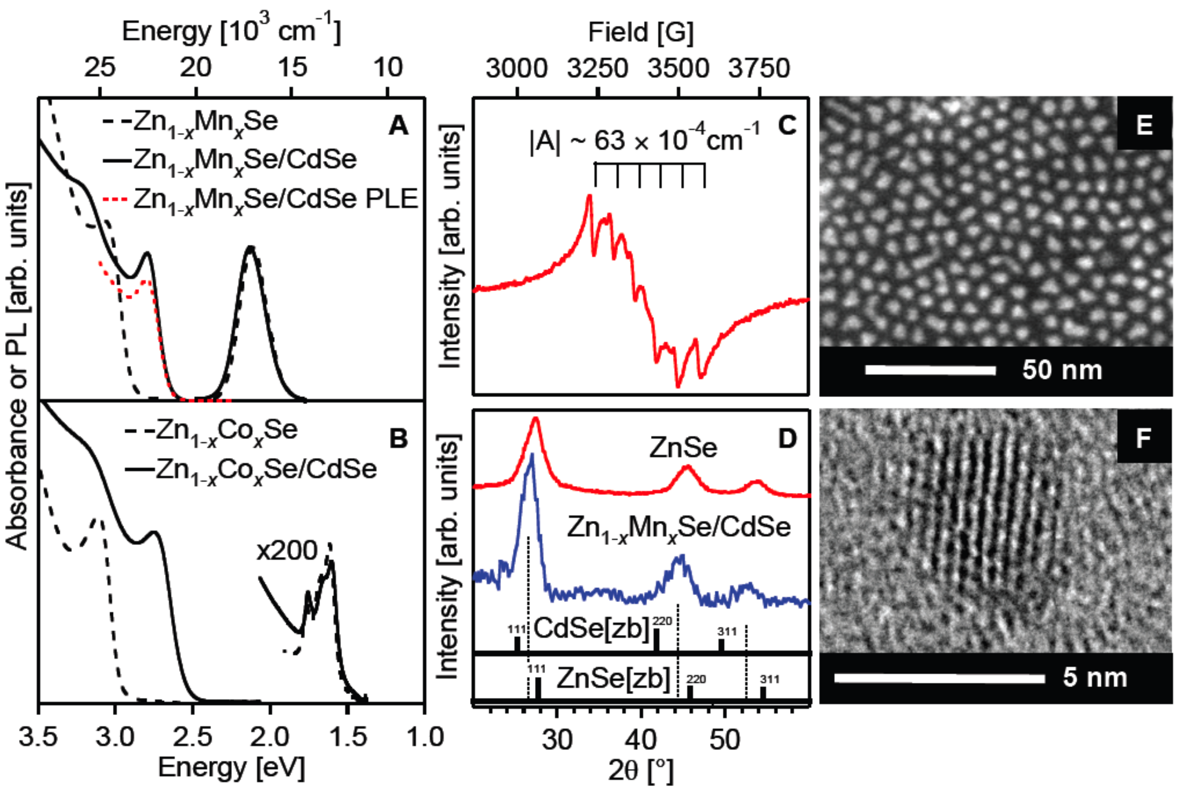

Figure 2.1. **(A)** Room-temperature absorption, photoluminescence, and photoluminescence excitation spectra of colloidal $Zn_{1-x}Mn_xSe$ core and $Zn_{1-x}Mn_xSe/CdSe$ core/shell nanocrystals (x = 0.016). The $Zn_{1-x}Mn_xSe$ absorption maximum corresponds to dia. ≈ 4.2 nm. **(B)** Room-temperature absorption spectra of analogous $Zn_{1-x}Co_xSe$ core and $Zn_{1-x}Co_xSe/CdSe$ core/shell nanocrystals (x = 0.005). **(C)** Room-temperature EPR spectrum of $Zn_{1-x}Mn_xSe/CdSe$ core/shell nanocrystals with 1.6 nm thick shells (x = 0.02). **(D)** Powder X-ray diffraction data for representative doped $Zn_{1-x}Co_xSe$ and $Zn_{1-x}Mn_xSe/CdSe$ nanocrystals, showing the lattice parameter shift with shell growth. **(E)** STEM and **(F)** TEM images of representative $Zn_{1-x}Mn_xSe/CdSe$ core/shell nanocrystals.

The magnitude of ΔE_{Zeeman} was estimated by analysis of such absorption and MCD spectra for each sample as detailed in ref. [45]. For the $Zn_{0.98}Mn_{0.02}Se$ nanocrystals of Fig. 2A, a Zeeman splitting energy of ΔE_{Zeeman} = -40 meV at saturation is obtained. Similar values have been reported previously for other colloidal Mn^{2+}-doped nanocrystals.[45]

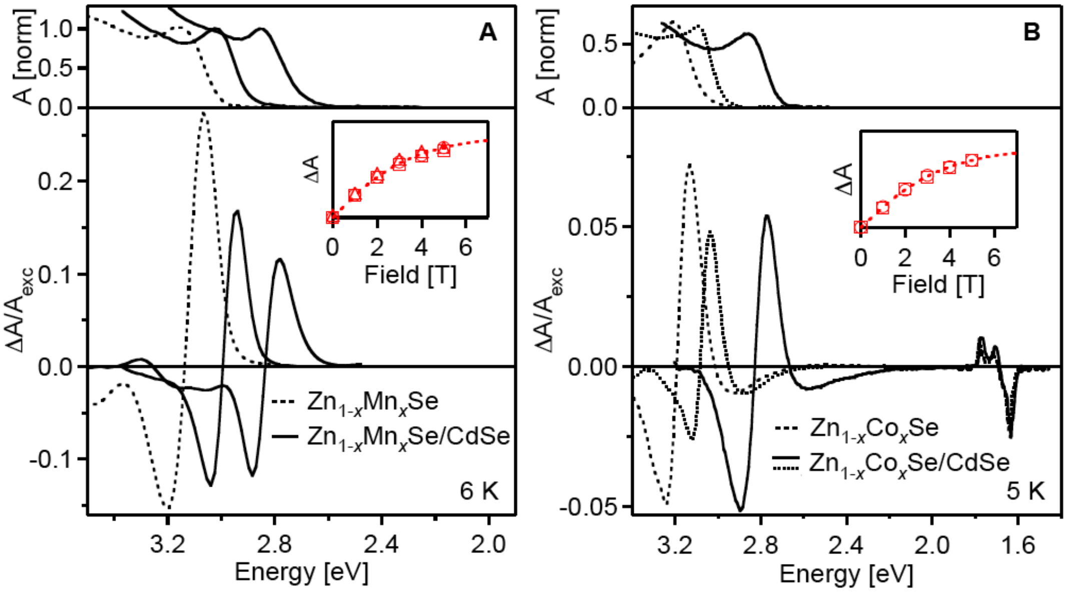

Figure 2.2. Absorption and 5 T MCD spectra of **(A)** $Zn_{0.98}Mn_{0.02}Se$ and $Zn_{0.98}Mn_{0.02}Se/CdSe$ nanocrystals (core dia. = 4.3 nm, r_S = 0.0, 0.3, and 0.5 nm), collected at 6 K, and **(B)** $Zn_{0.994}Co_{0.006}Se$ (dashed, dia. = 4.1), $Zn_{0.992}Co_{0.008}Se$ (dashed, dia. = 5.6 nm), and $Zn_{0.995}Co_{0.005}Se/CdSe$ (solid, core dia. = 3.9 nm, r_S = 0.55 nm) nanocrystals, collected at 5 K. All samples show MCD intensity saturation magnetization in agreement with the $S = 5/2$ (Mn^{2+}) or $S = 3/2$ (Co^{2+}) Brillion function at the experimental temperature (insets).

The shift of the excitonic feature to lower energy upon CdSe shell growth around these $Zn_{1-x}Mn_xSe$ core nanocrystals is accompanied by a decrease in the band-edge MCD intensity (Fig. 2.2A, solid), suggesting that ΔE_{Zeeman} is reduced. Figure 2.3A plots ΔE_{Zeeman} values obtained from quantitative analysis of the data of Fig. 2.2A, along with analogous data obtained from three additional series of core/shell samples built upon three independent core samples, with average core diameters all between 3.7 and 4.0 nm (see Supporting Information for sample details). The data for each series have been normalized to ΔE_{Zeeman} of the core nanocrystals of that series. For all samples, the magnitude of ΔE_{Zeeman} decreases smoothly with increasing shell thickness, approaching zero for the samples with the largest shells. Any dependence of this trend on core diameter is not discernable above the noise in this data set. The trend in Fig. 2.3A is similar to the one described previously,[30] but it is qualitatively at odds with the previous results in that inversion of the MCD sign for shell thicknesses of $r_S > \sim 0.2$ nm (sub-monolayer CdSe coverage) is not observed. This inversion was the key observation implicating confinement-induced kinetic *s-d* exchange, a possibility addressed in more detail below.

In the limit of infinitely thick CdSe shells around doped ZnSe nanocrystals, the Mn^{2+}-carrier spatial overlap approaches zero ($c_h = c_e = 0$ in eq 1), leaving only the small positive intrinsic contribution to ΔE_{Zeeman}. The asymptotic approach of ΔE_{Zeeman} to a very small value in the limit of large shell thicknesses in Fig. 2.3A is thus anticipated and easily understood. The behavior of ΔE_{Zeeman} in ZnSe/CdSe nanocrystals with thin or intermediate shells is more interesting, however. For certain core and shell dimensions, the ZnSe/CdSe band alignment may cause charge separation, with one carrier staying mainly inside the core and the other moving mainly into the shell. To test the role of the heterointerface experimentally, excitonic Zeeman splittings were measured for a series of isocrystalline $Zn_{1-x}Mn_xSe$/ZnSe core/shell nanocrystals (see Supporting Information), and the results of those experiments are also included in Fig. 2.3A. The striking observation is that the dependence of ΔE_{Zeeman} on shell thickness is essentially indistinguishable for $Zn_{1-x}Mn_xSe$/CdSe and $Zn_{1-x}Mn_xSe$/ZnSe core/shell nanocrystals, arguing against association of the trend in Fig. 2.3A with charge separation across a heterointerface. From these data, it is possible to conclude that the reduction of ΔE_{Zeeman} upon shell growth arises predominantly from relaxation of the h_{VB}^{+} probability density into the added shell volumes.

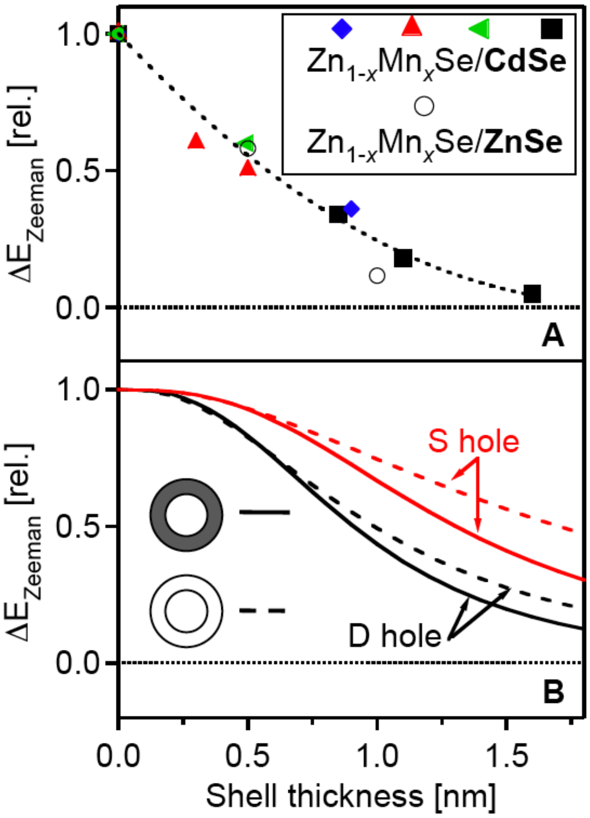

Figure 2.3. (A) Relative excitonic Zeeman splittings of core/shell nanocrystals at saturation, normalized to the splitting of the parent core for each series of samples: (◆ ,▲ ,■,◀) $Zn_{1-x}Mn_xSe/CdSe$ nanocrystals, (○) $Zn_{1-x}Mn_xSe/ZnSe$ nanocrystals. The dotted curve is a guide to the eye. See Supporting Information for sample details. All $Zn_{1-x}Mn_xSe$ core ΔE_{Zeeman} values fall within the range -45 to -30 meV at saturation. **(B)** Calculated effect of shell growth on $Zn_{1-x}TM_xSe$ QD Zeeman splitting energies, assuming bulk $Zn_{1-x}TM_xSe$ values of $N_0\alpha = +0.26$ eV and $N_0\beta = -1.11$ eV and bulk band offsets of -0.86 eV (CB) and +0.08 eV (VB).[47] Results for 3.4 nm diameter ZnSe cores are illustrated, and similar results are obtained for 4.0 nm diameter cores. Both CdSe and ZnSe shells are considered, with the CdSe shells having a larger effect for the same shell thickness. Increasing the hole D-orbital character increases the impact of shell growth, and the limiting curves for 0 and 100% D-orbital character are plotted. Note that the intrinsic contribution to ΔE_{Zeeman} is not included in these plots. This contribution will lead to an approximately constant negative offset whose relative magnitude depends upon the value of x (see eq 1). For the experimental doping levels studied here, this intrinsic contribution amounts to ~1% of the y scale of panel B.

2.4 Applying the spherical box model to calculate dopant-carrier overlap

For comparison with the experimental results of Fig. 2.3A, model calculations were performed for both ZnSe/CdSe and ZnSe/ZnSe nanocrystals. Accurate quantitative modeling is complicated by uncertainties in the hole angular momentum at the band edge,[48,49] the actual band offsets on these length scales,[50] the microstructure of the interface,[51] the effective surface potentials, and the large role that nanocrystal shape anisotropy must play. Bearing these uncertainties in mind, however, the effect of shell growth on ΔE_{Zeeman} in these nanocrystals can be explored using eq 1 in conjunction with wavefunction calculations executed within an effective mass approximation approach for idealized spherical crystallites with infinite potentials at their surfaces, as described previously.[11,12,14,30,49] For simplicity, bulk band offsets and effective masses were used in the calculations presented here. In the simplest approximation, the spatial parts of the wavefunctions of both the electron and the hole are 1S ($L = 0$) in character. In this limit, the electron shifts into the shell volume more easily than the hole does because the conduction band offset between ZnSe and CdSe is greater than the valence band offset, and because the electron is lighter than the hole.[11] Inclusion of 1D ($L = 2$) character in the hole wavefunction can be expected to enhance the transfer of hole probability density into the shell.[30] Because the ratio of S to D character appropriate for these experimental nanocrystals is unknown, overlap coefficients were calculated for the limiting cases of pure 1S and pure 1D hole wavefunctions, the real S-to-D ratio lying between these two limits. Dopant-carrier overlap coefficients (c_e and c_h from eq 1) were calculated as the integrated projections of the electron and hole probability densities onto the ZnSe core volumes. With these coefficients, the excitonic Zeeman splittings of various core/shell nanocrystals were then calculated relative to the core nanocrystals using eq 1, neglecting the intrinsic contribution to ΔE_{Zeeman} and assuming bulk values for $N_0\alpha$ and $N_0\beta$. The results of these calculations for ZnSe/CdSe nanocrystals are summarized in Fig. 3B (solid), and additional results are provided in Supporting Information.

Calculations performed for isocrystalline $Zn_{1-x}Mn_xSe$/ZnSe core/shell nanocrystals are also summarized in Fig. 2.3B (dashed).

For both the $Zn_{1-x}Mn_xSe$/CdSe and $Zn_{1-x}Mn_xSe$/ZnSe core/shell nanocrystals, the calculated results all show a gentle decrease in ΔE_{Zeeman} with increasing shell thickness that reproduces the experimental trends (Fig. 2.3A) reasonably well. The plateau at sub-monolayer shell thicknesses (one CdSe monolayer equals $r_S \sim 0.35$ nm) in Fig. 2.3B is an artifact of the idealized spherical shell model and does not appear in the experimental data set. The calculations suggest that both carriers expand into the shell volume to a very similar extent, but because of the large value of $N_0\beta$, the reduction of ΔE_{Zeeman} upon shell growth arises almost exclusively from the reduction of c_h upon shell addition. The precise extent of hole relaxation into the shell volume depends on the hole's D character and the identity of the shell material, but the calculated excitonic Zeeman splittings remain dominated by the h_{VB}^{+}-Mn^{2+} overlap. For example, in bulk $Zn_{1-x}Mn_xSe$, $|N_0\beta/N_0\alpha| \approx 4.8$ (ref. [31], where $c_e = c_h = 1$ in eq 1). When $L = 2$, the hole's probability density shifts into the shell volume somewhat quicker than the electron's, as suggested previously,[30] but $|(c_hN_0\beta)/(c_eN_0\alpha)| > 3.8$ for all scenarios examined here. When $L = 0$, the electron shifts to the shell slightly faster than the hole, and $|(c_hN_0\beta)/(c_eN_0\alpha)| > 4.8$ for all scenarios examined here. Using band offsets from experiments on nanocrystals[50] rather than from bulk samples increases these ratios. Overall, these calculations support the conclusion drawn above that the reduction of ΔE_{Zeeman} upon shell growth is governed entirely by hole relaxation into the shell volume, and is largely independent of whether the shell material is CdSe or ZnSe, or of the electron's response to shell growth.

2.5 The elusive kinetic *s-d* exchange

The data in reference 30 show an inversion of the $Zn_{1-x}Mn_xSe$ nanocrystal band-edge MCD sign upon shell growth that was interpreted as evidence of kinetic *s-d* exchange. The experimental results and analysis here have failed to yield such a sign change, warranting a closer examination of the conditions required to achieve and observe kinetic *s-d* exchange in such nanocrystals. The conclusion of dominant kinetic *s-d* exhange in ref. [30] was predicated on three necessary-but-not-sufficient conditions: (*i*) the inverted core/shell structure must withdraw sufficient hole density from the core before removal of electron density, such that the weaker *s-d* interaction becomes the dominant effect probed by MCD; (*ii*) quantum confinement must raise the conduction band edge energy by >~200 meV relative to bulk in order for it to approach resonance with the $Mn^{2+/+}$ acceptor level; and (*iii*) tacitly assumed, the $Mn^{2+}\text{-}e^-_{CB}$ transfer integral (V_{sd}) must be large enough for kinetic *s-d* exchange to dominate over the usual potential *s-d* exchange. We now examine each of these conditions individually.

The first condition has been addressed above: The data of Fig. 2.3A and the calculations of Fig. 3B suggest that the dominant *p-d* interaction in $Zn_{1-x}Mn_xSe/CdSe$ nanocrystals cannot be reduced sufficiently to make *s-d* exchange dominate ΔE_{Zeeman}, because hole transfer into the CdSe shell volume is at most only marginally greater than electron transfer even under the most favorable conditions (limit of pure D-orbital hole wavefunctions, bulk band offsets). The conclusion that $Zn_{1-x}Mn_xSe/CdSe$ excitonic Zeeman splittings remain dominated by *p-d* interactions is supported by the very similar results obtained for $Zn_{1-x}Mn_xSe/ZnSe$ samples (Fig. 3A).

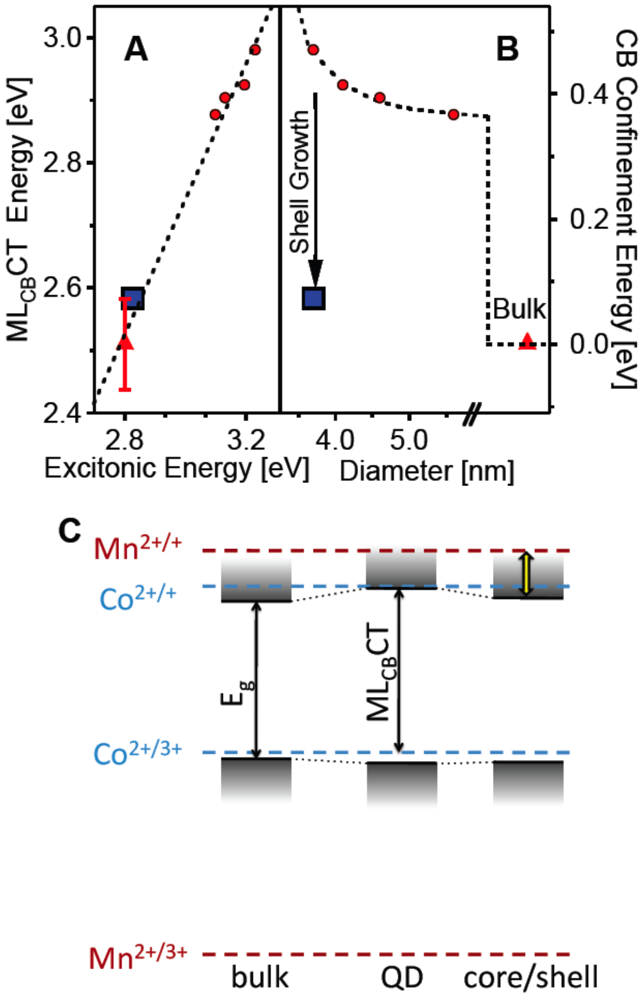

Figure 2.4. (A) Relationship between the Co^{2+} → CB charge transfer ($ML_{CB}CT$) transition energy and the excitonic energy of a series of $Zn_{1-x}Co_xSe$ (●) nanocrystals, determined from MCD spectroscopy (e.g., Fig. 2B). The best-fit line yields a slope of ~0.75 that reflects the electron effective mass in the $ML_{CB}CT$ excited state (ref. 35). The ▲ symbol indicates the approximate energy of the $ML_{CB}CT$ transition in bulk $Zn_{1-x}Co_xSe$.[35,52-56] The $ML_{CB}CT$ energy of the $Zn_{1-x}Co_xSe$/CdSe core/shell nanocrystals (■) from Fig. 2B falls on the same line. **(B)** Data from part (A) re-plotted as conduction band confinement energy vs ZnSe nanocrystal diameter, referenced to bulk ZnSe. The experimental results indicate that CdSe shell growth (arrow) around the smallest ZnSe nanocrystals stabilizes the e^-_{CB}, bringing its potential close to that of bulk ZnSe in the $Zn_{1-x}Co_xSe$/CdSe core/shell nanocrystals of Fig. 2B (core dia. = 3.9 nm, r_S = 1.1 nm). **(C)** Energy diagram illustrating VB and CB positions relative to the TM^{2+} donor and acceptor levels for bulk and quantum confined $Zn_{1-x}TM_xSe$ and $Zn_{1-x}TM_xSe$/CdSe nanocrystals. The bold yellow double-arrow shows the relevant energy splitting for the confinement-induced kinetic *s-d* exchange for Mn^{2+} dopants ($\Delta E(Mn^{2+/+}-E(e^-_{CB}))$).

2.5.A Focusing on the conduction band with the $Co^{2+} \rightarrow CB$ *charge-transfer transition*

Even if sufficient hole extraction could be achieved without also extracting the electron, the other two conditions must also be met in order for kinetic *s-d* exchange to be observed in the MCD experiment. Chemical reasoning suggests that the large exciton red shift observed upon CdSe shell growth around the ZnSe nanocrystal cores (Fig. 1A,B) derives from stabilization of the CB by addition of Cd^{2+}. CdSe shell growth is therefore hypothesized to quench the needed electron confinement energies in ZnSe/CdSe nanocrystals. To test this hypothesis, a series of $Zn_{1-x}Co_xSe$ and $Zn_{1-x}Co_xSe$/CdSe nanocrystals was prepared for examination by MCD spectroscopy. The appearance of a sub-bandgap $Co^{2+} \rightarrow$ CB charge-transfer transition (*i.e.*, $ML_{CB}CT$, or donor-type photoionization transition) in the MCD spectra of $Zn_{1-x}Co_xSe$ nanocrystals whose energy reflects the confinement-induced shift in the CB edge energy has been described previously.[35] Here, this optical charge-transfer transition is used as an internal probe of the change in the electron confinement energy upon CdSe shell growth in $Zn_{1-x}Co_xSe$/CdSe nanocrystals.

Figure 2B shows electronic absorption and MCD spectra collected for a series of $Zn_{1-x}Co_xSe$ and $Zn_{1-x}Co_xSe$/CdSe nanocrystals. Whereas the $^4T_1(P)$ ligand field band is to first order independent of core and shell dimensions, the sub-bandgap $ML_{CB}CT$ transition shifts to lower energy when either the ZnSe core diameter increases or the CdSe shell is added. Figure 4A plots the energy of this $ML_{CB}CT$ transition versus that of the first excitonic feature for the entire set of $Zn_{1-x}Co_xSe$ and $Zn_{1-x}Co_xSe$/CdSe nanocrystals. This plot yields a straight line across the whole series of $Zn_{1-x}Co_xSe$ and $Zn_{1-x}Co_xSe$/CdSe nanocrystal samples, extrapolating close to the estimated bulk charge-transfer energy.[35] The slope of this line, $\Delta E_{MLCT}/\Delta E_{EXC} \approx 0.75$, reflects the effective mass of the CB electron in this charge-transfer excited state.[35] Importantly, this plot shows that the CB energy of the $Zn_{1-x}Co_xSe$/CdSe nanocrystals is close to the CB energy of bulk $Zn_{1-x}Co_xSe$, *i.e.*, that CdSe shell growth quenches the confinement energy of the CB electron in the ZnSe core. For illustration, the data in Fig. 4A are re-plotted in Fig. 4B relative to the bulk conduction band energy,[35] emphasizing the large stabilization of the ZnSe nanocrystal CB energy upon CdSe shell growth. In the recent report of kinetic *s-d* exchange,[30] the required CB confinement energy was estimated to be >~200 meV, and a CB confinement energy within the inverted core/shell nanocrystals of ~400 meV was estimated from consideration of the $Zn_{1-x}Mn_xSe$ core alone. With the demonstration here that the electron confinement energies of ZnSe nanocrystals are strongly quenched by CdSe shell growth, it appears unlikely that the necessary strong electron confinement can be achieved in ZnSe/CdSe nanocrystals with shells that are also sufficiently thick to extract the holes.

2.5.B Co^{2+} is expected to have larger kinetic s-d exchange than Mn^{2+}

It is interesting to note that the $Co^{2+/+}$ acceptor level in ZnSe is believed to be nearly degenerate with the ZnSe CB edge,[57,58] > 0.5 eV below the corresponding $Mn^{2+/+}$ level (cf. Fig. 4C), and in excellent energetic proximity for resonant mixing with the ZnSe CB edge wavefunction. By switching from Mn^{2+} to Co^{2+}, an even greater reduction of the energy difference $\Delta E(TM^{2+/+}$-$E(e^-_{CB}))$ (or $\varepsilon^- - E_e$ in ref. 33) governing this interaction has thus been achieved than was accessible via quantum confinement in the $Zn_{1-x}Mn_xSe$ core nanocrystals. $Zn_{1-x}Co_xSe$ and $Zn_{1-x}Co_xSe$/CdSe nanocrystals are therefore both much better positioned to display strong kinetic *s-d* exchange than the corresponding Mn^{2+}-doped nanocrystals. Importantly, the d^7 configuration of Co^{2+} also provides identical $3d(t_2)$-e^-_{CB} exchange pathways as Mn^{2+}, making direct comparison particularly straightforward. This reduction in $\Delta E(TM^{2+/+}$-$E(e^-_{CB}))$ for Co^{2+} is estimated to increase the kinetic *s*-*d* exchange magnitude by a factor of >~4 relative to comparable $Zn_{1-x}Mn_xSe$ nanocrystals in the size regime investigated here, which if correct would cause the *s*-*d* coupling to exceed the *p*-*d* exchange energy such that MCD sign inversion should occur in $Zn_{1-x}Co_xSe$ nanocrystals even without carrier separation. Despite this major advantage, MCD sign inversion is still not observed in either $Zn_{1-x}Co_xSe$ or $Zn_{1-x}Co_xSe$/CdSe nanocrystals (Fig. 2B), nor is there any obvious difference between the Zeeman properties of the Co^{2+}- and Mn^{2+}-doped nanocrystals that might suggest stronger kinetic *s*-*d* exchange in the former.

2.5.C Apparently kinetic s-d exchange is small

The above results argue against interpretation of the MCD sign inversion in ref. [30] in terms of the kinetic *s*-*d* exchange model of ref. [33], and call into question the order of magnitude of the kinetic *s*-*d* exchange effects predicted by that model for quantum dots. The absence of strong kinetic *s*-*d* exchange despite nearly perfect energetic resonance conditions in the Co^{2+}-doped nanocrystals suggests that the transfer integral that governs this exchange interaction must remain small despite the relaxation of symmetry constraints via quantum confinement described in ref. [33]. Although kinetic *s*-*d* exchange is undoubtedly allowed in these doped nanocrystals because of mechanisms such as those described in ref. [33], it evidently exists only as a weak perturbation to the already small potential *s*-*d* exchange interaction.

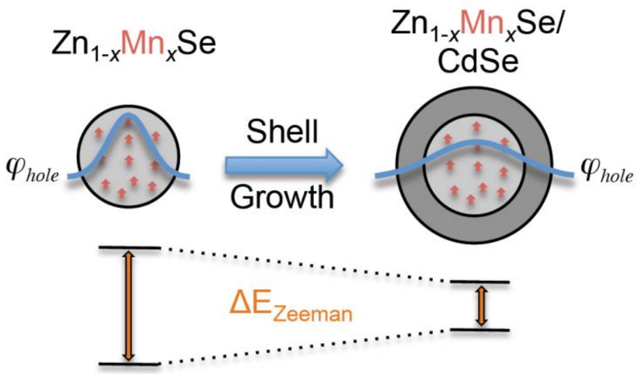

Scheme 1.

2.6 Summary

Spectroscopic investigations into the electronic structures of a series of $Zn_{1-x}TM_xSe$ core, $Zn_{1-x}TM_xSe$/CdSe inverted core/shell, and $Zn_{1-x}TM_xSe$/ZnSe isocrystalline core/shell colloidal nanocrystals doped with Co^{2+} or Mn^{2+} have provided an experimental description of the influence of shell growth on dopant-carrier magnetic exchange interactions in these interesting materials. Evidence for confinement-induced modification of the fundamental exchange parameters could not be found either experimentally or through modeling. Specifically, kinetic *s*-*d* exchange coupling could not be confirmed, and analysis suggests that it will not likely be observed in $Zn_{1-x}Mn_xSe$/CdSe inverted core/shell nanocrystals: (*i*) shell growth causes insufficient hole extraction from the cores to make the *s-d* interaction dominate the excitonic Zeeman splitting; and (*ii*) large electron stabilization upon shell growth quenches the strong confinement required for the electron to approach energetic resonance with the $Mn^{2+/+}$ acceptor level. The absence of detectable kinetic *s-d* exchange effects even in $Zn_{1-x}Co_xSe$ and $Zn_{1-x}TM_xSe$/CdSe nanocrystals leads us to suggest that the TM^{2+}-e^-_{CB} transfer integrals remain vanishingly small despite any formal relaxation of symmetry restrictions through quantum confinement. The primary result of shell growth in both $Zn_{1-x}TM_xSe$/CdSe and $Zn_{1-x}TM_xSe$/ZnSe nanocrystals is to allow expansion of hole probability densities into the new shell volumes, which diminishes the *p-d* interactions that nevertheless continue to dominate the excitonic Zeeman splittings (Scheme 1). In this sense, the spectroscopic effect of shell growth around doped cores is the same as that observed in core/shell nanocrystals with doped shells, where dopant-carrier overlap is also diminished relative to nanocrystals with uniform dopant distributions by reduction of the hole-dopant projection coefficient, c_h.[24,36] These experimental results shed new light on the role of shell growth in modifying dopant-carrier magnetic exchange interactions in colloidal doped core/shell nanocrystals and challenge our understanding of the role quantum confinement plays in altering fundamental mechanisms of dopant-carrier magnetic exchange coupling on these length scales.

2.7 Methods

2.7.A Synthesis

ZnSe nanocrystals doped with either Mn^{2+} or Co^{2+} were prepared by adapting the procedure reported recently for doping CdSe nanocrystals.[1,2] The inorganic cluster $(Me_4N)_2[Zn_4(SePh)_{10}]$ was prepared using procedures adapted from ref. [3]. This cluster was synthesized at room temperature under inert (N_2) conditions by addition of $Zn(NO_3)_2 \cdot 4H_2O$ (17 mmol) in methanol (16.8 mL) to an equimolar solution of triethylamine and benzeneselenol (44 mmol) in methanol (9.6 mL). A solution of tetramethylammonium chloride (19.3 mmol) in methanol (9.6 mL) was added, and the mixture was allowed to crystallize at 0°C under N_2. The crystalline product was filtered, washed repeatedly with methanol, and dried under vacuum.

Mn^{2+}-doped ZnSe nanocrystals were synthesized from $(Me_4N)_2[Zn_4(SePh)_{10}]$ as follows: 10.8 g of hexadecylamine and 0.01 g of $MnCl_2•4H_2O$ were degassed under vacuum at 130 ºC for 1.5 h. The temperature was dropped to <80ºC, at which point 0.19 g of $(Me_4N)_2[Zn_4(SePh)_{10}]$ and 0.019 g of Se metal were added to the reaction. The temperature was increased and kept at 130 ºC for 1.5 h under N_2 to dissolve the solids. After the solids had dissolved, the temperature was increased to 280 ºC and the nanocrystals were allowed to grow for 1.0 to 2.5 h in order to reach the desired size. Co^{2+}-doped ZnSe nanocrystals were prepared in an analogous fashion using $CoCl_2$ as the dopant precursor.

$Zn_{1-x}TM_xSe$/CdSe core/shell nanocrystals were prepared using methods adapted from ref. 12. In a typical synthesis, 0.01 mmol of $Zn_{1-x}TM_xSe$ nanocrystals (determined by electronic absorption) in hexane were added to a reaction solution containing 4.5 g of octadecene and 0.5 g oleylamine. The shell nutrient solution was prepared separately by mixing 0.1 mmol of Se metal dissolved in 1 mL trioctylphosphine with a 0.1 M cadmium oleate solution, prepared by heating CdO in octadecene and oleic acid under N_2. The nanocrystals were heated to 200ºC under N_2, at which point the growth solution was added dropwise over a period of 10 to 60 minutes to reach the desired shell thickness. ZnSe shells were grown in the same way, but at 240-250ºC.

2.7.B. Physical characterization

Powder X-ray diffraction (XRD) data were collected using a 12 kW Rigaku Rotaflex RTP300 X-ray diffractometer. All cation concentrations (Zn^{2+}, Cd^{2+}, Co^{2+}, and Mn^{2+}) were determined quantitatively using inductively coupled plasma atomic emission spectrometry (ICP-AES, Jarrel Ash model 955) after acid digestion of the samples. Shell thicknesses were estimated from the analytical Cd:Zn ratios and the known ZnSe core dimensions assuming spherical average geometries for both core and core/shell particles. Continuous wave (CW) electron paramagnetic resonance (EPR) spectra were recorded at room temperature on a Bruker E580 spectrometer with X-band microwave sources (~9.5 GHz). Room-temperature absorption spectra of colloidal nanocrystals were collected using 1 cm cuvettes and a Cary 500 (Varian) spectrophotometer. Luminescence spectra were measured in 1 cm x 1 cm fluorescence cuvettes on a Jobin Yvon FluoroMax-2 fluorimeter. Low-temperature electronic absorption and magnetic circular dichroism (MCD) measurements were collected on high optical quality glasses of the colloidal nanocrystals. Low-temperature absorption and MCD spectra were collected simultaneously using an Aviv 40DS spectropolarimeter and a high-field superconducting magneto-optical cryostat (Cryo-Industries SMC–1659 OVT) positioned in the Faraday configuration. MCD intensities were measured as the differential absorbance $\Delta A = A_L - A_R$ where A_L and A_R refer to the absorption of left and right circularly polarized photons following the sign convention of Piepho and Schatz.[6]

2.7.C. Calculations

The e^-_{CB} and h^+_{VB} wavefunctions were calculated following the spherical-box approach outlined by Haus *et al.*[7] In general, the wavefunctions must satisfy the time-independent Schrödinger equation (eq 2).

$$-\frac{h^2}{2m_{carrier}}\nabla^2\Psi_{carrier} + V_{carrier}(r)\Psi_{carrier} = E\Psi_{carrier} \qquad (2)$$

The carrier effective masses, $m_{carrier}$, were taken as their bulk values: ZnSe, $m_e = 0.14$, $m_h = 0.53$; CdSe, $m_e = 0.13$, $m_h = 0.45$.[8,9] The e^-_{CB} and h^+_{VB} offset potentials were modeled as step functions using the ZnSe-to-CdSe bulk band offsets (ΔV): -0.86 eV for e^{-}_{CB}, and +0.08 eV for h^{+}_{VB}.[10]

Equation 2 was then solved for the two regions on either side of the step. For a constant potential V, the general solution to the radial part of the wavefunction is a linear combination of spherical Bessel and Neumann of the first and second kind ($j_l(r)$ and $n_l(r)$, respectively), and the angular solutions are the spherical harmonics ($Y_{l,m}(\theta,\phi)$). Thesolutions for the two regions are combined by imposing continuity and differentiability (more precisely, continuity of the probability current) at the interface. The total wavefunction for each carrier is given by eq 3, where $H(r\text{-}r_i)$ is the Heaviside function.

$$\begin{aligned}\Psi_{total} = {} & [(1-H(r-r_{core}))\times(A_l^{core} j_l(k^{core}r)+B_l^{core} n_l(k^{core}r)) \\ & +H(r-r_{core})\times(A_l^{shell} j_l(k^{shell}r)+B_l^{shell} n_l(k^{shell}r))]\mathrm{Y}_{l,m}(\theta,\phi)\end{aligned} \qquad (3)$$

where $$k^{core}=\sqrt{\frac{2m_{carrier}(E-V^{core})}{h^2}}\,,\ k^{shell}=\sqrt{\frac{2m_{carrier}(E-V^{shell})}{h^2}}$$

This wavefunction has five unknowns, including E. These unknowns are determined using the four boundary conditions and normalization. Besides continuity and differentiability at the core/shell interface, the wavefunction is taken to be zero at the edge of the shell and bounded at the origin. The solution given in eq 3 is valid for all l values. Only $l = 0$ was considered for the electron, whereas both $l = 0$ and $l = 2$ were considered for the hole. In early studies of ZnSe/CdSe inverted core/shell nanocrystals, the hole was modeled using only $l = 0$, and the electron was concluded to shift to the shell volume first.[4,11,12] Accounting for the $l = 2$ character of the hole, it has more recently been suggested that the hole departs first, followed by the electron.[13] Here, we neglect the effects of heavy- and light-hole level mixing, under which the $l =$

0 and l = 2 radial wavefunctions would each have to be described by a combination of two Bessel functions with different k^i (i = core or shell) values (for the different effective masses of the heavy-hole (m_{hh}) and light-hole (m_{lh})). Figure 2.5 shows the effect of growing a ZnSe shell onto a 3.4 nm ZnSe core for the unmixed and the mixed l = 2 wavefunctions. The unmixed wavefunction consists of a pure l = 2 Bessel function of the first kind (using $m_h = 0.53$) and the mixed wavefunction consists of the l = 2 part of the radial hole wavefunction ($m_{hh} = 0.859$, $m_{lh} = 0.121$), demonstrating that the effect of that mixing on the hole spatial probability density is small.

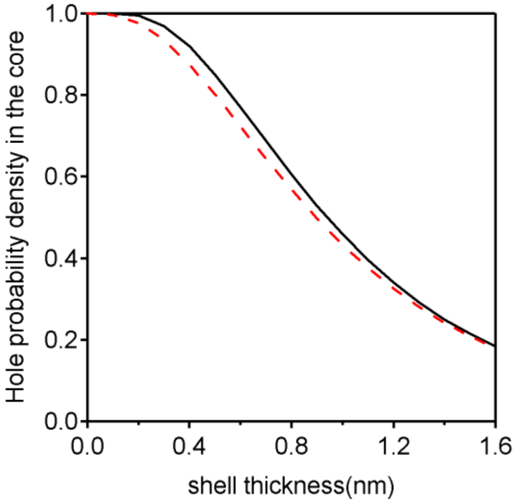

Figure 2.5. Hole probability density in the 3.4 nm ZnSe core as a function of ZnSe shell thickness for the l=2 components of the mixed(black) and unmixed(red) hole wavefunctions.

2.8 References

1 Reiss, P., Protière, M., & Li, L., Core/shell semiconductor nanocrystals. *Small* **5**, 154-168 (2009).

2 van Embden, J., Jasieniak, J., Gómez, D.E., Mulvaney, P., & Giersig, M., Review of the Synthetic Chemistry Involved in the Production of Core/Shell Semiconductor Nanocrystals. *Aust. J. Chem.* **60**, 457-471 (2007).

3 Hines, M.A. & Guyot-Sionnest, P., Synthesis and Characterization of Strongly Luminescing ZnS-Capped CdSe Nanocrystals. *J. Phys. Chem.* **100**, 468-471 (1996).

4 Dabbousi, B.O., Rodriguez-Viejo, J., Mikulec, F.V., Heine, J.R., Mattoussi, H., Ober, R., Jensen, K.F., & Bawendi, M.G., (CdSe)ZnS Core-Shell Quantum Dots: Synthesis and Characterization of a Size Series of Highly Luminescent Nanocrystallites. *J. Phys. Chem. B* **101**, 9463-9475 (1997).

5 Peng, X., Schlamp, M.C., Kadavanich, A.V., & Alivisatos, A.P., Epitaxial Growth of Highly Luminescent CdSe/CdS Core/Shell Nanocrystals with Photostability and Electronic Accessibility. *J. Am. Chem. Soc.* **119**, 7019-7029 (1997).

6 Pandey, A. & Guyot-Sionnest, P., Slow Electron Cooling in Colloidal Quantum Dots. *Science* **322**, 929-932 (2008).

7 Mahler, B., Spinicelli, P., Buil, S., Quelin, X., Hermier, J.-P., & Dubertret, B., Towards non-blinking colloidal quantum dots. *Nature Mater.* **7**, 659-664 (2008).

8 Chen, Y., Vela, J., Htoon, H., Casson, J.L., Werder, D.J., Bussian, D.A., Klimov, V.I., & Hollingsworth, J.A., "Giant" Multishell CdSe Nanocrystal Quantum Dots with Suppressed Blinking. *J. Am. Chem. Soc.* **130**, 5026-5027 (2008).

9 García-Santamaría, F., Chen, Y., Vela, J., Schaller, R.D., Hollingsworth, J.A., & Klimov, V.I., Suppressed Auger Recombination in "Giant" Nanocrystals Boosts Optical Gain Performance. *Nano Lett.*, ASAP (DOI:10.1021/nl901681d) (2009).

10 Kim, S., Fisher, B., Eisler, H.-J., & Bawendi, M.G., Type-II Quantum Dots: CdTe/CdSe(Core/Shell) and CdSe/ZnTe(Core/Shell) Heterostructures. *J. Am. Chem. Soc.* **125**, 11466-11467 (2003).

11 Balet, L.P., Ivanov, S.A., Piryatinski, A., Achermann, M., & Klimov, V.I., Inverted Core/Shell Nanocrystals Continuously Tunable between Type-I and Type-II Localization Regimes. *Nano Lett.* **4**, 1485-1488 (2004).

12 Zhong, X., Xie, R., Zhang, Y., Basché, T., & Knoll, W., High-Quality Violet- to Red-Emitting ZnSe/CdSe Core/Shell Nanocrystals. *Chem. Mater.* **17**, 4038-4042 (2005).

13 Nanda, J., Ivanov, S.A., Htoon, H., Bezel, I., Piryatinski, A., Tretiak, S., & Klimov, V.I., Absorption cross sections and Auger recombination lifetimes in inverted core-shell nanocrystals: Implications for lasing performance. *J. Appl. Phys.* **99**, 034309 (2006).

14 Piryatinski, A., Ivanov, S.A., Tretiak, S., & Klimov, V.I., Effect of Quantum and Dielectric Confinement on the Exciton-Exciton Interaction Energy in Type II Core/Shell Semiconductor Nanocrystals. *Nano Lett.* **7**, 108-115 (2007).

15 Yang, H. & Holloway, P.H., Electroluminescence from Hybrid Conjugated Polymer-CdS:Mn/ZnS Core/Shell Nanocrystals Devices. *J. Phys. Chem. B* **107**, 9705-9710 (2003).

16 Yang, H. & Holloway, P.H., Efficient and Photostable ZnS-Passivated CdS:Mn Luminescent Nanocrystals. *Adv. Funct. Mater.* **14**, 152-156 (2004).

17 Yang, Y., Chen, O., Angerhofer, A., & Cao, Y.C., Radial-Position-Controlled Doping in CdS/ZnS Core / Shell Nanocrystals. *J. Am. Chem. Soc.* **128**, 12428-12429 (2006).

18 Thakar, R., Chen, Y., & Snee, P.T., Efficient Emission from Core/(Doped) Shell Nanoparticles: Applications for Chemical Sensing. *Nano Lett.* **7**, 3429-3432 (2007).

19 Yang, Y., Chen, O., Angerhofer, A., & Cao, Y.C., On Doping CdS/ZnS Core/Shell Nanocrystals with Mn. *J. Am. Chem. Soc.* **130**, 15649–15661 (2008).

20 Wood, V., Halpert, J.E., Panzer, M.J., Bawendi, M.G., & Bulović, V., Alternating Current Driven Electroluminescence from ZnSe/ZnS:Mn/ZnS Nanocrystals. *Nano Lett.* **9**, 2367–2371 (2009).

21 Erwin, S.C., Zu, L.J., Haftel, M.I., Efros, A.L., Kennedy, T.A., & Norris, D.J., Doping semiconductor nanocrystals. *Nature* **436**, 91-94 (2005).

22 Wang, S., Jarrett, B.R., Kauzlarich, S.M., & Louie, A.Y., Core/Shell Quantum Dots with High Relaxivity and Photoluminescence for Multimodality Imaging. *J. Am. Chem. Soc.* **129**, 3848-3856 (2007).

23 Ithurria, S., Guyot-Sionnest, P., Mahler, B., & Dubertret, B., Mn^{2+} as a Radial Pressure Gauge in Colloidal Core/Shell Nanocrystals. *Phys. Rev. Lett.* **99**, 265501 (2007).

24 Archer, P.I., Santangelo, S.A., & Gamelin, D.R., Inorganic Cluster Syntheses of TM^{2+}-Doped Quantum Dots (CdSe, CdS, CdSe/CdS): Physical Property Dependence on Dopant Locale. *J. Am. Chem. Soc.* **129**, 9808-9818 (2007).

25 Radovanovic, P.V. & Gamelin, D.R., Electronic Absorption Spectroscopy of Cobalt Ions in Diluted Magnetic Semiconductor Quantum Dots: Demonstration of an Isocrystalline Core/Shell Synthetic Method. *J. Am. Chem. Soc.* **123**, 12207-12214 (2001).

26 Radovanovic, P.V., Norberg, N.S., McNally, K.E., & Gamelin, D.R., Colloidal Transition-Metal-Doped ZnO Quantum Dots. *J. Am. Chem. Soc.* **124**, 15192-15193 (2002).

27 Pradhan, N., Goorskey, D., Thessing, J., & Peng, X., An Alternative of CdSe Nanocrystal Emitters: Pure and Tunable Impurity Emissions in ZnSe Nanocrystals. *J. Am. Chem. Soc.* **127**, 17586-17587 (2005).

28 Cao, L., Zhang, J., Ren, S., & Huang, S., Luminescence Enhancement of Core-Shell ZnS:Mn/ZnS Nanoparticles. *Appl. Phys. Lett.* **80**, 4300-4302 (2002).

29 Quan, Z., Wang, Z., Yang, P., Lin, J., & Fang, J., Synthesis and Characterization of High-Quality ZnS, $ZnS:Mn^{2+}$, and $ZnS:Mn^{2+}/ZnS$ (Core/Shell) Luminescent Nanocrystals. *Inorg. Chem.* **46**, 1354-1360 (2007).

30 Bussian, D.A., Crooker, S.A., Yin, M., Brynda, M., Efros, A.L., & Klimov, V.I., Tunable magnetic exchange interactions in manganese-doped inverted core–shell ZnSe–CdSe nanocrystals. *Nature Mater.* **8**, 35-40 (2009).

31 Furdyna, J.K. & Kossut, J. eds., Diluted Magnetic Semiconductors. (Academic, N.Y., 1988).

32 Kacman, P., Spin Interactions in Diluted Magnetic Semiconductors and Magnetic Semiconductor Structures. *Semicond. Sci. Technol.* **16**, R25-R39 (2001).

33 Merkulov, I.A., Yakovlev, D.R., Keller, A., Ossau, W., Geurts, J., Waag, A., Landwehr, G., Karczewski, G., Wojtowicz, T., & Kossut, J., Kinetic Exchange between the Conduction Band Electrons and Magnetic Ions in Quantum-Confined Structures. *Phys. Rev. Lett.* **83** (7), 1431-1434 (1999).

34 Stern, N.P., Myers, R.C., Poggio, M., Gossard, A.C., & Awschalom, D.D., Confinement engineering of s-d exchange interactions in $Ga_{1-x}Mn_xAs/Al_yGa_{1-y}As$ quantum wells. *Phys. Rev. B* **75**, 045329 (2007).

35 Norberg, N.S., Dalpian, G.M., Chelikowsky, J.R., & Gamelin, D.R., Energetic Pinning of Magnetic Impurity Levels in Quantum Confined Semiconductor Nanocrystals. *Nano Lett.* **6**, 2887-2892 (2006).

36 Norberg, N.S., Parks, G.L., Salley, G.M., & Gamelin, D.R., Giant Excitonic Zeeman Splittings in Co^{2+}-doped ZnSe Quantum Dots. *J. Am. Chem. Soc.* **128**, 13195-13203 (2006).

37 Norris, D.J., Yao, N., Charnock, F.T., & Kennedy, T.A., High-Quality Manganese-Doped ZnSe Nanocrystals. *Nano Lett.* **1**, 3-7 (2001).

38 Suyver, J.F., Wuister, S.F., Kelly, J.J., & Meijerink, A., Luminescence of Nanocrystalline $ZnSe:Mn^{2+}$. *Phys. Chem. Chem. Phys.* **2**, 5445-5448 (2000).

39 Ivanov, S.A., Nanda, J., Piryatinski, A., Achermann, M., Balet, L.P., Bezel, I.V., Anikeeva, P.O., Tretiak, S., & Klimov, V.I., Light Amplification Using Inverted Core/Shell Nanocrystals: Towards Lasing in the Single-Exciton Regime. *J. Phys. Chem. B* **108**, 10625-10630 (2004).

40 Ludwig, G.W. & Woodbury, H.H., in *Solid State Physics*, edited by F. Seitz & D. Turnbull (Academic Press, New York, 1962), Vol. 13, pp. 298.

41 Ando, K., Yamada, Y., & Shakin, V.A., Magneto-optical study of quantum confinement in Cd(S,Se) quantum dots. *Phys. Rev. B* **47**, 13462-13465 (1993).

42 Kuno, M., Nirmal, M., Bawendi, M.G., Efros, A., & Rosen, M., Magnetic Circular Dichroism Study of CdSe Quantum Dots. *J. Chem. Phys.* **108**, 4242-4247 (1998).

43 Hoffman, D.M., Meyer, B.K., Ekimov, A.I., Merkulov, I.A., Efros, A.L., Rosen, M., Counio, G., Gacoin, T., & Boilot, J.-P., Giant Internal Magnetic Fields in Mn Doped Nanocrystal Quantum Dots. *Sol. State Comm.* **114**, 547-550 (2000).

44 Archer, P.I., Santangelo, S.A., & Gamelin, D.R., Direct Observation of sp-d Exchange Interactions in Colloidal Mn^{2+}- and Co^{2+}-doped CdSe Quantum Dots. *Nano Lett.* **7**, 1037-1043 (2007).

45 Beaulac, R., Ochsenbein, S.T., & Gamelin, D.R., Colloidal Transition-Metal-Doped Quantum Dots in *Semiconductor and Metal Nanocrystals (2nd edition)*, edited by V. I. Klimov (2009), pp. in press.

46 Bacher, G., Optical Spectroscopy on Epitaxially Grown II–VI Single Quantum Dots (review). *Topics Appl. Phys.* **90**, 147-185 (2003).

47 Heinrich, H. & Langer, J.M., Band Offsets in Heterostructures in *Advances in Solid State Physics*, edited by P. Grosse (Springer, Berlin, 1986), Vol. 26, pp. 251-275.

48 Efros, A.L., Luminescence polarization of CdSe microcrystals. *Phys. Rev. B* **46**, 7448-7458 (1992).

49 Haus, J.W., Zhou, H.S., Honma, I., & Komiyama, H., Quantum confinement in semiconductor heterostructure nanometer-size particles. *Phys. Rev. B* **47**, 1359-1365 (1993).

50 Pandey, A. & Guyot-Sionnest, P., Intraband spectroscopy and band offsets of colloidal II-VI core/shell structures. *J. Chem. Phys.* **127**, 104710 (2007).

51 Yu, Z.G., Guo, L., Du, H., Krauss, T., & Silcox, J., Shell Distribution on Colloidal CdSe/ZnS Quantum Dots. *Nano Lett.* **5**, 565-570 (2005).

52 Robbins, D.J., Dean, P.J., Glasper, J.L., & Bishop, S.G., New high-energy luminescence bands from Co^{2+} in ZnSe. *Solid State Comm.* **36** (1), 61-67 (1980).

53 Noras, J.M., Szawelska, H.R., & Allen, J.W., Energy levels of cobalt in ZnSe and ZnS. *J. Phys. C* **14**, 3255-3268 (1981).

54 Sokolov, V.I., Surkova, T.P., Kulakov, M.P., & Fadeev, A.V., New Experimental Evidence Concerning the Nature of L, M, and N Lines in ZnSe:Co. *Phys. Stat. Solidi (b)* **130** (1), 267-272 (1985).

55 Ehlert, A., Dreyhsig, J., Gumlich, H.-E., & Allen, J.W., Excited-state absorption of ZnSe doped with cobalt. *J. Lumin.* **60-61**, 21-25 (1994).

56 Dreyhsig, J., Configuration-interaction energy level diagrams for d^7 and d^8 charge-state impurities in II-VI and III-V compound semiconductors. *J. Phys. Chem. Solids* **59**, 31-42 (1998).

57 Blinowski, J., Kacman, P., & Dietl, T., Kinetic Exchange vs. Room Temperature Ferromagnetism in Diluted Magnetic Semiconductors. *Mat. Res. Soc. Symp. Proc.* **690**, 109-114 (2002).

58 Dietl, T., Spin order manipulations in nanostructures of II–VI ferromagnetic semiconductors. *J. Mag. Mag. Mater.* **272-276**, 1969–1973 (2004).

Chapter 3: Tunable Dual Emission in Doped Semiconductor Nanocrystals

3.1 Introduction

Colloidal semiconductor nanocrystals are powerful optical materials that combine the photo-stability of conventional crystalline inorganic phosphors with the processing flexibility of molecular dyes or luminophores and the rich electronic structures of semiconductors. As a consequence, they are applied in fields as diverse as photovoltaics, photonics, bio-imaging, nano-sensing, and nano-electronics.[1,2] Doping with transition metal impurity ions allows access to an entirely new portfolio of complementary physical properties in this class of materials.[3] Here we report colloidal semiconductor nanocrystals that show a new photophysical property attractive for ratiometric optical thermometry applications, such as in microfluidics or thermal therapeutics. Pronounced high-temperature dual emission is observed from colloidal semiconductor nanocrystals that possess a unique electronic structure achieved by the combination of doping and bandgap engineering. Photoexcitation of these nanocrystals gives rise to strongly temperature dependent luminescence involving two distinct but interconnected emissive excited states of the same doped nanocrystals. The temperature window over which pronounced dual emission is observed can be tuned by changing the nanocrystal energy gap during growth.

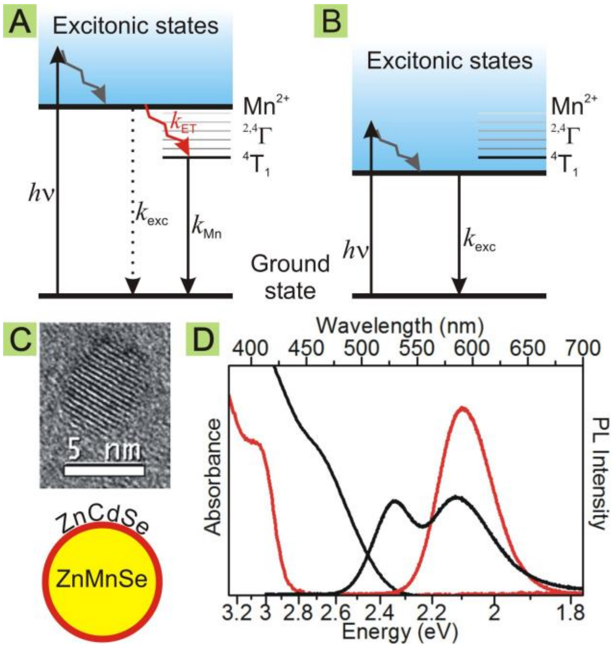

Figure 3.1. Schematic representation of different electronic structures related to photoluminescence in colloidal Mn^{2+}-doped semiconductor nanocrystals. (A) When Mn^{2+} states reside within the semiconductor gap, efficient energy transfer (k_{ET}) quenches excitonic emission and sensitizes Mn^{2+} $^4T_1 \rightarrow {}^6A_1$ luminescence. (B) In narrower-gap semiconductors, all Mn^{2+} excited states are located outside of the gap, and the nanocrystals show excitonic luminescence. (C) TEM image of a colloidal $Zn_{1-x}Mn_xSe$/ZnCdSe core/shell nanocrystal, showing lattice fringes and pseudo-spherical shape, and schematic representation of the same. (D) Room-temperature electronic absorption and photoluminescence spectra of colloidal $Zn_{1-x}Mn_xSe$ and $Zn_{1-x}Mn_xSe$/ZnCdSe nanocrystals. Core diameter = 4.5 nm, x ~ 0.01, shell thickness ~ 0.6 nm.

3.1.A. Two kinds of emission

Photoluminescence (PL) in doped semiconductor nanocrystals typically involves one of two general scenarios for relaxation after photoexcitation. The most extensively studied scenario is typified by $Zn_{1-x}Mn_xSe$ and $Zn_{1-x}Mn_xS$ nanocrystals, which frequently show PL quantum yields exceeding 50%.[4-9] As phosphors, these nanocrystals are characterized by very large energy shifts between absorption and PL maxima arising from rapid nonradiative energy transfer from the excited semiconductor to the Mn^{2+} dopants. The excited dopants then relax radiatively via the $^4T_1 \rightarrow {}^6A_1$ internal *d-d* transition with a slow (τ_{Mn} ~ μsec – msec)[3] The electronic structure responsible for this scenario is generalized in Fig. 3.1A,[10] which is also applicable to numerous other doped semiconductor materials. A qualitatively different scenario is encountered in Mn^{2+}-doped intermediate- or narrow-gap semiconductor nanocrystals such as $Cd_{1-x}Mn_xSe$ and $Cd_{1-x}Mn_xTe$, where the lowest excitonic states occur below all of the Mn^{2+} *d-d* excited states (Fig. 3.1B)[10] and excitonic PL is therefore not quenched by energy transfer to Mn^{2+}. This scenario is conducive to exciton spin polarization and spontaneous magnetization of the Mn^{2+} spins under the exciton's exchange field, as observed in colloidal $Cd_{1-x}Mn_xSe$ nanocrystals.[10,11] Scenarios A and B have both been studied extensively in the corresponding bulk, thin film, and self-assembled quantum dot forms of transition-metal-doped semiconductors.[12,13]

Recently, a new relaxation scenario for photoexcited Mn^{2+}-doped semiconductors was observed: small colloidal $Cd_{1-x}Mn_xSe$ nanocrystals possessing electronic structures like that in scenario A (with Mn^{2+} states within the gap) exhibited excitonic luminescence like in scenario B.[14] This luminescence was characterized by extremely long excitonic PL decay times of up to ~15 μsec at 200 K, orders of magnitude longer than the intrinsic excitonic lifetimes. The slowly decaying Mn^{2+} excited state was shown to act as a population storage reservoir from which an excitonic population could be regenerated thermally, analogous to the classic E-type delayed fluorescence of organic chromophores involving singlet-triplet thermalization.[15] Unfortunately, the small nanocrystal diameters (<~2.5 nm) needed to shift the CdSe excitonic states above the Mn^{2+} $^4T_1$ state approached the lower limit that could be doped, leading to signal "contamination" from undoped nanocrystals that obscured the effect. The PL arising from this unusual scenario constituted a minor fraction of the total PL, and was only clearly observed using gated detection at low temperatures. The need to balance size-dependent doping constraints against the size dependence of the nanocrystal energy gap ultimately limited dual emission in colloidal $Cd_{1-x}Mn_xSe$ nanocrystals to a photophysical novelty.

3.2 Dual emission in $Zn_{1-x}Mn_xSe$/ZnCdSe core/shell nanocrystals

We now demonstrate pronounced dual emission from colloidal Mn^{2+}-doped semiconductor nanocrystals at high temperatures, achieved using $Zn_{1-x}Mn_xSe$/ZnCdSe core/shell nanocrystals instead of $Cd_{1-x}Mn_xSe$ nanocrystals. With these core/shell nanocrystals, the two criteria of nanocrystal doping and energy-gap tuning are no longer interdependent and hence can be optimized individually: the initial preparation of $Zn_{1-x}Mn_xSe$ cores can be optimized for dopant incorporation, and subsequent CdSe shell growth can be optimized for dual emission. Surface termination with additional ZnSe layers was found to improve quantum yields and photostability. With this strategy, dual emission has been achieved as the dominant PL feature of colloidal semiconductor nanocrystals for the first time.

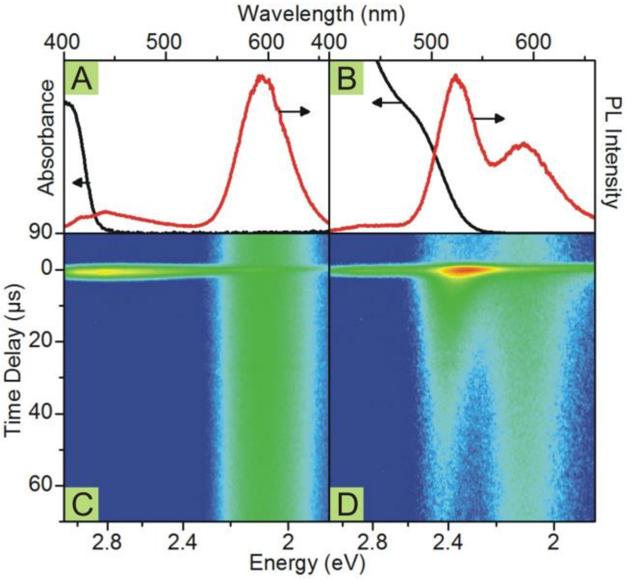

Figure 3.2. Room-temperature absorption and photoluminescence data for (A) $Zn_{1-x}Mn_xSe$ core and (B) $Zn_{1-x}Mn_xSe$/ZnCdSe core/shell nanocrystals. (C, D) Time evolution of the room-temperature photoluminescence for the same samples, plotted on a logarithmic intensity scale. Core diameter = 4.5 nm, $x \sim 0.01$, shell thickness ~ 0.7 nm.

ZnCdSe shell growth around $Zn_{1-x}Mn_xSe$ cores allows the energy gap to be tuned continuously from ~3.0 to ~2.0 eV. Figure 3.1D compares the room-temperature absorption and PL spectra of representative colloidal $Zn_{1-x}Mn_xSe$ and $Zn_{1-x}Mn_xSe$/ZnCdSe nanocrystals. PL from the $Zn_{1-x}Mn_xSe$ nanocrystals is dominated by the Mn^{2+} $^4T_1 \rightarrow {}^6A_1$ band at 2.12 eV, and excitonic PL at ~2.9 eV is almost completely suppressed, as described by Fig. 1A. Shell growth shifts the nanocrystal absorption edge lower by ~0.5 eV. Remarkably, this red shift results in the appearance of a second emission band ~0.25 eV *higher* in energy than the Mn^{2+} band, attributable to excitonic PL.

3.2.A Time resolved dual emission

To probe the relationship between the two PL bands of the core/shell nanocrystals, excited-state dynamics were examined. Figures 3.2A,B show room-temperature PL spectra of core and core/shell nanocrystals measured using pulsed excitation with continuous signal integration, and Fig. 2C,D show the time-resolved PL of the same samples. In the $Zn_{1-x}Mn_xSe$ nanocrystals (Fig. 3.2A,C), the Mn^{2+} $^4T_1$ PL shows a slow decay that exceeds the interval between excitation pulses. From Fig. 2C, $\square_{Mn}$ is on the order of 100 µsec at room temperature. From independent measurements, the excitonic PL decays with a time constant of <20 psec, consistent with fast energy transfer to Mn^{2+} measured in related samples.[17-19] A weak background signal is also observed over the entire window that decays within a few nanoseconds and is attributed to traps. Relative to the core nanocrystals, the excitonic PL decay time is greatly elongated and the Mn^{2+} $^4T_1$ decay time is shortened in the core/shell nanocrystals (Fig. 3.2D). Fig. 3.2D also reveals that the excitonic PL maximum shifts to higher energies with time. Growth of just a thin shell layer thus alters the nanocrystal PL dramatically.

3.3 Modeling dual emission as a decaying ensemble of 3-level systems

In both the $Zn_{1-x}Mn_xSe$ and $Zn_{1-x}Mn_xSe$/ZnCdSe nanocrystals, band-to-band photoexcitation is followed by rapid energy transfer to the lower-energy Mn^{2+} excited state. The dual emission and unusual PL dynamics of the $Zn_{1-x}Mn_xSe$/ZnCdSe nanocrystals are interpreted as arising from thermally assisted population transfer from this $^4T_1$ state *back* to the higher-energy excitonic state. The Mn^{2+} $^4T_1 \rightarrow {}^6A_1$ transition is spin forbidden and has a decay rate constant ~10^3-times smaller than that of the excitonic PL.[14] Consequently, thermal exciton population of only one part in ~10^3 is sufficient to make excitonic and Mn^{2+} PL intensities equivalent. To test this interpretation, the time-dependent PL was modeled using coupled linear rate equations (eq 1) that describe population evolution within the three-level scheme depicted in Fig. 3.3A. $N_{\mathrm{Mn}*}$ and N_{exc} refer to the populations of the Mn^{2+} $^4T_1$ and excitonic states, respectively, and k_{Mn} and k_{exc} are the decay rate constants associated with these excited states in the absence of coupling. k_{ET} and k_{BET} describe exciton-dopant energy transfer rate constants to and from the Mn^{2+}, respectively. When k_{ET} and k_{BET} are fast relative to all others, eq 1 converges to a thermal equilibrium model.[14] All rate constants are effective values, and their dependence on the number and distribution of Mn^{2+} ions, or nonradiative loss pathways, is not explicitly parameterized.

$$\frac{dN_{Mn*}}{dt} = k_{ET}N_{exc} - \left(k_{Mn} + k_{BET}\exp\left(-\frac{\Delta E}{kT} \right) \right) N_{Mn*} \tag{1a}$$

$$\frac{dN_{exc}}{dt} = -\left(k_{exc} + k_{ET} \right) N_{exc} + k_{BET}\exp\left(-\frac{\Delta E}{kT} \right) N_{Mn*} \tag{1b}$$

The remaining parameters in eq 1 are the energy gap between excitonic and Mn^{2+} $^4T_1$ excited states (ΔE, using the Mn^{2+} origin at 2.263 eV) and the thermal free energy (*k*T). The nanocrystal samples studied here possess finite size and shell-thickness distributions that translate into distributions in ΔE and prove invaluable for understanding the effect. To simulate the data in Fig. 2D, the distribution in ΔE was set equal to the experimental intensity distribution of the first excitonic absorption feature.

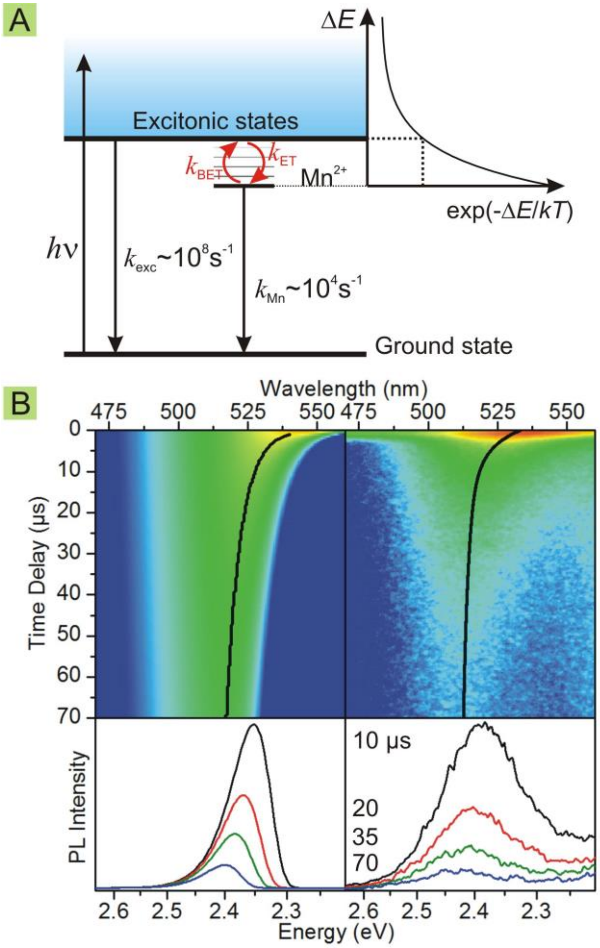

Figure 3.3 (A) Summary of the relevant components of Zn$_{1-x}$Mn$_x$Se/ZnCdSe dual emission as described by eq 1. (B) Simulated (left) and experimental (right, from Fig. 2D) evolution of the excitonic PL, plotted on a logarithmic intensity scale. The black lines are guides to the eye that trace the intensity maxima in time. Simulation parameters: ΔE(center) = 0.32 eV, $k_{Mn} = 10^4$ sec^{-1}, $k_{exc} = 10^8$ sec^{-1}, $k_{ET} = k_{BET} = 5\text{x}10^{10}$ sec^{-1}, T = 298 K, $N_{exc}(0) = 1$. The bottom panels show simulated (left) and experimental (right) PL time slices at 10, 20, 35, and 70 μsec following the excitation pulse, plotted on a linear intensity scale.

k_{Mn} and k_{exc} are readily estimated from experiment, but k_{ET} and k_{BET} are more difficult to determine. A lower bound of k_{ET} ~ 5×10^{10} sec^{-1} (<20 psec) is obtained from streak camera measurements on the $Zn_{1-x}Mn_xSe$ nanocrystals of Fig. 3.2A,C. Rate constants for energy transfer in the opposite direction (k_{BET}) have never been measured, but must also greatly exceed k_{Mn} for dual emission to be observed. To simulate the data in Fig. 3.2D, k_{ET} and k_{BET} were taken to be equal, with the back energy transfer rate attenuated by the appropriate Boltzmann factor.

Figure 3.3B compares the experimental PL time evolution with that calculated from eq. 1 *using no adjustable parameters*. The distribution of decay rates as a function of PL energy that leads to the blue-shifting PL maximum in Fig. 3.2 is clearly captured by the model: nanocrystals that emit further in the blue have larger ΔE, which decreases their back energy transfer rates and thus leads to slower overall population decay. Although more highly parameterized rate equations reproduce the experimental results better, they do not provide a deeper understanding of the underlying physics. Instead, we conclude that the simple three-level model in eq 1 captures the essence of the dual emission in these nanocrystals well.

3.4 Perlustration of potential thermal sensing applications

Pronounced dual emission is rare in colloidal semiconductor nanocrystals, but is well known in molecules. The most structurally similar example is Mn^{2+}/Eu^{3+}-codoped ZnS nanocrystals, which show two independent PL features from the two separate dopants.[20] Photophysically more similar are the molecular examples of exciplex or excimer complexes,[21] and fluorescence/phosphorescence in organics,[15] which both involve population transfer between two excited states. Among all known dual emitters, however, the nanocrystals described here are unique in that the temperatures over which their dual emission occurs can be easily tuned through nanocrystal size or composition control, which tunes ΔE. This dual emission is otherwise largely insensitive to environmental perturbation and is robust against photodegradation. Collectively, such properties make these dual-emitting doped nanocrystals superb probes for ratiometric optical thermometry.[21-23] Colloidal semiconductor nanocrystals are already applied for optical thermometry in many fields,[23-27] but accuracy relies on total intensity measurements that are susceptible to error introduced by optical occlusion, concentration inhomogeneities, excitation power fluctuations, or environment-induced nonradiative relaxation. Ratiometric detection involving two inter-converting excited states of the same nanocrystals circumvents these complications.

To demonstrate, Fig. 3.4A shows PL spectra of $Zn_{1-x}Mn_xSe$/ZnCdSe nanocrystals collected at various temperatures in the physiologically relevant window between 223 and 403 K, and normalized to the total integrated PL intensity at each temperature. At 223 K, the PL spectrum is dominated by the Mn^{2+} $^4T_1 \rightarrow {}^6A_1$ ligand-field PL at 2.1 eV. Above ~310 K, the excitonic PL grows in at ~2.3 eV, and at 403 K the PL is almost exclusively excitonic. Photographs of these nanocrystals at the two extremes of this range are shown in the inset, one yielding green PL and the other yellow. The overall PL intensity decreases by a factor of ~7 over this temperature range, characteristic of thermally activated nonradiative relaxation, but the normalized data show an isostilbic point at 2.2 eV. Invariant nonradiative contributions are required for observation of isostilbic points in PL spectra,[28] and the isostilbic point in Fig. 3.4B thus indicates that nonradiative deactivation in these nanocrystals affects both PL intensities simultaneously and is accounted for by normalization.

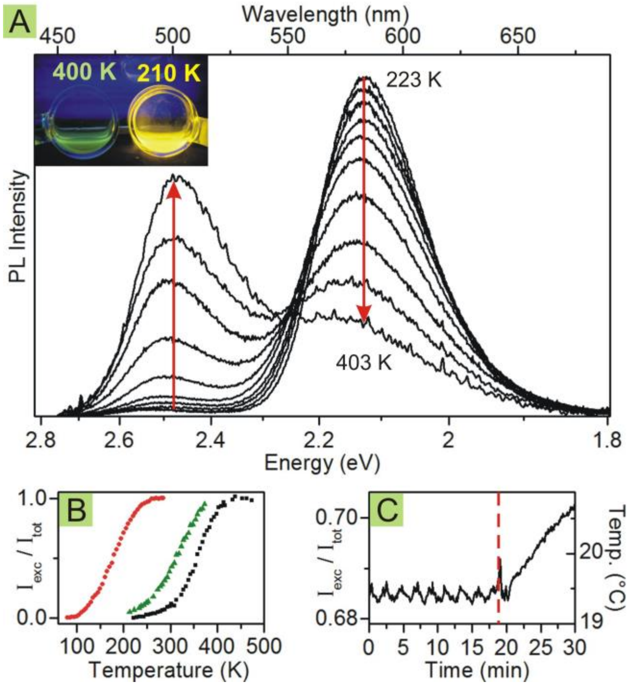

Figure 3.4. (A) Variable-temperature photoluminescence spectra of colloidal $Zn_{1-x}Mn_xSe$/ZnCdSe nanocrystals collected in 20 K intervals and normalized to total integrated intensity, showing intensity transfer between Mn^{2+} and excitonic bands as a function of temperature. Inset: Color photograph of the same nanocrystals at approximately 210 and 400 K. Core diameter = 3.7 nm, x ~ 0.01, shell thickness ~ 0.4 nm. (B) Response curves for three colloidal $Zn_{1-x}Mn_xSe$/ZnCdSe nanocrystal samples, plotting I_{exc}/I_{tot} vs temperature, and showing tunability of the active temperature window. From left to right: (red) core diameter = 4.5 nm, x = 0.01, shell thickness ~ 1.0 nm, (green) core diameter = 4.0 nm, x = 0.01, shell thickness ~ 0.6 nm, (blue) core diameter = 3.7 nm, x = 0.01, shell thickness ~ 0.4 nm. (C) PL response to ±0.2˚C temperature oscillations of a re-circulating chiller with time-averaged sample temperature of 19.5˚C, measured using dispersed halogen lamp excitation and a fiber-coupled hand-held spectrometer. The dashed line marks the point where the chiller was turned off and the sample was allowed to warm toward room temperature. Core diameter = 4.5 nm, x ~ 0.01, shell thickness ~ 0.7 nm.

This result confirms the limit of fast energy transfer in eq 1. Overall, these data demonstrate population transfer from one emissive excited state to the other as a function of temperature. Within the active dual-emission window, each temperature yields a unique PL spectrum characterized by its ratio of excitonic to Mn^{2+} PL intensities.

3.4.A Demonstration of thermal sensing

A calibration curve can be compiled from the data in Fig. 4A by plotting the ratio of integrated excitonic to total PL intensities (I_{exc}/I_{tot}, where $I_{tot} = I_{exc} + I_{Mn}$) vs temperature (Fig. 4B). This curve demonstrates a high thermometric sensitivity with a maximum slope of $9x10^{-3}$ K^{-1}. Furthermore, the temperature window over which dual emission occurs can be tuned simply by changing ΔE during growth. The experimental calibration curves for two additional $Zn_{1-x}Mn_xSe$/ZnCdSe nanocrystal samples with different ΔE values are included in Fig. 4B for comparison. The ability to tune the active dual-emission temperature range by simple changes in growth conditions makes this dual emission attractive as the basis of a new array of optical temperature sensors. For demonstration, Fig. 4C shows a ±0.2˚C oscillation around the set temperature of a closed-cycle chiller detected using the nanocrystals from Fig. 1D, for which a signal-to-noise ratio of ~10 was achieved using simple instrumentation.

3.5 Future outlook

The work with Mn^{2+}-doped nanocrystals reported here is by no means comprehensive. Apart from the Mn^{2+} doping itself, these nanocrystals are essentially indistinguishable from others that have already been applied in biological imaging, microelectronics, thermal therapeutics, or photonics experiments. Using these dual-emitting nanocrystals, such applications can now readily provide *in situ* temperature data. Furthermore, this Mn^{2+}-exciton dual emission is not limited to these core/shell nanocrystals, or even to nanocrystals, but should be generally achievable in other Mn^{2+}-doped semiconductors grown to make $\Delta E < \sim 8\ kT$ (e.g., $Cd_{1-x-y}Zn_xMn_ySe$, $Cd_{1-x}Mn_xS$, $Zn_{1-x}Mn_xTe$, etc.), offering even broader application opportunities.

3.6 Methods

3.6.A Synthesis

All samples were prepared by adaptation of previously published synthetic methods.[1,2] The inorganic precursor used in the synthesis of $Zn_{1-x}Mn_xSe$ nanocrystals, $(Me_4N)_2[Zn_4(SePh)_{10}]$, was prepared following procedures adapted from ref. 3. $Zn_{1-x}Mn_xSe$ nanocrystals were synthesized from this cluster as follows: In a three-neck flask, hexadecylamine (10.8g) and $MnCl_2 \cdot 4H_2O$ (0.01g) were heated at 130°C under vacuum for 90 minutes. The temperature was dropped to 80°C and the solution placed under nitrogen. With a nitrogen over-pressure, the cluster (0.2g) and elemental Se (0.02g) were added to the reaction. The flask was quickly evacuated and refilled with nitrogen three times, and the reaction temperature was allowed to recover to 130°C. After stirring for 90 minutes, the temperature was ramped to 280°C. Nanocrystal growth was complete within 60 to 120 minutes, depending on the desired size. Unreacted precursors were removed by repeated precipitation of the product nanocrystals with ethanol and resuspension in toluene. These conditions were chosen to yield ~1% Mn^{2+} incorporation into the nanocrystals, based on previous experience.

For addition of CdSe to the nanocrystal surfaces, core particles suspended in a small amount of toluene (0.01 mmol, determined by absorption, ref. 4) were added to a three-neck flask containing 4 g of octadecene and 0.5 g of oleylamine. The reaction flask was kept under vacuum at 100°C for 30 minutes. Under a nitrogen atmosphere, the reaction was heated to 200°C, at which point an ODE solution containing 0.05M cadmium oleate/Se and 0.5 g of trioctylphosphine was added to the nanocrystal suspension slowly until the desired energy gap was achieved. These particles were washed by repeated precipitation with ethanol and resuspension in toluene.

Addition of a ZnSe outer shell layer was found to improve PL quantum yields and photostability. Addition of a ZnSe shell to the nanocrystal surfaces was performed by methods adapted from ref. 5: core particles suspended in 2 g of hexadecylamine and 2 g of trioctylphosphineoxide were heated to 200°C. A 0.05 M solution of zinc stearate and TOP/Se in ODE was added over the course of two hours to reach the desired shell thickness.

3.6.B Physical characterization

Absorption spectra of the colloidal nanocrystals were collected using a Cary 500 (Varian) spectrophotometer. TEM images were obtained using an FEI TECNAI F20, 200 kV transmission electron microscope housed at the UW nanotech user facility.

3.6.C Photoluminescence measurements

Room- and low-temperature continuous-wave PL measurements were performed on colloidal suspensions of nanocrystals in toluene, sealed in quartz tubes under nitrogen atmosphere. Low-temperature spectra were obtained using Ar^+ ion laser excitation (457.9 nm, <~10 mW), with frozen suspensions (glassy matrices) of colloidal nanocrystals cooled by helium vapor in a Janis STVP-100 optical cryostat. The PL was dispersed using a 0.5 m single spectrometer (150 grooves/mm grating blazed at 500 nm) and detected with a liquid-nitrogen-cooled charge-coupled. High-temperature continuous-wave photoluminescence data were collected with nanocrystals suspended in octadecene under nitrogen in a three-neck flask. A hand-held UV lamp was used as the excitation source, and a USB2000 Miniature Fiber Optic Spectrometer (Ocean Optics) was used for detection.

The data in Fig. 4C were collected with the sample in a 1cm x 1cm cuvette cooled by a recirculating water chiller to a time-averaged sample temperature of 19.5˚C. The sample was excited using a dispersed halogen lamp, and the PL was detected using a USB2000 Miniature Fiber Optic Spectrometer (Ocean Optics).

All time-resolved photoluminescence measurements were performed on colloidal suspensions in toluene sealed in quartz tubes under nitrogen atmosphere. Samples were excited by the frequency doubled output of a mode-locked Ti:Sapphire oscillator at 3.26 eV, well above their fundamental band-edge absorption energies. The repetition rate of the Ti:Sapphire output was slowed from 76 MHz to 9 kHz using a pulse picker. The pulse duration was on the order of 150 fs, and the instrument response on the order of 50 ps. Data were collected using a streak camera combined with a grating spectrometer.

3.7 References

1 Alivisatos, A.P., Semiconductor Clusters, Nanocrystals, and Quantum Dots. *Science* 271, 933-937 (1996).

2 Talapin, D.V., Lee, J.-S., Kovalenko, M.V., & Shevchenko, E.V., Prospects of Colloidal Nanocrystals for Electronic and Optoelectronic Applications. *Chem. Rev.* 110, 389–458 (2010).

3 Beaulac, R., Ochsenbein, S.T., & Gamelin, D.R., Colloidal Transition-Metal-Doped Quantum Dots in *Semiconductor Quantum Dots,* edited by V. I. Klimov (CRC Press, 2010), pp. 397-453.

4 Bol, A.A. & Meijerink, A., Long-lived Mn2+ Emission in Nanocrystalline ZnS:Mn2+. *Phys. Rev. B* 58, R15997-R16000 (1998).

5 Suyver, J.F., Wuister, S.F., Kelly, J.J., & Meijerink, A., Luminescence of Nanocrystalline ZnSe:Mn2+. *Phys. Chem. Chem. Phys.* 2, 5445-5448 (2000).

6 Norris, D.J., Yao, N., Charnock, F.T., & Kennedy, T.A., High-Quality Manganese-Doped ZnSe Nanocrystals. *Nano Lett.* 1, 3-7 (2001).

7 Yang, H., Holloway, P.H., & Ratna, B.B., Photoluminescent and electroluminescent properties of Mn-doped ZnS nanocrystals (review). *J. Appl. Phys.* 93 (1), 586-592 (2003).

8 Pradhan, N., Goorskey, D., Thessing, J., & Peng, X., An Alternative of CdSe Nanocrystal Emitters: Pure and Tunable Impurity Emissions in ZnSe Nanocrystals. *J. Am. Chem. Soc.* 127, 17586-17587 (2005).

9 Nag, A., Chakraborty, S., & Sarma, D.D., To Dope Mn2+ in a Semiconducting Nanocrystal. *J. Am. Chem. Soc.* 130, 10605–10611 (2008).

10 Beaulac, R. *et al.*, Spin-Polarizable Excitonic Luminescence in Colloidal Mn2+-Doped CdSe Quantum Dots. *Nano Lett.* 8, 1197-1201 (2008).

11 Beaulac, R., Schneider, L., Archer, P.I., Bacher, G., & Gamelin, D.R., Light-Induced Spontaneous Magnetization in Colloidal Doped Quantum Dots. *Science* 325, 973–976 (2009).

12 Furdyna, J.K. & Kossut, J. eds., Diluted Magnetic Semiconductors. (Academic, N.Y., 1988).

13 Bacher, G., Optical Spectroscopy on Epitaxially Grown II–VI Single Quantum Dots (review). *Topics Appl. Phys.* 90, 147-185 (2003).

14 Beaulac, R., Archer, P.I., van Rijssel, J., Meijerink, A., & Gamelin, D.R., Exciton Storage by Mn2+ in Colloidal Mn2+-Doped CdSe Quantum Dots. *Nano Lett.* 8, 2949-2953 (2008).

15 Parker, C.A. & Hatchard, C.G., Triplet-singlet emission in fluid solutions. Phosphorescence of eosin. *Trans. Faraday Soc.* 57, 1894-1904 (1961).

16 Vlaskin, V.A., Beaulac, R., & Gamelin, D.R., Dopant-Carrier Magnetic Exchange Coupling in Inverted Core/Shell Nanocrystals. *Nano Lett.* 9, 4376-4382 (2009).

17 Leinen, D., Excitonic energy transfer to the 3d electrons of Mn2+ in Cd1–xMnxTe. *Phys. Rev. B* 55, 6975-6980 (1997).

18 Seufert, J. *et al.*, Dynamical Spin Response in Semimagnetic Quantum Dots. *Phys. Rev. Lett.* 88, 027402 (2002).

19 Chen, H.-Y., Chen, T.-Y., & Son, D.H., Measurement of Energy Transfer Time in Colloidal Mn-Doped Semiconductor Nanocrystals. *J. Phys. Chem. C* 114, 4418–4423 (2010).

20 Wang, S., Westcott, S., & Chen, W., Nanoparticle Luminescence Thermometry. *J. Phys. Chem. B* 106, 11203-11209 (2002).

21 Uchiyama, S., de Silva, A.P., & Iwai, K., Luminescent Molecular Thermometers. *J. Chem. Ed.* 83, 720-727 (2006).

22 Lou, J., Hatton, T.A., & Laibinis, P.E., Fluorescent Probes for Monitoring Temperature in Organic Solvents. *Anal. Chem.* 69, 1262-1264 (1997).

23 Lee, J. & Kotov, N.A., Thermometer design at the nanoscale. *NanoToday* 2, 48-51 (2007).

24 Han, B. *et al.*, Development of Quantum Dot-Mediated Fluorescence Thermometry for Thermal Therapies. *Annals Biomed. Eng.* 37, 1230–1239 (2009).

25 Walker, G.W. *et al.*, Quantum-dot optical temperature probes. *Appl. Phys. Lett.* 83, 3555-3557 (2003).

26 Lee, C.-G., Yamaguchi, Y., Uehara, M., Nakamura, H., & Maeda, H., Temperature measurement of microfluid using core/shell composite nanocrystals. *J. Chem. Eng. Japan* 41, 1127-1132 (2008).

27 Yu, X.-F. *et al.*, High temperature sensitivity of manganese-assisted excitonic photoluminescence from inverted core/shell ZnSe:Mn/CdSe nanocrystals. *Appl. Phys. Lett.* 96, 123104 (2010).

28 Hamilton, T.D.S. & Naqvi, K.R., Isosbestic points in emission spectra. *Chem. Phys. Lett.* 2, 374-378 (1968).

29 Archer, P.I., Santangelo, S.A., & Gamelin, D.R., Inorganic Cluster Syntheses of TM2+-Doped Quantum Dots (CdSe, CdS, CdSe/CdS): Physical Property Dependence on Dopant Locale. *J. Am. Chem. Soc.* 129, 9808-9818 (2007).

30 Archer, P.I., Santangelo, S.A., & Gamelin, D.R., Direct Observation of sp-d Exchange Interactions in Colloidal Mn2+- and Co2+-doped CdSe Quantum Dots. *Nano Lett.* 7, 1037-1043 (2007).

Chapter 4: ZnS/CdS/ZnS Multishell Heterostrucutres; A New Generation of Dual Emitting Nanocrystals

4.1 Introduction

Multi-shell semiconductor nanocrystals have been synthesized that display intrinsic dual emission with robust photo and thermal stability and attractive thermal sensitivity. In these nanocrystals, dual emission is insensitive to a variety of environments, which include surface functionalization with a variety of ligands, followed by phase transfer into aqueous media, exposure to a wider range of temperatures and storage in air under solvent free conditions. These materials are suitable for further functionalization to handle diverse optical thermometric or thermographic applications in biotechnology and other areas.

4.1.A. The significance of temperature

Temperature plays critical roles in many biological and biotechnological processes ranging from calcium signaling[1] and protein folding[2] to PCR[3] and thermotherapy.[4] The importance of temperature in such processes has fueled interest in the development of *in situ* temperature sensors.[5,6] Measurement of the temperature-dependent photoluminescence (PL) intensities of molecular probes is a popular approach to thermometry in biotechnology.[7] This type of optical measurement is attractive because of its simplicity and excellent spatial and temporal resolution.[8] Numerous luminescent probes based on fluorescent dyes[7-10] and semiconductor nanocrystals[11-13] have been developed for this purpose.

4.1.B. The high functionalization potential of nanocrystals

Colloidal semiconductor nanocrystals (or quantum dots, QDs) are often used as fluorescent labels because of their photostabilities,[14] broad excitation profiles,[15] large absorption cross-sections, and tunable emission energies.[16] The photophysical properties of QDs can be modified in a variety of ways such as by heteroepitaxial shell growth, surface functionalization, or introduction of impurity ions (doping). Nanocrystals containing paramagnetic impurities are attractive as MRI contrast agents.[17] In some cases, these impurities show efficient sensitized PL, making such materials also attractive for optical imaging[18] and sensing.[19]

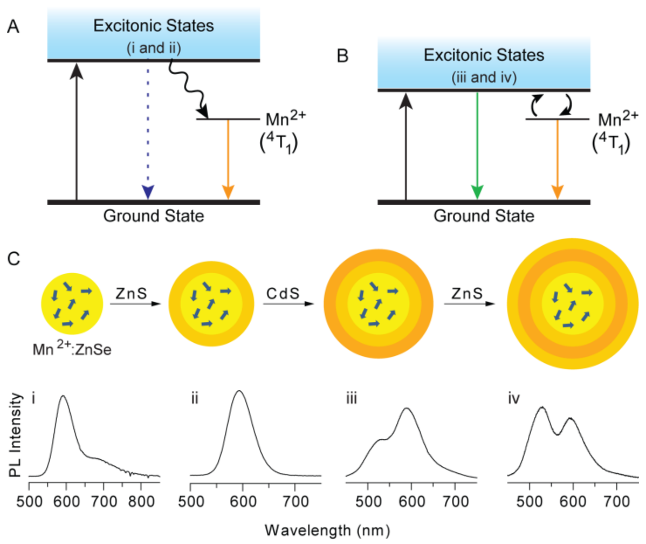

Figure 4.1. Dual-emitting Mn^{2+}-doped semiconductor nanocrystals. (A) Wide-gap Mn^{2+}-doped semiconductor nanocrystals such as $Zn_{1-x}Mn_xSe$ and $Zn_{1-x}Mn_xSe/ZnS$ show efficient sensitized Mn^{2+} luminescence (orange arrow) following semiconductor photoexcitation (black arrow). (B) Narrowing the band gap allows thermal population of excitonic excited states by back energy transfer from $Mn^{2+}(^4T_1)$, yielding excitonic PL (green arrow) in addition to Mn^{2+} PL (orange arrow). (C) (*i*) Core $Zn_{1-x}Mn_xSe$ (d ~ 3 nm) nanocrystals show intense sensitized Mn^{2+} PL at ~590 nm, as well as some trap PL at ~700 nm. (*ii*) Growth of a ~3 monolayer ZnS shell around these cores increases the Mn^{2+} PL QY while eliminating surface trap PL. (*iii*) Growth of a ~1 monolayer CdS shell around the $Zn_{1-x}Mn_xSe/ZnS$ nanocrystals narrows the energy gap and causes the appearance of excitonic PL at ~525 nm, with a drop in PL QY. (*iv*) Growth of a final ~3 monolayer ZnS shell around the $Zn_{1-x}Mn_xSe/ZnS/CdS$ nanocrystals narrows the energy gap slightly, altering the relative intensities of the two PL features. The final nanocrystals have d ~ 6 nm and show intrinsic dual emission at room temperature with PL QYs up to ~40%.

4.2 Dual emission as a powerful ratiometric temperature probe

We recently reported the discovery of a new photophysical process by which nanocrystals show intrinsic dual emission.[20] When Mn^{2+} ions were doped into wide-gap semiconductor nanocrystals such as ZnSe, photoexcitation of the semiconductor resulted in efficient Mn^{2+} sensitized luminescence (Fig. 4.1A). However, when Mn^{2+} ions were doped into semiconductor nanocrystals with energy gaps above but close in energy to the lowest Mn^{2+} *d-d* excited state ($^4T_1$), for example $Zn_{1-x}Mn_xSe$/ZnCdSe core/shell nanocrystals, thermal equilibration of excited-state populations between the $^4T_1$ and excitonic states gave rise to two luminescence bands whose ratio was extremely sensitive to temperature (Fig. 4.1B). The active dual-emission temperature windows could be tuned by adjusting the exciton-Mn^{2+}($^4T_1$) energy gap during nanocrystal synthesis.[20]

4.2.A Inferior properties of dual emitting nanocrystals reported earlier

Although a powerful proof of concept that allowed fundamental aspects of this dual-emission mechanism to be described in detail, the $Zn_{1-x}Mn_xSe$/ZnCdSe nanocrystals examined previously posed some practical limitations. A strong dependence of the nanocrystal energy gap on small numbers of surface Cd^{2+} ions made these structures susceptible to photo- or thermal degradation over long experiment times, because loss of even a few Cd^{2+} ions changed the energy gap governing the thermal equilibrium. Such instabilities were exacerbated in aqueous media. The suitability of these nanocrystals for bio-related applications was also arguably compromised by the exposure of Cd^{2+} at their surfaces. We now report successful preparation of robust dual-emitting nanocrystals that are stable at high temperatures and in water, making them suitable for a broad range of applications including bioimaging.

4.3 The ZnS/CdS/ZnS multishell morphology

4.3.A Synthetic motivations behind this approach

Figure 4.1C summarizes the approach used in the present study to obtain stable, dual-emitting QDs. First, $Zn_{1-x}Mn_xSe$ cores (*i*) were prepared by previously reported methods.[21,22] These core nanocrystals were then coated with shells of ZnS (*ii*), CdS (*iii*), and ZnS again (*iv*), by adaptation of methods described previously.[23,24] Placement of Mn^{2+} in the QD cores ensures rapid exciton-Mn^{2+} energy transfer, and the initial ZnS shell layer significantly improves core PL quantum yields (typically from <~10% to ~40%), likely by passivation of surface trap states. For example, the trap-based PL near 700 nm is diminished upon ZnS shell growth. Growth of a CdS layer around the $Zn_{1-x}Mn_xSe$/ZnS nanocrystals lowers the nanocrystal energy gap and results in appearance of excitonic PL to the blue of the Mn^{2+} PL (Fig. 4.1C.*iii*). Beyond enhancing PL, the first ZnS shell serves as a buffer layer between the ZnSe core and the CdS layer, reducing the sensitivity of the bandgap energy to the addition of Cd^{2+} seen in our previous study by preventing formation of Cd—Se bonds. The ZnS buffer layer also reduces Mn^{2+} migration out of the ZnSe core, a problem encountered upon Cd^{2+} addition to $Zn_{1-x}Mn_xSe$ nanocrystals under some conditions. The final ZnS layer confines the exciton away from the surface, making the QDs more photostable.[25] Outer ZnS shells generally make QDs less prone to oxidation in aqueous solutions as well.[26] Overall, this multi-shell synthetic method allows more precise tuning of the bandgap, and hence of the dual emission, than was achieved previously. The product nanocrystals are brighter and more stable against degradation.

4.3.B Stability at high temperatures

Figure 4.2 illustrates the robustness of the resulting dual-emitting nanocrystals. These nanocrystals exhibit exclusively Mn^{2+} emission (590 nm) at room temperature, with a PL quantum yield of 39%. Upon heating, excitonic PL is observed at 510 nm, concomitant with a decrease of Mn^{2+} PL. At temperatures greater than ~250 °C, the PL intensity has been shifted almost entirely from Mn^{2+} to the excitonic feature (Fig. 4.2A). Figure 2B shows the thermometric response curve measured for these nanocrystals, plotting the ratio of the integrated excitonic emission (I_{exc}) to the total integrated emission (I_{tot}) vs temperature. These data show a high thermometric sensitivity of $\sim 7 \times 10^{-3}$ °C^{-1} over a broad window of ~100 °C. Their stability over extended measurement times at these high temperatures illustrates the thermal robustness of these core/multi-shell dual-emitters.

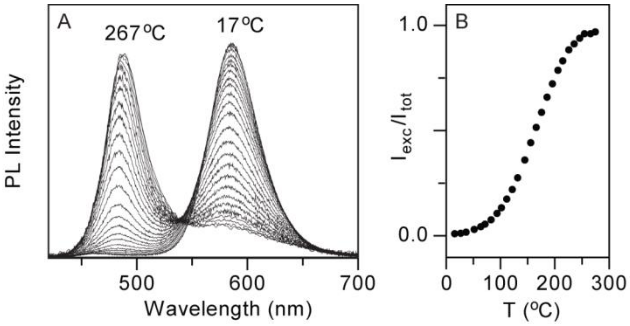

Figure 4.2. Thermal stability. (A) Variable-temperature PL spectra of colloidal $Zn_{1-x}Mn_xSe/ZnS/CdS/ZnS$ nanocrystals (*d* ~ 7 nm, 39% QY at room temperature, capped with TOPO), measured in octadecene under nitrogen. Spectra were normalized to total integrated intensity. (B) Thermometric response curve plotting $I_{\mathrm{exc}}/I_{\mathrm{tot}}$ vs temperature for these nanocrystals. A maximum slope of 7.3×10^{-3} °C^{-1} was obtained.

4.3.C Stability in water

The new multi-shell nanocrystals were found to be compatible with a variety of methods used for transfer to the aqueous phase, Figure 3 demonstrates compatibility with two of these methods. Replacement of TOPO ligands on the nanocrystal surface with citrate[30] molecules, made it possible to use dual emission to monitor temperature of water throughout its full liquid range, from the boiling point to well below its freezing point (Fig. 4.3A). The photograph in the inset of Fig. 3A shows these nanocrystals in toluene and in water. Their PL QY was 10% in water (decreased from 15%) and they showed no degradation over a period of days. Figure 3B plots the thermometric response curve measured for these nanocrystals in water, yielding a maximum sensitivity of $7.2 \times 10^{-3}\ °C^{-1}$. Noteworthy is the continuity in this curve across the liquid-solid phase transition of water, despite severe reduction in optical quality of the aqueous matrix. This result illustrates the powerful advantage of ratiometric optical thermometry.

Nanocrystals were also made hydrophilic by encapsulation with water soluble polymers making it possible for the nanocrystals to retain their surface ligands in the aqueous phase.[14] QDs prepared in this manner are stable for months or longer at room temperature. Figure 4.3C shows the temperature-dependent PL spectra of dual-emitting nanocrystals stabilized in water using *n*-octylamine-modified poly(acrylic) acid. Predominantly Mn^{2+} emission is observed at room temperature, and excitonic emission increases upon sample heating. Figure 3D shows the thermometric response curve measured for these nanocrystals, which display a maximum sensitivity of $8.3 \times 10^{-3}\ °C^{-1}$.

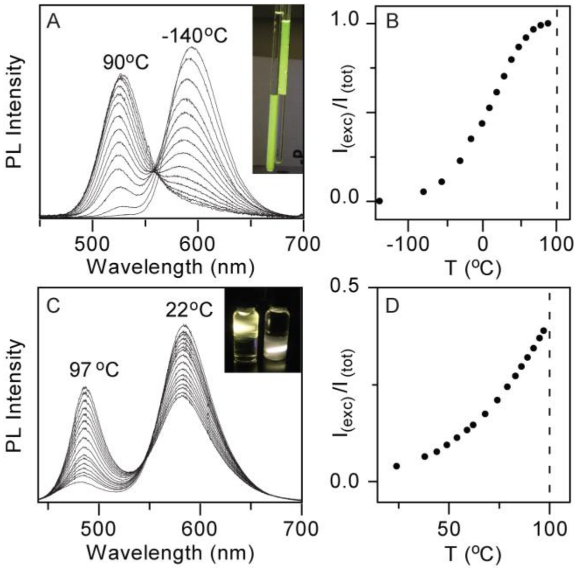

Figure 4.3. Water-soluble dual-emitting nanocrystals. (A) Variable-temperature PL spectra of citrate-capped $Zn_{1-x}Mn_xSe/ZnS/CdS/ZnS$ nanocrystals (*d* ~ 5 nm) in water. Spectra were normalized to the total integrated intensity. Inset: Photograph of the nanocrystals in water (left) and in toluene (right). The QY dropped from 15% to 10% upon phase transfer. (B) Thermometric response curve plotting I_{exc}/I_{tot} vs temperature for these nanocrystals. A maximum slope of 7.2×10^{-3} °C^{-1} was obtained. (C) Variable-temperature PL spectra of $Zn_{1-x}Mn_xSe/ZnS/CdS/ZnS$ nanocrystals encapsulated by *n*-octylamine-modified poly(acrylic) acid, suspended in aqueous solution. The QY dropped from 24% to 19% upon phase transfer. Inset: Photograph of these nanocrystals in toluene (left) and in aqueous solution (right). (D) Thermometric response curve plotting I_{exc}/I_{tot} vs temperature for the polymer-encapsulated nanocrystals. A maximum slope of 8.3×10^{-3} °C^{-1} was obtained.

4.4 Quality factors for ratiometric dual emitting thermometers

In addition to sensitivity, important metrics for evaluation of ratiometric optical thermometers are accuracy and precision with which they can report temperature. Accuracy of these probes is determined extrinsically with the aggregation of data for the calibration curves. Reproducibility of these curves is excellent due to the stability of the nanocrystals, but their accuracy is only as good as the calibrating thermometers used during data collection. With a perfect calibration curve, the precision of the optical thermometers would be determined entirely by the signal-to-noise ratios of the PL spectra, which is determined entirely by the sensitivity of the emission detector and the power of the excitation source. For illustration, the ratio I_{exc}/I_{tot} can be determined from the data in Fig. 4.3C,D with an error of $\pm 1.2\times 10^{-3}$, which translates to a precision of ±0.14 °C over the entire data set. We note that this level of precision exceeds that of the thermometer used in collecting the data for the calibration curve (±0.5 °C). Each spectrum here was collected with 300 ms integration using a hand-held fiber spectrometer and no collection optics. Even higher precision can thus be obtained simply by extending integration times or improving the detection set-up. One of the most adventageous characteristics of ratiometric detection, is that changes in the overall signal amplitude do not result in systematic errors in accuracy, instead precision scales with the overall amplitude, with the assumption that the detector is compatible with the given range of signal amplitudes.

4.5 Summary

Dual emitting Mn^{2+}-doped semiconductor nanocrystals based on the new ZnS/CdS/ZnS multishell motif have been preparad and exibit superior stability at high temperatures in water and in thin films. This constitutes a major expansion in number of potential thermometric applications that dual emitting nanocrystals can accomodate. In particular, stability of these dual emitters in aqueous environments, puts them in consideration for biological or biotechnological applications, such as thermographic imaging of microfluidic PCR devices and thermometric analysis of fundamental biological processes that include apoptosis and function of chaperone proteins.

4.6 Synthesis and physical characterization

$Zn_{1-x}Mn_xSe$ nanocrystals were synthesized from this cluster as follows: In a three-neck flask, hexadecylamine (HDA, 10.8 g)and $MnCl_2{\bullet}4H_2O$ (0.01 g) were heated at 130°C under vacuum for 90 minutes. The temperaturewas dropped to 80°C and the solution placed under nitrogen. Under nitrogen over-pressure, thecluster (0.2 g) and elemental selenium (Se, 0.02 g) were added to the reaction. The flask wasquickly evacuated and refilled with nitrogen three times, and the reaction temperature wasallowed to recover to 130°C. After stirring for 90 minutes, the temperature was ramped to 280°C. Nanocrystal growth was complete within 60 to 120 minutes, depending on the desired core size. Unreacted precursors were removed by repeated precipitation of the product nanocrystals with methanol and resuspension in toluene. These conditions were chosen to yield x~ 0.01, based on previous experience. Shell growth precursors were prepared by adapting previously described methods. For addition of zinc sulfide to the nanocrystal surfaces, core particles, suspended in a small amount of toluene (0.01 mmol in Zn, as determined by absorption) were added to a three-neck flask containing octadecene (ODE, 4 g) and oleylamine (OLA, 0.5 g). The reaction flask was kept under vacuum at 100°C for 30 minutes. Under a nitrogen atmosphere, the reaction was heated to 230°C, at which point an ODE solution containing zinc oleate (0.2 M) was added to the nanocrystal suspension over a period of 3-4 minutes, by syringe. The zinc precursor was allowed to react for 15 minutes prior to the addition of the sulfur precursor. Trioctylphosphine sulfide(TOPS), formed by combining elemental sulfur (1 mmol) and trioctylphosphine (5 ml, 97%,Strem), was added to the core solution over a period of 5 minutes, using a syringe pump. The precursors were allowed to react for 25 minutes prior to the addition of more zinc precursor. The addition of cadmium sulfide to the nanocrystals was performed in an analogous fashion, with a cadmium oleate solution (20 mM in ODE) substituting for the zinc oleate solution. Cationic and anionic precursors were added until the desired energy gap was achieved. The final ZnS shell was added to the nanocrystals in the same fashion as the first ZnS layer. Following synthesis, these nanocrystals were washed by repeated precipitation with ethanol and resuspension in toluene. Water-soluble nanocrystals were first obtained by cap-exchange of the native TOPO ligands with citrate. Nanocrystals were isolated by precipitation from toluene with ethanol. Sodium citrate was added to the pellet and the solids were dispersed in ethanol by sonication over the course of 1 hour. The dots were then isolated from ethanol through centrifugation and the process was repeated 4-5 times with fresh ethanol and sodium citrate added with each repetition.The pellet was then washed with toluene 3 times and then with ethanol once more to remove residual toluene. The particles were suspended in aqueous solution by sonication in water with additional sodium citrate. Nanocrystals encapsulated by *n*-octylamine-modified poly(acrylic) acid (PAA) were prepared by previously reported methods.7 PAA was functionalized with 40% *n*-octylamine groups by amide bond formation with 1-ethyl-3-(3-dimethylaminopropyl) carbodiimide and N-hydroxysuccinimide. Nanocrystals were isolated by repeated precipitation from toluene with ethanol and re-dissolved in a minimal amount of chloroform ($CHCl_3$). A solution of the modified polymer in $CHCl_3$ was added to the nanocrystal solution and left stirring overnight. After removing the $CHCl_3$ by vacuum, sodium bicarbonate buffer (pH ~8.5) was added to suspend thenanocrystals. The solution was then dialyzed at least three times (with 50 kDa MW cutoff spinconcentrators, Millipore) to furnish aqueous nanocrystals.

Absorption spectra of the colloidal nanocrystals were collected using a Cary500 (Varian) spectrophotometer. Room- and low-temperature continuous-wave PL measurements were performed on colloidal suspensions of nanocrystals in toluene. High temperature spectra were taken in ODE under nitrogen atmosphere. Low-temperature spectra were obtained with frozen suspensions of colloidal nanocrystals cooled by liquid nitrogen. An unfocused 405 nm laser (~30 mW) was used as the excitation source, and a USB2000 Miniature Fiber Optic Spectrometer (Ocean Optics) was used for detection. PL quantum yields were measured using an Absolute Photoluminescence Quantum Yield Measurement System C9920-02 (Hamamatsu).

4.7 References

(1) Clausen, T.; Vanhardeveld, C.; Everts, M. E. *Physiol. Rev.* **1991**, *71*, 733.
(2) Murphy, K. P.; Freire, E. *Adv. Protein Chem.* **1992**, *43*, 313.
(3) Zhang, C. S.; Xing, D. *Nucleic Acids Res.* **2007**, *35*, 4223.
(4) Sapareto, S. A.; Dewey, W. C. *Int. J. Radiat. Oncol. Biol. Phys.* **1984**, *10*, 787.
(5) Gosse, C.; Bergaud, C.; Low, P. Molecular Probes for Thermometry in Microfluidic Devices. In *Thermal Nanosystems and Nanomaterials*; Volz, S., Ed.; Topics in Applied Physics; Springer-Verlag Berlin: Berlin, 2009; Vol. 118, p 301.
(6) McCabe, K. M.; Hernandez, M. *Pediatr. Res.* **2010**, *67*, 469.
(7) Uchiyama, S.; de Silva, A. P.; Iwai, K. *J. Chem. Ed.* **2006**, *83*, 720.
(8) Ross, D.; Gaitan, M.; Locascio, L. E. *Anal. Chem.* **2001**, *73*, 4117.
(9) Lou, J. F.; Hatton, T. A.; Laibinis, P. E. *Anal. Chem.* **1997**, *69*, 1262.
(10) Schrum, K. F.; Williams, A. M.; Haerther, S. A.; Benamotz, D. *Anal. Chem.* **1994**, *66*, 2788.
(11) Wang, S. P.; Westcott, S.; Chen, W. *J. Phys. Chem. B* **2002**, *106*, 11203.
(12) Walker, G.; Sundar, V.; Rudzinski, C.; Wun, A.; Bawendi, M.; Nocera, D. *App. Phys. Lett.* **2003**, *83*, 3555.
(13) Han, B.; Hanson, W. L.; Bensalah, K.; Tuncel, A.; Stern, J. M.; Cadeddu, J. A. *Ann. Biomed. Eng.* **2009**, *37*, 1230.
(14) Wu, X. Y.; Liu, H. J.; Liu, J. Q.; Haley, K. N.; Treadway, J. A.; Larson, J. P.; Ge, N. F.; Peale, F.; Bruchez, M. P. *Nat. Biotechnol.* **2003**, *21*, 41.
(15) Murray, C. B.; Norris, D. J.; Bawendi, M. G. *J. Am. Chem. Soc.* **1993**, *115*, 8706.
(16) Chan, W. C. W.; Maxwell, D. J.; Gao, X. H.; Bailey, R. E.; Han, M. Y.; Nie, S. M. *Curr. Opin. Biotechnol.* **2002**, *13*, 40.
(17) Mornet, S.; Vasseur, S.; Grasset, F.; Duguet, E. *J. Mater. Chem.* **2004**, *14*, 2161.
(18) Louie, A. *Chem. Rev.* **2010**, *110*, 3146.
(19) Thakar, R.; Chen, Y. C.; Snee, P. T. *Nano Lett.* **2007**, *7*, 3429.
(20) Vlaskin, V. A.; Janssen, N.; van Rijssel, J.; Beaulac, R.; Gamelin, D. R. *Nano Lett.* **2010**, *10*, 3670.
(21) Archer, P. I.; Santangelo, S. A.; Gamelin, D. R. *J. Am. Chem. Soc.* **2007**, *129*, 9808.
(22) Archer, P. I.; Santangelo, S. A.; Gamelin, D. R. *Nano Lett.* **2007**, *7*, 1037.

(23) Li, J. J.; Wang, Y. A.; Guo, W.; Keay, J. C.; Mishima, T. D.; Johnson, M. B.; Peng, X. *J. Am. Chem. Soc.* **2003**, *125*, 12567.

(24) Chen, H.-S.; Lo, B.; Hwang, J.-Y.; Chang, G.-Y.; Chen, C.-M.; Tasi, S.-J.; Wang, S.-J. J. *J. Phys. Chem. B* **2004**, *108*, 17119.

(25) Reiss, P.; Protiere, M.; Li, L. *Small* **2009**, *5*, 154.

(26) Medintz, I. L.; Uyeda, H. T.; Goldman, E. R.; Mattoussi, H. *Nat. Mater.* **2005**, *4*, 435.

(27) Nose, K.; Fujita, H.; Omata, T.; Otsuka-Yao-Matsuo, S.; Nakamura, H.; Maeda, H. *J. Lumin.* **2007**, *126*, 21.

(28) Pilla, V.; Alves, L. P.; Munin, E.; Pacheco, M. T. T. *Opt. Commun.* **2007**, *280*, 225.

(29) Munro, A. M.; Jen-La Plante, I.; Ng, M. S.; Ginger, D. S. *J. Phys. Chem. C* **2007**, *111*, 6220.

(30) Rogach, A. L.; Nagesha, D.; Ostrander, J. W.; Giersig, M.; Kotov, N. A. *Chem. Mater.* **2000**, *12*, 2676.

Chapter 5: Doping Nanocrystals by Diffusion

(swimming in an excess anion sea with my fat friends under a gentle sprinkle of cations that remain faithful… I'm staying)

5.1 Background

The physical properties of inorganic crystals can be changed dramatically by the introduction of impurities. The development of synthetic methods for growing high-quality doped inorganic crystals has consequently been a perennial frontier of materials science, laying the foundation for such technological milestones as the Ruby laser and silicon microelectronics. The past two decades have seen the emergence of another frontier in crystal growth that exploits the ability to isolate kinetically trapped semiconductor nanocrystals, often with anisotropic shapes, before they evolve into their macroscopic thermodynamic end products. Colloidal CdSe nanocrystals have played a central role in the advancement of this field,[1-4] serving as a model system for the development of optimized syntheses controlling structural quality, nanocrystal uniformity, shape anisotropies, and ultimately translating these features into powerful physical properties.[5,6] For almost as long, however, it has also been recognized that traditional methods for doping macroscopic crystals are generally incompatible with the syntheses of such kinetically trapped nanostructures.[7-12] For example, a traditional method for preparation of high-quality crystals of II-VI semiconductor solid solutions is the Bridgeman technique, in which the crystal growth front is in equilibrium with the melt reservoir, and hence the crystal is formed at its thermodynamically favored composition. Heating colloidal nanocrystals to drive such equilibria usually results in severe Ostwald ripening and loss of the desired properties obtained from size or shape control. Consequently, efforts to dope nanocrystals have largely focused on impurity incorporation during growth, where doping is governed kinetically. Under these conditions, dopants must compete with host cations for available surface binding sites, and nanocrystal surfaces must compete against surfactant ligands for impurity binding. Figure 1A adapts the Sugimoto model of nutrient concentration gradients, during crystal growth, in the context of diffusion doping, showing a small nanocrystal growing in the presence of both lattice nutrients and impurity ions. For $Cd_{1-x}Mn_xSe$ growth under normal hot-injection conditions, Cd^{2+} deposition is diffusion limited, resulting in depletion at the surfaces. Because of unfavorable hard/soft acid/base conditions, however, Mn^{2+} depletion at the same surface is negligible. The surface competition reactions are biased against impurities that have mismatches in charge, size, geometry, ionicity, or other physical attributes, and hence typically disfavor doping. For example, whereas bulk $Cd_{1-x}Mn_xSe$ crystals have been grown from the melt with x as high as 0.5,[13] synthesis of comparable colloidal $Cd_{1-x}Mn_xSe$ nanocrystals by state-of-the-art hot-injection methods has proven tremendously challenging.[10] The synthesis of colloidal $Cd_{1-x}Mn_xSe$ nanocrystals has therefore long served as a testing ground for the development of innovative nanocrystal doping chemistries intended to overcome these general challenges. In specific cases, fast-diffusing ions can be introduced into colloidal nanocrystals at temperatures that are too low for substantial Ostwald ripening, allowing thermodynamic nanocrystal composition control. [14-23] The most thoroughly investigated of such chemistries is so-called "cation exchange".[14-20] A defining feature of cation-exchange reactions that makes them extremely powerful is that the anion sublattice remains invariant, allowing retention of crystallite shape anisotropies and phases despite dramatic changes in crystal composition. Under thermodynamic control, cation exchange is governed by the differences between crystal and solution chemical potentials (μ^{NC} *vs* $\mu^{solution}$) of the impurity and host ions. Unfortunately, such reactions are limited to a relatively small set of cation combinations for which diffusion is rapid. Raising temperatures to drive diffusion of less reactive cations such as Mn^{2+} can cause severe Ostwald ripening and sacrifice nanostructuring.[24] Mn^{2+} incorporation into magic-size ZnTe nanoclusters via cation exchange has been successful,[25] as has cation exchange in even smaller clusters,[26,27] but successful synthesis of $Cd_{1-x}Mn_xSe$ or related nanocrystals by cation exchange has not been reported. For example, deliberate attempts to introduce Mn^{2+} into pre-formed colloidal ZnSe nanocrystals at elevated temperatures were either unsuccessful[28] or accompanied by severe ripening and collapse of shape anisotropy.[24] Indeed, it has been a long-standing tenet of nanocrystal doping that Mn^{2+} diffusion in II-VI nanocrystals is negligible at normal colloid growth or handling temperatures, and that equilibrium doping concentrations are therefore inaccessible.[8,9,29,30] Researchers wishing to access the unique luminescent, magnetic, magneto-optical, or magneto-electronic properties of Mn^{2+}-doped II-VI semiconductor nanocrystals, or of other doped nanocrystals that do not involve fast diffusers, are thus to date primarily restricted to samples synthesized under kinetic control.

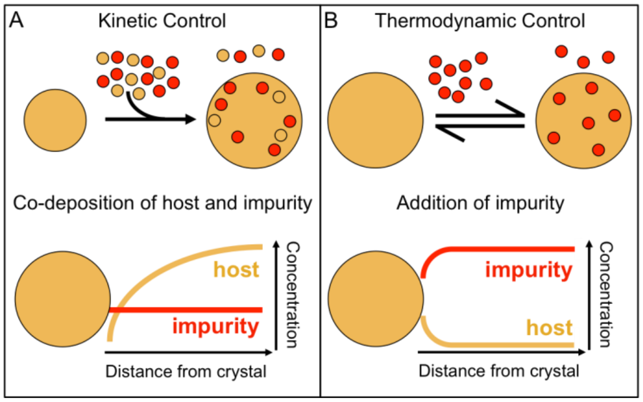

Figure. 5.1. Incorporation of impurities into nanocrystals under kinetic (A) or thermodynamic (B) control. Under kinetic control, impurities compete with host nutrients for surface binding sites and are internalized via subsequent crystal lattice overgrowth. Under thermodynamic control, impurities enter the nanocrystal lattice under quasi-equilibrium conditions, driven by entropy, and are internalized via diffusion of the crystal ions.

5.1.A Statement of problem: Rediagonalize equilibrium perpendicular to size and shape of the nanocrystals and turn up the heat

To achieve thermodynamically controlled Mn^{2+} doping of semiconductor nanocrystals, two seemingly incommensurate criteria must be met: the nanocrystals must be allowed to progress toward their equilibrium solid-solution composition without approaching their equilibrium morphology. In other words, the lattice must be sufficiently fluid to allow mixing rather than just heterostructure formation, but at the same time, inter-particle (and in anisotropic crystals, also intra-particle) mass transfer must be avoided. Figure 5.1B illustrates the desired thermodynamically controlled doping process, in this example via impurity addition to a pre-formed spherical nanocrystal. To be successful, this process must tune the solution and lattice chemical potentials of both host and impurity ions such that impurity addition is thermodynamically favorable and ripening is minimized. Simultaneously, there must be sufficient thermal energy for impurity diffusion from the surface into the internal volume of the nanocrystal.

5.1.B Summary

Here we report development of a successful synthesis of high-quality colloidal $Cd_{1-x}Mn_xSe$ nanocrystals performed under thermodynamic rather than kinetic control, based on addressing the above challenges in a systematic way. Beginning with colloidal CdSe quantum dots prepared by state-of-the-art hot-injection methods, we demonstrate thermally activated diffusion of Mn^{2+} into the nanocrystal internal volumes. In contrast with cation-exchange processes described previously, we show that this diffusion doping involves stoichiometric cation + anion addition without the loss of host cations and hence increases the nanocrystal volume in proportion to x. In common with cation-exchange reactions, we show that this diffusion doping allows retention of the original nanocrystal size distributions, crystallographic phases, and even shape anisotropies. The resulting nanocrystals show Mn^{2+} concentrations exceeding any reported previously for colloidal $Cd_{1-x}Mn_xSe$ nanocrystals, while simultaneously showing size and shape uniformity unparalleled in doped CdSe nanocrystals to date. We then illustrate the generality of this method by describing doping of CdSe nanocrystals with other cationic impurities, sequential tandem doping of two impurities into the same CdSe nanocrystals, and preliminary results for diffusion doping of CdTe, CdS, and ZnSe nanocrystals. The materials reported here represent a new benchmark for high-quality doped CdSe nanocrystals in particular, and in general illustrate the value of diffusion doping for preparing complex doped nanostructures under thermodynamic control.

5.2 Manufacturing the synthesis

5.2.A Conditions

The set of conditions developed by Norberg, N. S. et. al for the synthesis of Co^{2+}:ZnSe nanocrystals identified the ideal conditions for doping nanocrystals at temperatures, as it was later shown, high enough to allow rapid exchange of cations between the nanocrystals and solution. The successful generalization of this synthesis to Mn^{2+}:CdSe was described in chapter 1.7, however it had the major limitation of having nucleation and growth in the same solution. This meant that various parameters such as Mn^{2+} concentration could not be varied, if they had a major deleterius effect on one of the stages. Once Barrows C.J. collected enough compelling evidence demostrating decoupled Mn^{2+} doping and CdSe growth, he left no reason to continue to try to optimize conditions for doping, growth and nucleation in the same solution. Kinetic trapping was no longer the only way to dope. Decoupling of nucleation/growth from doping/growth was achieved by applying the seeded growth techniques, described in chapter

4.3.B. pioneered by the Dimitri Talapin and Liberto Manna, with ligands taken from what is still essentially Nick Norberg's Co^{2+}:ZnSe synthesis discussed in chapter 1.5.C.

5.2.B The best analytical tool for Mn^{2+} doped semiconductor nanocrystals; room temperature MCD

As detailed previously,[10,11,37,38] doping CdSe nanocrystals with Mn^{2+} results in MCD intensity inversion and enhancement at the CdSe absorption edge. These changes arise from the introduction of strong *sp-d* exchange contributions to excitonic Zeeman splittings upon Mn^{2+} doping, as described by eq 1.[11,39] The first term in eq 1 describes the intrinsic contribution to the excitonic Zeeman splitting energies ($\Delta E_{\mathrm{Zeeman}}$) of CdSe nanocrystals. This contribution is small, temperature independent, and linearly dependent on magnetic field (B, where μ_{B} is the Bohr magneton). Experimental measurements have yielded $g_{\mathrm{int}} \sim +1.0$ for undoped pseudo-spherical CdSe nanocrystals.[37,40] For the purposes of this study we consider negative g_{Exc}, values to be conclusive evidence os substantial Mn^{2+} doping. The second term in eq 1 describes the

$$\Delta E_{\mathrm{Zeeman}} = g_{\mathrm{int}} \mu_{\mathrm{B}} B + x_{\mathrm{eff}} \left\langle S_z \right\rangle N_0 \left(\alpha - \beta \right) \qquad (1)$$

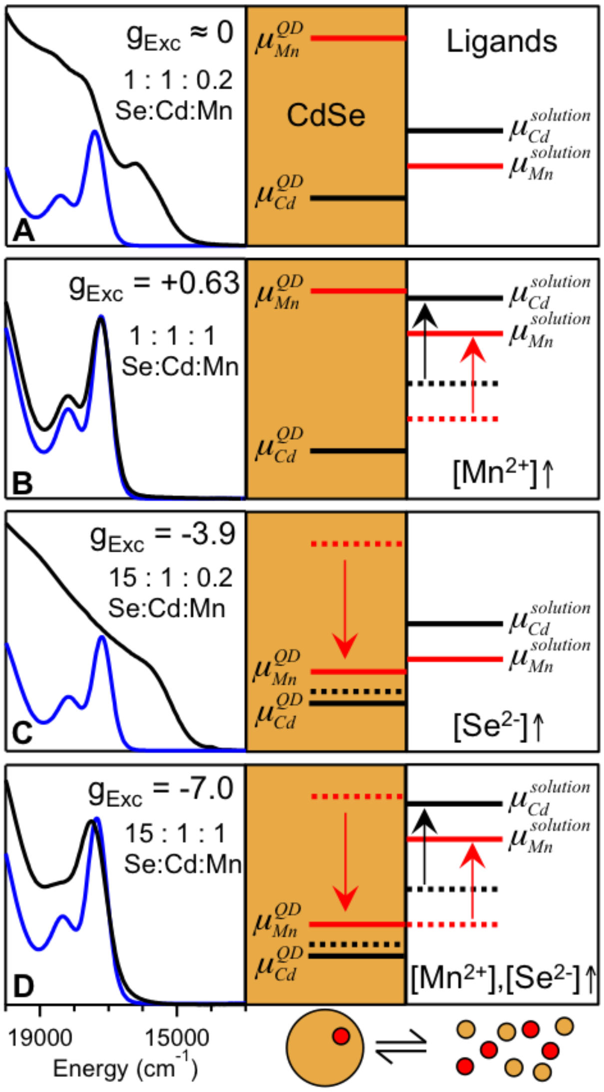

Figure. 5.2. (Left) Room-temperature electronic absorption spectra of the first excitonic feature of *zb*-CdSe nanocrystals before (blue) and after (black) 30 min at 300 °C under the conditions described in the text and with the ion ratios indicated. Undoped *zb*-CdSe nanocrystals are injected into reaction solutions with (A) Mn^{2+} in a 0.2:1 ratio to the Cd^{2+} contained in the nanocrystals, (B) Mn^{2+} in solution in a 1:1 ratio with the Cd^{2+} contained in the nanocrystals, (C) Se^{2-} and Mn^{2+} in a 15:1:0.2 ratio to the Cd^{2+} contained in the nanocrystals, and (D) Se^{2-} and Mn^{2+} in a 15:1:1 ratio to the Cd^{2+} contained in the nanocrystals. The excitonic *g* values of the resulting nanocrystals, determined from room-temperature MCD spectroscopy, are given in each panel and indicate negligible-to-weak Mn^{2+}-exciton exchange coupling in panels A and B, and strong exchange coupling in panels C and D. (Right) Relative free energies of the Mn^{2+} and Cd^{2+} cation chemical potentials on either side of the nanocrystal/solution interface, for identical reaction conditions with the exception of relative ionic ratios.

dopant-exciton *sp-d* exchange coupling contribution to ΔE_{Zeeman}, where $\langle S_z \rangle$ is the spin expectation value of the dopant at the experimental temperature and magnetic field (as described by the Brillouin function for magnetic ions with spin-only ground states, such as Mn^{2+}), $N_0(\alpha - \beta)$ is the mean-field *sp-d* exchange energy, and x_{eff} represents the effective amount of paramagnetic Mn^{2+} exchange coupled with the exciton. x_{eff} is generally smaller than x because of Mn^{2+}-Mn^{2+} pair formation,[13,41] reaching its maximum of ~3.3% when x is ~8.2%. In nanocrystals, x_{eff} is typically also smaller than x because of undoped cores.[42,43] For the cases studied here, the *sp-d* exchange term has the opposite sign of the intrinsic term, where $<S_z>$ is strongly temperature dependent, invesly proportional to temperature for simple paramagnets like Mn^{2+}. In the limit of small B, $\langle S_z \rangle$ is also linearly proportional to B (the Curie limit). In this regime, the proportionality constant $g_{\text{Exc}} = \Delta E_{\text{Zeeman}}/\mu_B B$ provides a measure of these two competing contributions to ΔE_{Zeeman}. Room-temperature MCD spectroscopy of the nanocrystals in Fig. 2A shows little or no intensity at the first exciton, $g_{\text{Exc}} \approx 0$, and hence little or no success in doping.

5.2.C Systematic variation of chemical potentials

Figure 2A(right) illustrates why doping does take place under these conditions, in terms of Cd^{2+} and Mn^{2+} chemical potentials. Under these experimental conditions, the soft Cd^{2+} Lewis acid preferentially binds to the soft Se^{2-} rather than to the hard Lewis bases present in solution as surfactants (stearate and hexadecylamine). Conversely, Mn^{2+} prefers these harder ligands. The resulting imbalance in chemical potentials favors Mn^{2+} solvation and is responsible for absense of exchange between Cd^{2+} and Mn^{2+} under these conditions. Moreover, the relatively small imbalance between μ_{Cd}^{NC} and $\mu_{Cd}^{solution}$ allows large Cd^{2+} diffusion lengths in solution and hence

Ostwald ripening.

To encourage doping, the Mn^{2+} concentration in solution was greatly increased compared to conditions of Fig. 5.2A so that it now equaled the total Cd^{2+} content of the seed CdSe nanocrystals. These levels more closely resemble conditions in cation-exchange reactions than in kinetic doping reactions. Figure 5.2B(left) shows absorption spectra collected before and after heating CdSe nanocrystals in the presence of such an excess of Mn^{2+}. A positive value of g_{Exc} = +0.63 is observed by MCD spectroscopy following heating at 300 °C for 30 min, again indicating little or no successful doping. Although Mn^{2+} is not incorporated, the nanocrystals remarkably preserve their average size and narrow size distribution despite prolonged heating. These observations can be understood by considering the effects of increased Mn^{2+} concentration illustrated in Fig. 5.2B(right). When Mn^{2+} is added as $Mn(OAc)_2$, its ligands can be exchanged by pumping off acetic acid, such that Mn^{2+} in the reaction solution is coordinated by the surfactant ligands, oleate and hexadecylamine. Such a large increase in Mn^{2+} concentration thus increases the chemical potentials of both Mn^{2+} and Cd^{2+} ions in solution because the free ligand concentration decreases, analogous to the common ion effect This assumption is supported by control experiments, where increased HDA concentration promotes Ostwald ripening. The added driving force for Cd^{2+} binding to the CdSe surfaces offsets any increased driving force for Mn^{2+} incorporation into the crystals, and consequently doping does not proceed. If this was the last experiment, Gustavo M. Dalpian could claim victory. A striking observation is made however, the increased chemical potential of Cd^{2+} in solution attenuates CdSe diffusion and thereby suppresses Ostwald ripening. The ability to turn off Ostwald Ripening at temperatures high enough to drive alloying inside the nanocrystals, is a major breakthrough, however to this day it appears to be specific to Mn^{2+} and CdSe. A generalization of this across all materials would be a revolution in nanoscale synthesis.

The dream of doping Mn^{2+} into CdSe nanocrystals exclusively through chemical potential manipulation, is the same thing as dreaming that conditions for doping via cation exchange exist. This is where the 2006 calculation by Gustavo M. Dalpian et.al. is applicable and proves impossibility of doping nanocrystals, unless they get so large that accidents happen. The only theoretical way to solve this problem would be to find something that is softer than Se^{2-} , yet would be able to solubalize Mn^{2+}.

The straight forward solution to an impossible problem is to remove it. Figure 5.2C(left) shows absorption spectra collected before and after heating when excess Se^{2-} (instead of excess Mn^{2+}) is added at a 15:1 ratio to total Cd^{2+}, with other conditions the same as in Fig. 1A. Upon heating, the CdSe absorption edge redshifts by ~1500 cm^{-1} and broadens considerably, indicating extensive Ostwald ripening, however room-temperature MCD of the resulting nanocrystals shows a sign inversion of the excitonic feature, with $g_{\mathrm{Exc}} = -3.9$, indicating dominance of Mn^{2+}-exciton *sp*-*d* exchange and hence successful Mn^{2+} incorporation. If Mn^{2+} and Cd^{2+} do not compete for the same Se^{2-} then their relative chemical potentials become irrelevant and doping can be thermodynamically driven by the relative positions of chemical exclusively Mn^{2+} chemical potentials. Figure 5.2C(right) shows one such possibility, where it achieved by decreasing the chemical potential of Mn^{2+} inside the lattice, using excess Se^{2-}.

The other possible way to control the relative positions of Mn^{2+} chemical potentials, is through mass action, which also conveniently turns off Ostwald ripening, this is shown in figure 5.2D. Absorption spectra collected before and after heating CdSe seed nanocrystals at 300 °C for 30 min in the presence of excess Se^{2-} and Mn^{2+}, confirms suppression of Oswald ripening with the excitonic feature relatively unchanged throughout the process. Room-temperature MCD yields g_{Exc} = -7.0 for these nanocrystals. A truly remarkable result given that the magnitude of this Zeeman splitting made this the most heavility doped ensemble of Mn^{2+}:CdSe nanocrystals ever made at the time. Furthermore the width of the excitonic feature is only slightly larger than the expected homogeneous bandwidth, making this ensemble of 10^{17}, spherical entities composed of 700 CdSe units and 50 Mn^{2+} cations each on average, a complete domination of enthalpy over entropy.

5.3 Properties of nanocrystals produced by diffusion doping

5.3.A Temporal evolution of the nanocrystal ensemble

To further explore the chemistry shown in Fig. 2D, a reaction was performed under these conditions with aliquots periodically withdrawn from the solution. Figure 5.3A shows the evolution of the CdSe absorption spectrum with reaction time at 300 °C. The first excitonic feature broadens and shifts to higher energy as the reaction proceeds. Figure 5.3B shows that this trend is accompanied by an inversion and progressive increase in MCD intensity at the CdSe absorption edge. g_{Exc} becomes dominated by *sp-d* exchange within the first 2 minutes.

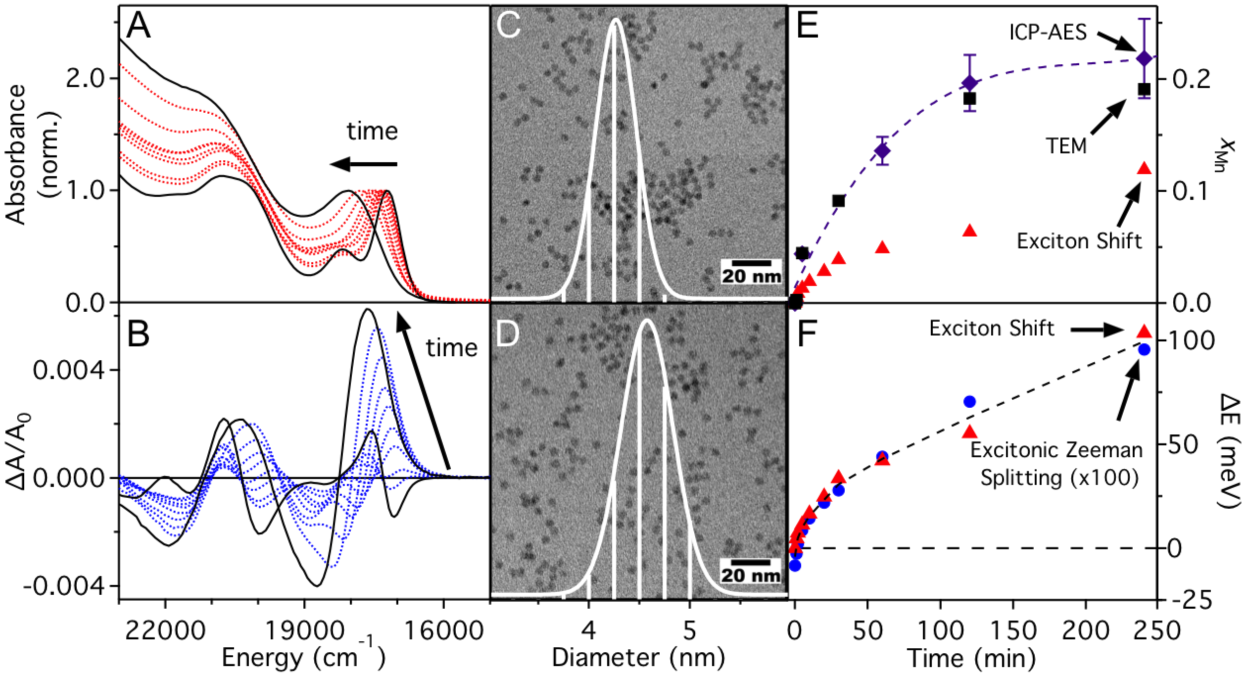

Figure 5.3. (A) Room-temperature electronic absorption spectra of reaction aliquots taken at different times during *w*-CdSe nanocrystal diffusion doping at 300 °C, normalized at the first excitonic maximum. (B) Corresponding MCD spectra showing a sign inversion and signal growth with increased reaction time, indicative of growing *sp*-*d* exchange coupling strengths. (C) TEM image and corresponding diameter histogram from analysis of undoped CdSe ($d = 4.37 \pm 0.18$ nm) precursor nanocrystals. (D) TEM image and corresponding diameter histogram from analysis of $Cd_{1-x}Mn_xSe$ nanocrystals after 240 min of diffusion doping at 300 °C ($d = 4.69 \pm 0.24$ nm). (E) Mn^{2+} cation mole fraction (x_{Mn}) determined by ICP-AES (purple diamonds, with error bars from three measurements of each aliquot), analysis of volumes obtained from TEM (black squares), and analysis of the excitonic absorption energy shifts (red triangles). The dashed line is a guide to the eye. In order of increasing reaction time, the standard deviations on the average nanocrystal diameters from TEM are: 4.1 (seed), 3.4, 4.1, 3.8, 3.6, and 5.1%. (F) Excitonic absorption energy shifts (red triangles, from analysis of panel (A) data) and excitonic Zeeman splittings (blue circles, from analysis of panel (B) data, multiplied 100x) plotted vs diffusion doping time. The dashed line is a guide to the eye.

Figure 5.3C shows a TEM image of the seed CdSe nanocrystals used in the experiments of Fig. 5.3A,B. These nanocrystals have diameter 4.37 ± 0.18 nm ($\sigma = 4.1\%$). Figure 5.3D shows a TEM image of the same nanocrystals after 4 hrs of heating at 300 °C in the presence of excess Mn^{2+} and Se^{2-}. The average diameter increases to 4.69 ± 0.24 nm ($\sigma = 5.1\%$). We attribute this growth entirely to addition of Mn-Se units to the seed CdSe nanocrystal. From this volume increase, a value of x_{Mn} ~ 0.19 can be inferred in the maximally doped nanocrystals, corresponding to ~195 Mn^{2+}/nanocrystal. Figure 5.3E summarizes the TEM results, plotting the data as x_{Mn} vs diffusion doping time under the assumption that growth derives solely from addition of Mn-Se units. These data show an initial increase and subsequent plateau at x_{Mn} ~ 0.19 over the course of 4 hrs. This curvature is indicative of an equilibrium process. For comparison, x_{Mn} was also determined analytically for each aliquot using ICP-AES following careful washing to remove adventitious Mn^{2+}. Figure 5.3E plots these analytical concentrations on the same axes as the concentrations estimated from TEM. The analytical x_{Mn} data agree very well with the values deduced from the TEM data, again increasing over the first two hours before plateauing at x_{Mn} ~ 0.22. The agreement between these two data sets confirms that this synthesis introduces Mn^{2+} into seed CdSe nanocrystals by addition of Mn-Se units. Beyond this unprecedentedly large Mn^{2+} concentration in colloidal CdSe nanocrystals, the remarkable feature of these data is that the nanocrystal size distribution remains essentially unchanged following such prolonged heating.

5.2.B Evidence of fast deposition followed by slower alloying

The TEM results show that the exciton broadening seen in Figs. 5.2D and 5.3A does not come from a loss of the size uniformity. Instead, this broadening reflects perturbation of the transition energy due to Mn^{2+} addition. Figure 5.3F plots the energy of the first excitonic maximum (E_g) vs Mn^{2+} diffusion doping time for the same aliquots. E_g *increases* with Mn^{2+} addition, despite the increasing nanocrystal volumes. This increase starts immediately and proceeds for the first 2 hrs before leveling somewhat, but a terminal plateau is not reached within 4 hrs. These data demonstrate that Mn-Se does not simply deposit onto the CdSe NC surfaces to form CdSe/MnSe core/shell structures. Like CdSe/ZnSe core/shell nanocrystals, such structures would show exciton relaxation into the shell layer and hence a small decrease in E_g. Instead, the data confirm $Cd_{1-x}Mn_xSe$ solid-solution formation. To understand these data, we recall that E_g in bulk CdSe displays a well-defined dependence on x_{Mn}, shifting to higher energy linearly with a slope of ~+11.4 meV/x_{Mn}(%) (or +92 cm^{-1}/x_{Mn}(%)).[39] This shift is largely attributable to the fact that the empty Mn^{2+}(4*s*) orbitals are in poor energetic alignment with the Cd^{2+}(5*s*) orbitals, [44,45] and consequently Mn^{2+} inclusion into the lattice disrupts the CdSe conduction band. The blue shift in E_g with increasing nanocrystal volume shown in Fig. 3 thus results from the dependence of E_g on x_{Mn}. An estimate of x_{Mn} from E_g was attempted but is made difficult by the fact that these nanocrystals are quantum confined, and addition of Mn-Se units simultaneously relaxes the exciton spatial confinement. If we assume that E_g simply scales linearly with x_{Mn} as in bulk, but now starts from E_g of the undoped CdSe NCs and finishes at the bulk bandgap energy of the hypothetical wurtzite MnSe (*i.e.*, assuming no MnSe quantum confinement at these diameters and no relaxation of confinement with Mn-Se addition to CdSe nanocrystals), then the excitonic blue shift in Fig. 5.3F implies a value of x_{Mn} ~ 0.14. Because of the increasing nanocrystal volume, this value is a lower limit, and is entirely consistent with the values determined in Fig 5.3E. For comparison with the absorption data, Fig. 5.3F also plots the room-temperature excitonic Zeeman splitting energies (ΔE_{Zeeman}) determined from analysis of the MCD intensities in Fig. 5.3B, plotted vs diffusion doping time. These data behave in essentially the same way as E_g. The fact that Mn^{2+} addition plateaus (Fig. 3E) but the spectroscopic effects of Mn^{2+} continue to increase (Fig. 5.3F) provide strong evidence for a mechanism involving initial Mn-Se deposition within an active surface volume, followed by slower homogenization of the $Cd_{1-x}Mn_xSe$ solid solution.

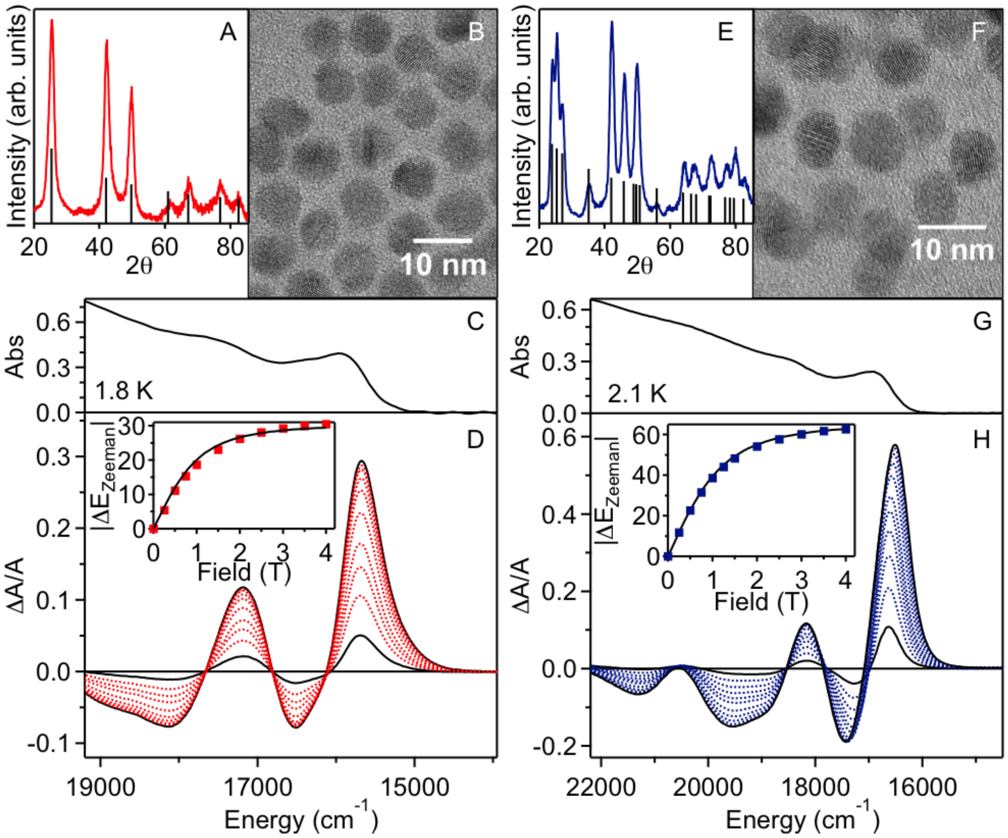

Fig. 5.4. **(**A) XRD and (B) TEM data for *d* = 8.8 ± 0.8 nm *zb*-$Cd_{1-x}Mn_xSe$ nanocrystal product obtained from diffusion doping of *d* = 8.4 nm *zb*-CdSe precursor nanocrystals for 30 min as in Fig. 1D. 1.8 K electronic absorption (C) and variable-field MCD (D) spectra of *d* = 8.4 nm *zb*-$Cd_{1-x}Mn_xSe$ nanocrystals. **(**E) XRD and (F) TEM data for *d* = 7.9 ± 0.5 nm *w*-$Cd_{1-x}Mn_xSe$ nanocrystal product obtained from diffusion doping of 6.8 nm *w*-CdSe seed nanocrystals. 2.1 K electronic absorption (G) and variable-field MCD (H) spectra of *d* = 6.0 nm *w*-$Cd_{1-x}Mn_xSe$ nanocrystals. The insets to (D) and (H) plot the excitonic Zeeman splittings vs magnetic field, deduced from the MCD spectra. The solid curves plot $S = 5/2$ Brillouin functions calculated using $g_{\mathrm{Mn}} = 2.0$ and the experimental temperatures. At saturation, $\Delta E_{\mathrm{Zeeman}}$ = -31 meV and -62 meV for these zinc blende and wurtzite $Cd_{1-x}Mn_xSe$ nanocrystals, respectively. The excitonic *g* values in the limit of small magnetic fields are g_{Exc} = -376 and -815 for the zinc blende and wurtzite $Cd_{1-x}Mn_xSe$ nanocrystals, respectively.

5.3.C Crystal structure retention

To test whether diffusion doping retains crystallographic phase, samples of predominantly hexagonal wurtzite (*w*) or cubic zinc blende (*zb*) CdSe nanocrystals were reacted with Mn^{2+} under identical conditions. The different crystal phases of these samples derive from different synthesis conditions, however under the identical diffusion doping reaction conditions both samples should have the same thermodynamically favored crystal phase. The fact that the nanocrystals retain their crystal structure while internally cations homogenize, is strong evidence that the anionic sublattice is rigid under these conditions.

Figure 4A-D shows data collected following 30 min of diffusion doping of d = 8.4 nm *zb*-CdSe seed nanocrystals under the same optimized conditions as in Fig. 2D. The TEM data of Fig. 4B show growth to d = 8.8 nm, and the XRD data of Fig. 5.4A show retention of the cubic lattice structure. Likewise, Fig. 5.4E-H show data collected following 60 min of diffusion doping of d = 6.8 nm *w*-CdSe seed nanocrystals under the same conditions. The TEM data of Fig. 5.4F show growth to d = 7.9 nm, and the XRD data of Fig. 4E show retention of the wurtzite lattice structure. From the XRD peak positions and bulk relationships between x_{Mn} and XRD peak positions, x_{Mn} values of 0.12 ± 0.02 and 0.19 ± 0.01 are estimated for the *zb* and *w* $\mathrm{Cd}_{1-x}\mathrm{Mn}_x\mathrm{Se}$ nanocrystals, respectively, consistent with the results of Fig. 3.[13]

5.3.D Nanocrystal shape retention

To test whether diffusion doping also retains nanocrystal shape, experiments were performed using anisotropic seed nanocrystals. Figure 5.5A shows TEM data of CdSe nanorods prepared by seeded growth and having d ~ 6-8 nm with ~6:1 aspect ratios and distinct bulges that are characteristic of nanorods prepared by the seeded growth method.[32] The shapes, sizes, and even the bulges of these nanorods are retained following 30 min of diffusion doping with Mn^{2+} at 300 °C under the optimized conditions of Fig. 5.2D, with successful doping confirmed by MCD spectroscopy. Combined, these results demonstrate diffusion doping as a new example of nanocrystal composition control without loss of crystallographic phase, size uniformity, or shape anisotropy, placing this method alongside cation exchange in these capacities.

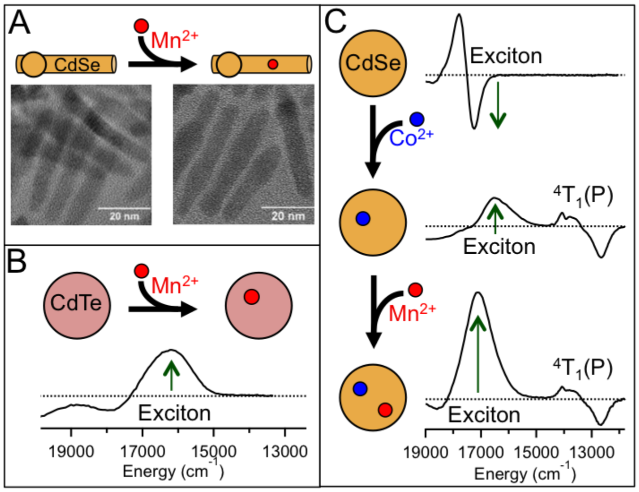

Figure 5.5. (A) Diffusion doping of seeded *w*-CdSe nanorods. TEM images collected before and after diffusion doping of seeded CdSe nanorods (*d* ~ 6-8 nm, aspect ratio ~ 6:1) with Mn^{2+} at 300 °C for 30 min. The nanorods retain their shapes. MCD spectra confirm doping (see Supporting Information). (B) MCD spectrum of CdTe nanocrystals after diffusion doping with Mn^{2+}, showing inversion of the excitonic MCD signal indicative of successful doping. (C) Tandem diffusion doping of *zb*-CdSe nanocrystals with Co^{2+} followed by Mn^{2+}. From top to bottom: (*top*) MCD of undoped CdSe precursor nanocrystals, (*middle*) MCD spectrum of the same nanocrystals after diffusion doping with Co^{2+}, showing inversion of the excitonic MCD signal and appearance of the characteristic Co^{2+} $^4T_1(P)$ *d-d* transition, (*bottom*) MCD spectrum of the same nanocrystals following diffusion doping with Mn^{2+}, showing increased excitonic Zeeman splitting and retention of the Co^{2+} $^4T_1(P)$ *d-d* transition.

5.4 Testing the limits

5.4.A Record sp-d exchange

Figures 5.4C,D and G,H plot low-temperature absorption and variable-field MCD spectra of these nanocrystals after diffusion doping. In both cases, the MCD signals are very strong and show the hallmark signatures of successful Mn^{2+} doping. Plots of ΔE_{Zeeman} vs magnetic field (insets) show the $S = 5/2$ saturation magnetization expected for $Cd_{1-x}Mn_xSe$. For the *zb*-$Cd_{1-x}Mn_xSe$ nanocrystals, ΔE_{Zeeman} saturates at -31 meV and $g_{Exc} = -376$ in the low-field limit (1.8 K). For the *w*-$Cd_{1-x}Mn_xSe$ nanocrystals, ΔE_{Zeeman} saturates at -62 meV, and $g_{Exc} = -815$ in the low-field limit (2.1 K), consistent with their greater x_{Mn}. The largest ΔE_{Zeeman} we have achieved using diffusion doping is $\Delta E_{\mathrm{Zeeman}}$ = -100 meV, with an extraordinarily large value of g_{Exc} = -907 at 1.8K.

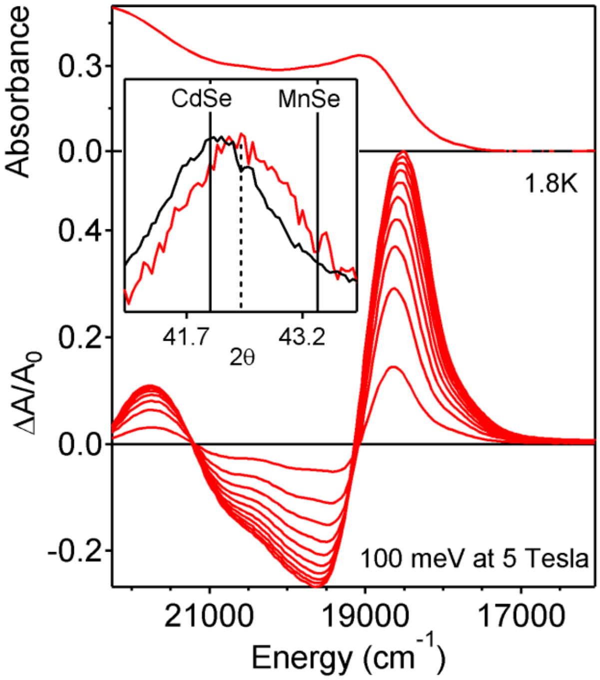

Figure 5.6. $Cd_{1-x}Mn_xSe$ nanocrystals made from diffusion doping of d = 3.5 nm CdSe core nanocrystals for 1 hr at 300 ºC. The g_{Exc} = -907 at 1.8 K, and $\Delta E_{\mathrm{Zeeman}}$ = 100 meV at saturation. The inset shows the 220 reflection of the XRD measured before (black) and after (red) Mn^{2+} incorporation. The magnitude of this shift corresponds to $x_{\mathrm{Mn}} = 0.29$.

This $\Delta E_{\mathrm{Zeeman}}$ value is close to the maximum of -120 meV anticipated from bulk *sp-d* exchange parameters and the maximum x_{eff} of ~3.3%.[41] Comparison with literature shows these to be the largest magneto-optical effects achieved for $Cd_{1-x}Mn_xSe$ nanocrystals of any type to date, for example exceeding the next largest $\Delta E_{\mathrm{Zeeman}}$ and g_{Exc} = -907 values by nearly a factor of two.[10,11] Such strong magneto-optical responses, and the magneto-electronic properties they report upon, constitute one of the main motivations for synthesis of this class of materials.

5.4.B. The first observation of sp-d exchange in Mn^{2+}:CdTe colloidal nanocrystals

Although the present work has focused primarily on optimization of reaction conditions for the benchmark $Cd_{1-x}Mn_xSe$ nanocrystal system, the principles underpinning the diffusion doping process described here are general, and the chemistry should therefore also be broadly generalizable. For example, by replacing CdSe nanocrystals and Se^{2-} with CdTe nanocrystals and Te^{2-}, decreasing the injection temperature to 170 °C, and adding a reductant (superhydride) to prevent Te^{2-} anions in solution from reducing the first potential oxidant and then bond with their own in a black powder at the bottom of the flask. successful synthesis of $Cd_{1-x}Mn_xTe$ nanocrystals was achieved (Fig. 5.5B) but without satisfactory suppression of Ostwald ripening, which is perhaps the revenge of Gustavo M. Dalpian's 2006 calculation, proclaiming that dopants will destroy the nanocrystals from within. In this case increased Ostwald ripening takes place as a corrolary to the increased dissolution rate of Mn^{2+}:CdTe nanocrystals. CdTe nanocrystals are notoriously unstable because Te^{2-} exposed on the surface can readily be oxidized and as it loses electrons its affinity for Cd^{2+} is replaced by affinity for other tellurides and if these are allowed to form crystals with sufficient surface area, CdTe nanocrystals are dissolved by this competing reaction. Presense of oxidizing agents such as oxygen drive this process forward, making ZnTe nanocrystals very air sensitive. Attempts to dope CdTe with Co^{2+}, consisted of nanocrystal growth, followed by nanocrystal dissolution. Ironically the softer Co^{2+} cation has always been a easier to dope than Mn^{2+} in Se^{2-} and S^{2-} based II-VI semiconductor nanocrystals. It is a possibility that Co^{2+} ability to diffuse into CdTe nanocrystals in large numbers, dissolves them.

5.4.C. Extension to Mn^{2+}:ZnSe and Mn^{2+}:CdS

Diffusion doping methods have been extended to both Mn^{2+}:ZnSe and Mn^{2+}:CdS, however the synthetic problems these materials have exhibited are of interest. Mn^{2+}:ZnSe ensembles undergo severe Ostwald ripening. Mn^{2+}:ZnSe nanocrystals are known to undergo rapid Ostwald ripening when the growth solution goes above 280°C, by those who have been making Mn^{2+}:ZnSe using the cluster synthesis. Further exploration also confirmed that S^{2-} and Se^{2-} are able to switch and dope Mn^{2+} into CdSe and CdS nanocrystals repsectively. Attempts to use Se^{2-} to dope Mn^{2+} into CdTe resulted in a complete loss of excitonic features by absorption.

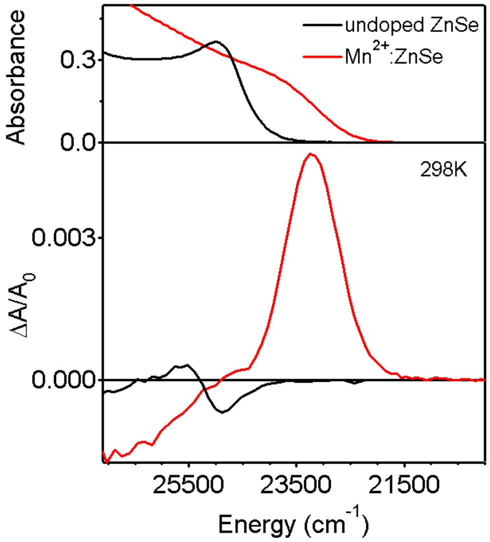

Figure 5.7. Room-temperature absorption and MCD spectra of $Zn_{1-x}Mn_xSe$ nanocrystals (red) prepared by diffusion doping of d = 4 nm ZnSe seed nanocrystals (black) for 30 min at 300 °C.

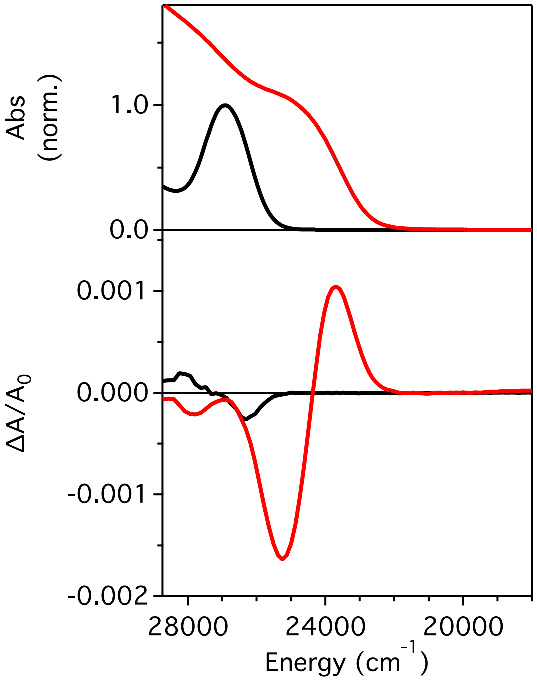

Figure 5.8. Room-temperature absorption and MCD spectra of $Cd_{1-x}Mn_xS$ nanocrystals (red) made by diffusion doping d = 2.6 nm CdS seed nanocrystals (black) with Mn^{2+}. Absorption spectra (top) before and after 60 min of diffusion doping at 300 ºC. MCD spectra (bottom) show g_{Exc} = +0.60 before diffusion doping, and -3.47 after doping.

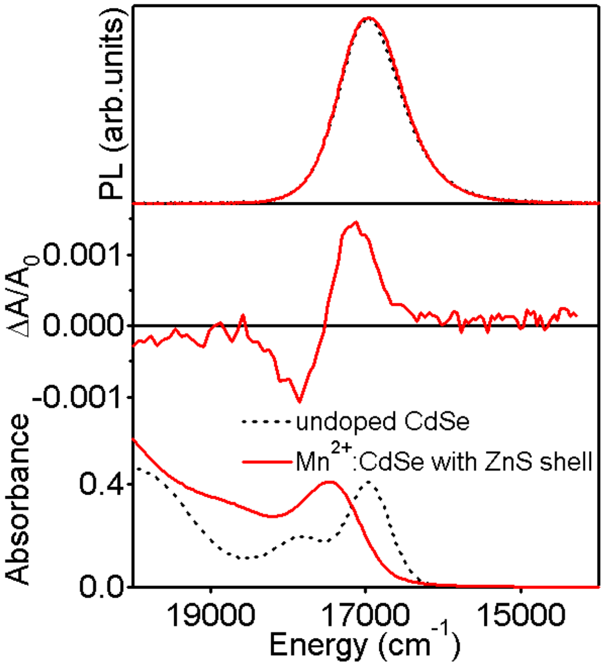

Figure 5.9. Room temperature absorbance of 4.1 nm diameter CdSe nanoparticles before(black) and after(red) 30 minutes at 300° C in the presence of Mn^{2+} and sulfur in place of selenium. The particles were washed and an eight monolayer ZnS shell was applied over 12 hours at 230° C. The absorbance is slightly blue shifted and broadened. Room temperature MCD of this sample gives an excitonic g value of -0.92, consistent with Mn^{2+} incorporation.

5.4.D. Sequencial and simultaneous doping with two different cations

The capacity to separate doping from nanocrystal synthesis introduces new opportunities to prepare doped nanostructures that would be difficult or impossible to obtain under kinetic trapping conditions. For example, previous work has shown that dopants are excluded from very small semiconductor nanocrystals under kinetic doping conditions.[8,42,43,46] Among other things, this behavior has complicated the analysis of the recently discovered intrinsic dual emission phenomenon in small $Cd_{1-x}Mn_xSe$ nanocrystals because of the coexistence of both doped and undoped nanocrystals.[47] To overcome this problem, $Cd_{1-x-y}Zn_xMn_ySe$ alloys and complex $Zn_{1-x}Mn_xSe$/CdSe and $Zn_{1-x}Mn_xSe$/ZnS/CdS/Zn nanocrystal heterostructures were developed.[48-50] By diffusion doping, we have now succeeded in reaching values of x_{Mn} in CdSe nanocrystals large enough to raise the energy of the excitonic states high enough in energy to show pronounced dual emission directly in $Cd_{1-x}Mn_xSe$ for the first time, without signal contamination from undoped nanocrystals.

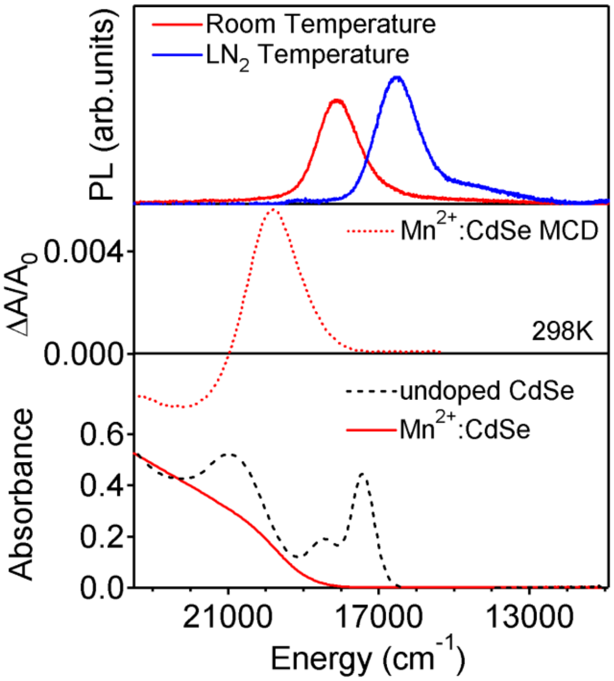

Figure 5.10. Room temperature absorbance of 3.6 nm diameter CdSe nanoparticles before(black) and after(red) 29 hours at 300° C in the presence of Mn^{2+}. The absorbance is significantly blue shifted and broadened. Room temperature emission is dominated by the excitonic feature. As the sample is submerged in liquid nitrogen, excitonic emission is quenched and replaced by Mn^{2+} $^4T_1$-> $^6A_1$ ligand field emission. Excitonic emission quenching and a large excitonic absorbance blue shift suggest that there is no undoped subset in this sample. Room temperature MCD gives g_{Exc} of -12.3, resulting from Mn^{2+} incorporation into the lattice.

We have also successfully added both Mn^{2+} and Zn^{2+} into seed CdSe nanocrystals in one simultaneous step, offering a convenient new way to achieve dual-emitting nanocrystals. Given the high Mn^{2+}, it is possible to grow ZnS shells at high temperatures without the possibility of creating an undoped subset. With this added synthetic flexebility it is now possible explore many more ways to create bright and stable nanocrystals.

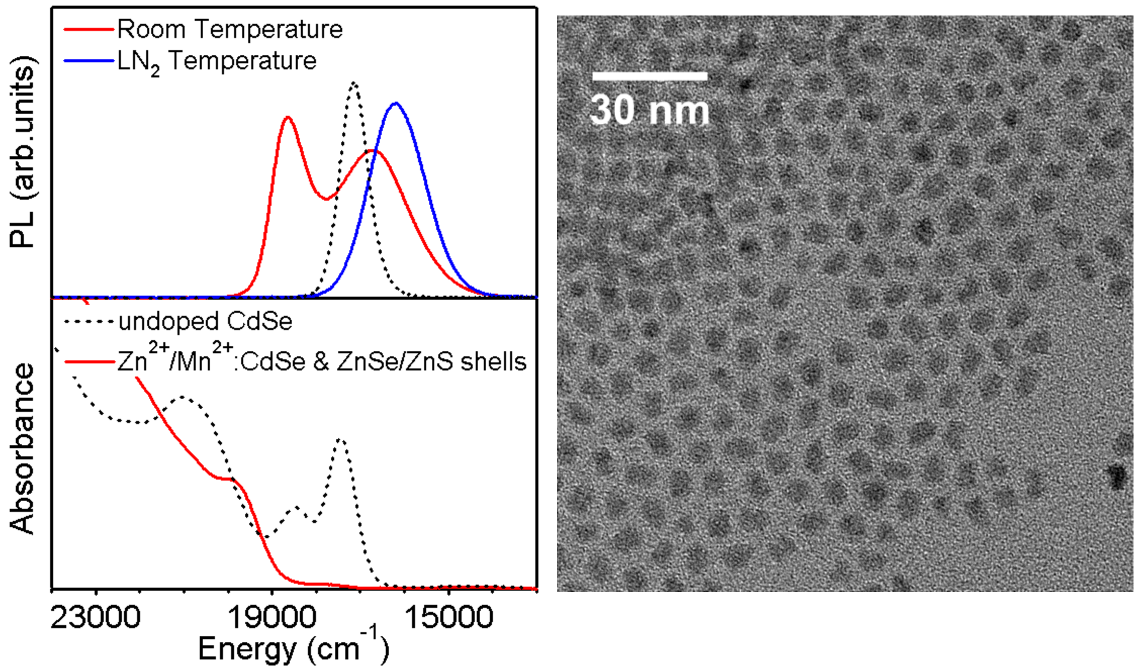

Figure 5.11. Room temperature absorbance and emission from 3.6 nm diameter CdSe nanoparticles before(black) and after(red) 30 minutes at 300° C in the presence of Zn^{2+} and Mn^{2+} in a 1:1 ratio. The particles are washed , a ZnSe shell is applied, followed by five monolayers of a ZnS shell applied at 300°C over five hours, to add stability and increase quantum yield. The absorbance is significantly blue shifted and broadened, as a result of dopant incorporation into the lattice. Room temperature emission exhibits both excitonic and Mn^{2+} $^4T_1$-> $^6A_1$ ligand field features. At liquid nitrogen temperature, excitonic emission is completely quenched, consistent with the absence of an undoped subset. The fact that a five hour 300° C shell growth did not lead to an undoped subset is consistent with a high initial Mn^{2+} concentration in the lattice. During the application of the ZnS shell at 300° C the emission was green, dominated by excitonic emission. Luminescence quantum yield remained high at 23% after being exposed to air for 6 months.

Furthermore, qualitatively new chemistries are now possible. For example, Fig. 5C shows excitonic MCD spectra of d = 3.8 nm CdSe seed nanocrystals that are doped sequentially by addition of Co^{2+} and then Mn^{2+}. The undoped CdSe nanocrystals show a negative leading-edge MCD intensity consistent with the absence of *sp-d* exchange. Diffusion doping with Co^{2+} for 30 min at 300 °C inverts the excitonic MCD signal and yields the characteristic Co^{2+} $^4A_2(F) \rightarrow {}^4T_1(P)$ MCD feature centered at 13370 cm^{-1}, confirming successful incorporation of Co^{2+} at the tetrahedral cation sites of the CdSe lattice.[37,38] After subsequent diffusion doping with Mn^{2+} for

40 min at 300 °C, the Co^{2+} $^4A_2(F) \rightarrow {}^4T_1(P)$ transition is retained and the excitonic MCD intensity is further increased. The ratio of excitonic to Co^{2+} ligand-field absorbance varies slowly during Mn^{2+} incorporation, indicating minimal loss of Co^{2+} during Mn^{2+} addition, consistent with the large difference between lattice and solution chemical potentials for all cations under these conditions.

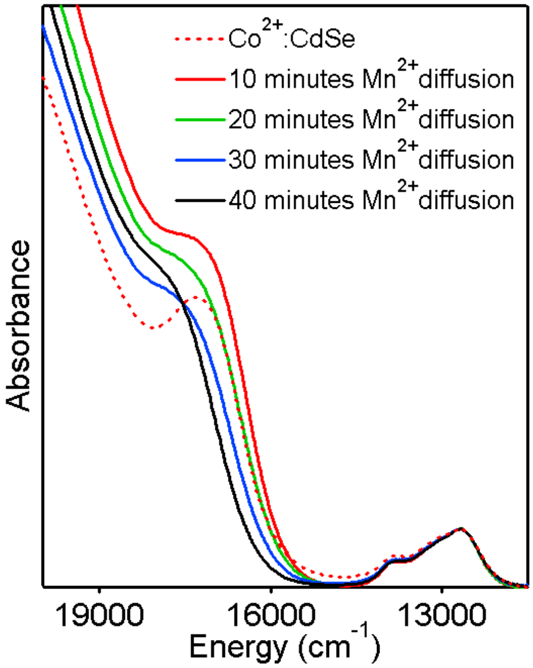

Figure 5.12. Room-temperature electronic absorption spectra collected during diffusion doping of Mn^{2+} into $Cd_{1-x}Co_xSe$ nanocrystals, themselves prepared by diffusion doping of Co^{2+} into CdSe nanocrystals (*i.e.*, the sequential tandem doping shown in Fig. 5C of the main text). Co^{2+} is initially diffused into $d = 4$ nm CdSe nanocrystals for 30 min at 300 °C. These $Cd_{1-x}Co_xSe$ nanocrystals are then infused with Mn^{2+} for 40 min at 300 °C. Aliquots were taken every 10 min.

5.4.E. Dopants that are either very hard or very soft Lewis acids

Hard Lewis acids such as Al^{3+}, Mg^{2+}, Gd^{3+}, and Er^{3+} were found cuase rapid precipitation of everything from solution, under conditions optimized for Mn^{2+} doping. The most likely explanation is catalysis of various reactions, such as amide formation between stearic acid and hexadecylamine, involving the activated carbonyl on the carboxylic acid Attempts to co-dope these ions simultaneously with Mn^{2+}, thereby using a lower concentration of the interfering ion, sacrificed the ability of Mn^{2+} to suppress Ostwald ripening, likely for the same reason. Extension of this method to these strong Lewis acids may be possible with identification of a suitable ligand set, preliminary results show that it is possible to keep the nanocrystals suspended longer by increasing the ligand concentration, this does lead to increased Ostwald ripening however.

On the other end of the spectrum, extension to soft Lewis acids such as Cu^{2+}, Cu^{+}, and Ag^{+} was not possible because of rapid formation of their respective selenide lattices separately from the CdSe nanocrystals. In the absense of added Se^{2-}, Cu^{+}/Mn^{2+} and Cu^{2+}/Mn^{2+} combinations had dratically different effects on CdSe nanocrystals. The attempt to initiate cation exchange between Cd^{2+} and Cu^{2+} with Mn^{2+} acting as an Ostwald ripening supressor, after 30 minutes had almost no effect on the excitonic absorption feature of these nanocrystals. The similar experiment with Cu^{2+} replace with Cu^{+} lead to rapid precipitation of black powerders that could not be resuspended.

5.4.F. Is Mn^{2+} special?

Replacing Mn^{2+} with excess Fe^{2+} without excess Se^{2-} was found to successfully preserve the absorption spectrum of the seed CdSe nanocrystals, precisely as with Mn^{2+} in Fig. 2B. Importantly, the nanocrystals also retain their excitonic photoluminescence. Fe^{2+} is a "killer trap" for luminescence in II-VI semiconductors, and this result thus indicates an absence of Fe^{2+} doping in the absence of excess Se^{2-} (as concluded for Mn^{2+} above). Addition of Se^{2-} to this reaction mixture leads to an increase in E_g with reaction time and complete quenching of the CdSe luminescence, consistent with successful Fe^{2+} incorporation. Fe^{2+} diffusion doping into

CdSe nanocrystals thus closely mirrors that of Mn^{2+}. Similarly, using Co^{2+} in place of Mn^{2+} allows the successful synthesis of $Cd_{1-x}Co_xSe$ nanocrystals with high Co^{2+} concentrations. Mn^{2+} is the weakest hard Lewis acid, this puts it in a position as the perfect mediator of ligands in solution. The fact that it is a hard Lewis acid makes the formation of MnSe and MnS crystals difficult makes the range of possible Mn^{2+} concentrtions larger than for softer cations, such as Fe^{2+} and Co^{2+}. Its weakness as a Lewis acid prevents it from catalyzing reactions that destroy ligand, leading to an evolution of reaction conditions that is difficult to control and reproduce. Perhaps most importantly its weakness gives an ensemble of Mn^{2+} cation in solution the ability to distribute in such a way that ligands are able to participate in other processes, such as suspension of nanocrystals in solution. A weak acid is a buffer.

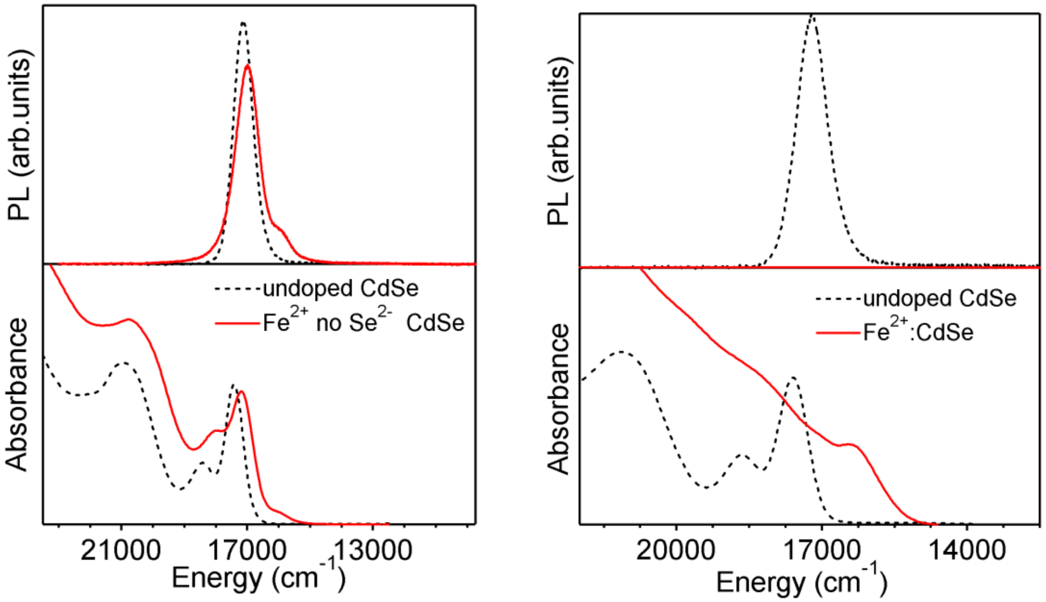

Figure 5.13. Room-temperature absorption and photoluminescence spectra of $d = 3.6$ nm CdSe nanocrystals before (black) and after (red) diffusion doping for 20 min at 300 °C in the presence of Fe^{2+}, a well-known "killer trap" for luminescence in II-VI semiconductors. **Left.** Data collected when diffusion doping was performed without additional Se^{2-}. The excitonic luminescence quantum yield is not affected appreciably, consistent with the absence of Fe^{2+} in the CdSe lattice. **Right.** Data collected when diffusion doping was performed in the presence of excess Se^{2-} (7:1 ratio to Cd^{2+} in nanocrystals). CdSe excitonic luminescence is quenched, consistent with Fe^{2+} incorporation.

5.5 Conclusion

We have described the development and demonstrated a successful synthesis of doped semiconductor nanocrystals that does not rely on accidental trapping of dopants. Instead the thermodynamic processes that have been behind intra and inter particle cation transfer, observed as self-purification, nanocrystal-solution cation exchange and rapid conversion of core/shells into homogeneous alloys, were understood, described and demonstrated through experiment. Simultaneous discovery that Ostwald ripening can be suppressed by relatively unreactive Mn^{2+} cations that attenuate the ability of ligands in solution to participate in cation transfer between separate nanoparticles, without disengaging them completely from various equilibria. This diffusion-doping method thus allows the nanocrystals to achieve their thermodynamic compositions without reaching their thermodynamically favored shapes, sizes, or crystallographic phases. Using this strategy, we have solved multiple long standing synthetic problems, such as fabrication of high-quality colloidal $Cd_{1-x}Mn_xSe$ nanocrystals that simultaneously display the narrowest size distributions, the highest values of x, and largest magneto-optical exciton splittings of any $Cd_{1-x}Mn_xSe$ nanocrystals reported to date. This success motivates the generalization of this strategy to synthesize nanocrystals of various other shapes and compositions under thermodynamic control, particularly compositions that do not involve the few well-known fast-diffusing ions that have dominated cation-exchange chemistries to date, and promising preliminary results for other nanocrystal compositions have been presented. Overall, these findings raise interesting possibilities for the development of new doped nanostructures with complex shapes and compositions, and may ultimately enable the advancement of new technologies involving this important class of materials.

5.6 Methods

5.6.A Experimental

Seed CdSe nanocrystals of different crystallographic phases, shapes, and sizes, as well as seed ZnSe, CdS, and CdTe nanocrystals, were all prepared by methods adapted from various literature sources[32-35] as described in detail in the Supporting Information. All nanocrystals have been capped with oleate prior to diffusion doping, but the complete exchange with the residual native ligands employed in the various syntheses is not assumed.

Diffusion doping of CdSe nanocrystals with Mn^{2+} was performed as follows: CdSe nanocrystals (~0.13 mmol in terms of CdSe units) were dried and added to 0.17 g (2.1 mmol) of selenium powder, 1 mL of ODE, and 1 mL of TBP in a septum-capped 5 mL round bottom flask in a nitrogen-atmosphere glovebox. Separately, 12 g of ODE, 0.5 g of SA and 1 g of HDA were added to a 100 mL 3-neck round bottom flask. Following heating of the latter solution for 30 min at 100 °C under vacuum, 0.03 g (0.1 mmol) of $Mn(OAc)_2•4H_2O$ was added against a nitrogen overpressure. The flask was then placed under vacuum to remove acetate and water, then heated under nitrogen to 300 °C, at which point the CdSe/selenide solution was injected rapidly. This reaction mixture was held at temperatures between 290 °C and 300 °C for between a few seconds and 29 hours. The reaction is aided by the greater activity of TBP than the more common TOP. As the solution was cooled to room temperature, 3 mL of toluene was added at ~120 °C to prevent SA solidification. Parallel experiments in which the samples were heated to only 200 °C failed to incorporate Mn^{2+} (see Supporting Information). The synthetic procedures for Co^{2+} or Fe^{2+} diffusion doping were identical, but with Co^{2+} added as $Co(OAc)_2•4H_2O$ or Fe^{2+} added as $Fe(SO)_4•7H_2O$.

Diffusion doping of CdTe nanocrystals with Mn^{2+} was performed as follows: 12 g of

ODE, 1 g of HDA, and 0.5 g of SA were added to a 100 mL 3-neck round bottom flask. The solution was degassed for 30 min under vacuum at 100 °C and brought back under nitrogen. Under a nitrogen overpressure, 0.03 g (0.1 mmol) of $Mn(OAc)_2 \cdot 4H_2O$ was added, followed by a brief pump/purge cycle, before the solution was heated to 170 °C for the nanocrystal injection. In a separate, septum-capped 5 mL round bottom flask, 0.32 g (2.5 mmol) of tellurium, 1 mL of TBP, 0.5 mL of 1M superhydride solution in THF, 1 mL of oleylamine, and CdTe (~0.1 mmol in terms of CdTe units) nanocrystals were mixed in a nitrogen atmosphere glovebox. This solution was injected into the Mn^{2+} solution at 170 °C and stirred for 30 min at this temperature.

All nanocrystals were washed using the same procedures: The nanocrystals were precipitated from solution by addition of ethanol, and washed by repeated suspensions in toluene and flocculation with ethanol. In some cases, TOPO, HDA, OA, or TOP were added to improve nanocrystal solubility.

5.6.B.Physical characterization

Room-temperature electronic absorption spectra were collected for colloidal toluene suspensions of nanocrystals in 0.1 cm path length cuvettes using a Cary 500 spectrophotometer (Varian). XRD data were collected from evaporated nanocrystal films on glass slides using a Bruker D8 Discover spectrometer at the UW nanotech user facility. TEM samples were prepared by submerging a 200 mesh copper grid (Ted Pella, Inc.) in a 1 μM colloidal suspension of nanocrystals in toluene and allowing this substrate to dry in air. TEM images were obtained on a FEI TECNAI F20, 200 kV microscope at the UW nanotech user facility. Nanocrystal sizes and size distributions were determined by analysis of the images of > 100 individual nanocrystals for each value reported. Relative atomic concentrations were obtained by analysis of dried nanocrystals digested in ultrapure nitric acid (EMD chemicals) using inductively coupled plasma atomic emission spectrometry (ICP-AES, Perkin Elmer). Room-temperature magnetic circular dichroism (MCD) spectra were collected on colloidal nanocrystal suspensions in a 0.1 cm pathlength cuvette placed in a 1.5 T electromagnet oriented in the Faraday configuration. Low-temperature absorption and MCD spectra were collected on nanocrystal films prepared by depositing dilute toluene suspensions between two quartz disks. These samples were placed in a superconducting magneto-optical cryostat (Cryo-Industries SMC–1659 OVT) oriented in the Faraday configuration. At helium temperature, each sample was screened for depolarization by matching the CD spectra of a chiral molecule placed before and after the sample. In all cases, depolarization was < 5%. Electronic absorption and MCD spectra were collected simultaneously using an Aviv 40DS spectropolarimeter. The differential absorption collected in the MCD experiment is reported as $\Delta A = A_L - A_R$, where A_L and A_R refer to the absorption of left and right circularly polarized photons in the sign convention of Piepho and Schatz.[36, 37]

5.7 References

1. Murray, C. B.; Norris, D. J.; Bawendi, M. G., *J. Am. Chem. Soc.* **1993,** *115*, 8706.
2. Alivisatos, A. P., *J. Phys. Chem.* **1996,** *100*, 13226.
3. Murray, C. B.; Kagan, C. R.; Bawendi, M. G., *Annu. Rev. Mater. Sci.* **2000,** *30*, 545.
4. Scholes, G. D., *Adv. Funct. Mater.* **2008,** *18*, 1157.
5. Klimov, V. I., *Semiconductor Quantum Dots*. 2010.
6. Rogach, A., *Semiconductor Nanocrystal Quantum Dots. Synthesis, Assembly, Spectroscopy and Applications*. Springer: Vienna, 2008.
7. Bryan, J. D.; Gamelin, D. R., *Prog. Inorg. Chem.* **2005,** *54*, 47.
8. Erwin, S. C.; Zu, L. J.; Haftel, M. I.; Efros, A. L.; Kennedy, T. A.; Norris, D. J., *Nature* **2005,** *436*, 91.
9. Norris, D. J.; Efros, A. L.; Erwin, S. C., *Science* **2008,** *319*, 1776.
10. Beaulac, R.; Archer, P. I.; Ochsenbein, S. T.; Gamelin, D. R., *Adv. Funct. Mater.* **2008,** *18*, 3873.
11. Beaulac, R.; Ochsenbein, S. T.; Gamelin, D. R., Colloidal Transition-Metal-Doped Quantum Dots. In *Semiconductor Quantum Dots*, 2nd ed.; Klimov, V. I., Ed. CRC Press: 2010; pp 397.
12. Buonsanti, R.; Milliron, D. J., *Chem. Mater.* **2013,** *25*, 1305.
13. Furdyna, J. K.; Kossut, J., *Diluted Magnetic Semiconductors*. Academic: N.Y., 1988; Vol. 25.
14. Son, D. H.; Hughes, S. M.; Yin, Y.; Alivisatos, A. P., *Science* **2004,** *306*, 1009.
15. Luther, J. M.; Zheng, H.; Sadtler, B.; Alivisatos, A. P., *J. Am. Chem. Soc* **2009,** *131*, 16851.
16. Jain, P. K.; Amirav, L.; Aloni, S.; Alivisatos, A. P., *J. Am. Chem. Soc* **2010,** *132*, 9997.
17. Casavola, M.; van Huis, M. A.; Bals, S.; Lambert, K.; Hens, Z.; Vanmaekelbergh, D., *Chem. Mater.* **2011,** *24*, 294.
18. Miszta, K.; Dorfs, D.; Genovese, A.; Kim, M. R.; Manna, L., *ACS Nano* **2011,** *5*, 7176.
19. Li, H.; Zanella, M.; Genovese, A.; Povia, M.; Falqui, A.; Giannini, C.; Manna, L., *Nano Letters* **2011,** *11*, 4964.
20. Rivest, J. B.; Jain, P. K., *Chem. Soc. Rev.* **2013,** *42*, 89.
21. Mokari, T.; Aharoni, A.; Popov, I.; Banin, U., *Angew. Chem.* **2006,** *45*, 8001.
22. Mocatta, D.; Cohen, G.; Schattner, J.; Millo, O.; Rabani, E.; Banin, U., *Science* **2011,** *332*, 77.
23. Sahu, A.; Kang, M. S.; Kompch, A.; Notthoff, C.; Wills, A. W.; Deng, D.; Winterer, M.; Frisbie, C. D.; Norris, D. J., *Nano Letters* **2012,** *12*, 2587.
24. Acharya, S.; Sarkar, S.; Pradhan, N., *J. Phys. Chem. C* **2013,** *117*, 6006.
25. Eilers, J.; Groeneveld, E.; Donega, C. D.; Meijerink, A., *J. Phys. Chem. Lett.* **2012,** *3*, 1663.
26. Hagen, K. S.; Stephan, D. W.; Holm, R. H., *Inorg. Chem.* **1982,** *21*, 3928.
27. Autissier, V.; Henderson, R. A., *Inorg. Chem.* **2008,** *47*, 6393.
28. Chen, D.; Viswanatha, R.; Ong, G. L.; Xie, R.; Balasubramaninan, M.; Peng, X., *J. Am. Chem. Soc.* **2009,** *131*, 9333.
29. Du, M.-H.; Erwin, S. C.; Efros, A. L., *Nano Lett.* **2008,** *8*, 2878.
30. Erwin, S. C., *Phys. Rev. B* **2010,** *81*, 235433.
31. Qu, L.; Peng, X., *J. Am. Chem. Soc* **2002,** *124*, 2049.
32. Carbone, L.; Nobile, C.; De Giorgi, M.; Della Sala, F.; Morello, G.; Pompa, P.; Hytch, M.; Snoeck, E.; Fiore, A.; Franchini, I. R.; Nadasan, M.; Silvestre, A. F.; Chiodo, L.; Kudera, S.; Cingolani, R.; Krahne, R.; Manna, L., *Nano Letters* **2007,** *7*, 2942.

33. Yu, W. W.; Qu, L.; Guo, W.; Peng, X., *Chem Mater.* **2003,** *15,* 2854.
34. Yu, W. W.; Peng, X., *Angew. Chem.* **2002,** *41*, 2368.
35. Piepho, S. B.; Schatz, P. N., *Group Theory in Spectroscopy with Applications to Magnetic Circular Dichroism*. Wiley: New York, U.S.A., 1983.
36. Beaulac, R.; Archer, P. I.; Liu, X.; Lee, S.; Salley, G. M.; Dobrowolska, M.; Furdyna, J. K.; Gamelin, D. R., *Nano Lett.* **2008,** *8*, 1197.
37. Archer, P. I.; Santangelo, S. A.; Gamelin, D. R., *Nano Lett.* **2007,** *7*, 1037.
38. Archer, P. I.; Santangelo, S. A.; Gamelin, D. R., *J. Am. Chem. Soc.* **2007,** *129*, 9808.
39. Furdyna, J. K., *J. Appl. Phys.* **1988,** *64*, R29.
40. Kuno, M.; Nirmal, M.; Bawendi, M. G.; Efros, A.; Rosen, M., *J. Chem. Phys.* **1998,** *108*, 4242.
41. Shapira, Y.; Foner, S.; Ridgley, D. H.; Dwight, K.; Wold, A., *Physical Review B* **1984,** *30*, 4021.
42. Schwartz, D. A.; Norberg, N. S.; Nguyen, Q. P.; Parker, J. M.; Gamelin, D. R., *J. Am. Chem. Soc.* **2003,** *125*, 13205.
43. Norberg, N. S.; Gamelin, D. R., *J. Appl. Phys.* **2005,** *99*, 08M104.
44. Beaulac, R.; Gamelin, D. R., *Phys. Rev. B* **2010,** *82*, 224401.
45. Beaulac, R.; Feng, Y.; May, J. W.; Badaeva, E.; Gamelin, D. R.; Li, X., *Phys. Rev. B* **2011,** *84*, 195324.
46. Bryan, J. D.; Schwartz, D. A.; Gamelin, D. R., *J. Nanosci. Nanotechnol.* **2005,** *5,* 1472.
47. Beaulac, R.; Archer, P. I.; van Rijssel, J.; Meijerink, A.; Gamelin, D. R., *Nano Lett.* **2008,** *8*, 2949.
48. Vlaskin, V. A.; Janßen, N.; van Rijssel, J.; Beaulac, R.; Gamelin, D. R., *Nano Lett.* **2010,** *10*, 3670.
49. McLaurin, E. J.; Vlaskin, V. A.; Gamelin, D. R., *J. Am. Chem. Soc* **2011,** *133,* 14978.
50. McLaurin, E. J.; Fataftah, M. S.; Gamelin, D. R., *Chem. Commun.* **2013,** *49*, 39.
51. Fedorov, V. A.; Ganshin, V. A.; Korkishko, Y. N., *phys. stat. sol. (a)* **1993,** *139*, 9.
52. Pradhan, N.; Peng, X., *J. Am. Chem. Soc.* **2007,** *129*, 3339.
53. Zhong, X.; Han, M.; Dong, Z.; White, T. J.; Knoll, W., *J. Am. Chem. Soc.* **2003,** *125,* 8589.
54. Larsson, L.-E., *Mat. Sci. Engin.* **1975,** *19*, 231.

Bibliography

Acharya, S.; Sarkar, S.; Pradhan, N., *J. Phys. Chem. C* **2013,** *117*, 6006.

Alivisatos, A. P., *J. Phys. Chem.* **1996,** *100*, 13226.

Alivisatos, A.P. *Science* 271, 933-937 (1996).

Ando, K., Yamada, Y., & Shakin, V.A. *Phys. Rev. B* **47**, 13462-13465 (1993).

Archer, P.I.; Santangelo, S.A.; Gamelin, D.R. *J. Am. Chem. Soc.* **2007**, *129*, 9808.

Archer, P.I.; Santangelo, S.A.; Gamelin, D.R. *Nano Lett.* **2007**, *7*, 1037.

Autissier, V.; Henderson, R. A., *Inorg. Chem.* **2008,** *47*, 6393.

Bacher, G., *Topics Appl. Phys.* **90**, 147-185 (2003).

Balet, L. P.; Ivanov, S. A.; Piryatinski, A.; Achermann, M.; Klimov,V. I. *Nano Letters.* **2004,** 4, 1485–1488.

Bawendi, M. **G.;** Kortan, A. R.; Steigerwald, M. L.; Brus, L. E**.** *J.Chem. Phys.* **1989**, 91, 7282.

Beaulac, R.; Archer, P.I.; Ochsenbein, S.T.; Gamelin, D.R. *Adv. Funct. Mater.* **2008,** 18, 3873.

Beaulac, R.; Schneider, L.; Archer, P. I.; Bacher, G.; Gamelin, D. R. *Science*, **2009**, *325*, 973-976.

Beaulac, R.; Archer, P. I.; van Rijssel, J.; Meijerink, A.; Gamelin, D. R. *Nano Letters*, **2008**, *8*, 2949-2953.

Beaulac, R., Ochsenbein, S.T., & Gamelin, D.R., Colloidal Transition-Metal-Doped Quantum Dots in *Semiconductor and Metal Nanocrystals (2nd edition)*, edited by V. I. Klimov (2009), pp. in press.

Beaulac, R.; Feng, Y.; May, J. W.; Badaeva, E.; Gamelin, D. R.; Li, X., *Phys. Rev. B* **2011,** *84*, 195324.

Bhargava, R. N., Gallagher, D., Hong, X. & Nurmikko, A. Phys. Rev. Lett. 72, 416–-419 (**1994**).

Blinowski, J., Kacman, P., & Dietl, T. *Mat. Res. Soc. Symp. Proc.* **690**, 109-114 (2002).

Bol, A.A. & Meijerink, A. *Phys. Rev. B* 58, R15997-R16000 (1998).

Bradshaw, L. R.; Hauser, A.; McLaurin, E. J.; Gamelin, D. R. J. Phys. Chem. C., 2012, 116, 9300

Brus, L. E. *Appl. Phys. A* **1991**,53,465.

Brus.L.E. *J. Phys. Chem.* **1986,** 90, 2555.

Bryan, J. D.; Gamelin, D.R. *Prog. Inorg. Chem.* **2005**, 54, 47-126.

Buonsanti, R.; Milliron, D. J., *Chem. Mater.* **2013,** *25*, 1305.

Bussian, D. A.; Crooker, S. A.; Yin, M.; Brynda, M.; Efros, Al. L.; Klimov, V. I. *Nat. Mater.* **2009**, 8, 35–40.

Cao, L., Zhang, J., Ren, S., & Huang, S. *Appl. Phys. Lett.* **80**, 4300-4302 (2002).

Carbone, L.; Nobile, C.; De Giorgi, M.; Della Sala, F.; Morello, G.; Pompa, P.; Hytch, M.; Snoeck, E.; Fiore, A.; Franchini, I. R.; Nadasan, M.; Silvestre, A. F.; Chiodo, L.; Kudera, S.; Cingolani, R.; Krahne, R.; Manna, L., *Nano Letters* **2007,** *7*, 2942.

Casavola, M.; van Huis, M. A.; Bals, S.; Lambert, K.; Hens, Z.; Vanmaekelbergh, D., *Chem. Mater.* **2011,** *24*, 294.

Chan, W. C. W.; Maxwell, D. J.; Gao, X. H.; Bailey, R. E.; Han, M. Y.; Nie, S. M. *Curr. Opin. Biotechnol.* **2002**, *13*, 40.

Chen, H.-Y., Chen, T.-Y., & Son, D.H. *J. Phys. Chem. C* 114, 4418–4423 (2010).

Chen, Y., Vela, J., Htoon, H., Casson, J.L., Werder, D.J., Bussian, D.A., Klimov, V.I., & Hollingsworth, J.A. *J. Am. Chem. Soc.* **130**, 5026-5027 (2008).

Chen, H.-S.; Lo, B.; Hwang, J.-Y.; Chang, G.-Y.; Chen, C.-M.; Tasi, S.-J.; Wang, S.-J. J. *J. Phys. Chem. B* **2004**, *108*, 17119.

Chen, D.; Viswanatha, R.; Ong, G. L.; Xie, R.; Balasubramaninan, M.; Peng, X., *J. Am. Chem. Soc.* **2009,** *131*, 9333.

Clausen, T.; Vanhardeveld, C.; Everts, M. E. *Physiol. Rev.* **1991**, *71*, 733.

Cumberland, S.L.; Hanif, K.M.; Javier, A.; Khitrov, G.A.; Strouse, G.F.; Woessner, S.M.; Yun, C.S. *Chem. Mater.*, 14, 1576-1584 (**2002**)

Dabbousi, B.O., Rodriguez-Viejo, J., Mikulec, F.V., Heine, J.R., Mattoussi, H., Ober, R., Jensen, K.F., & Bawendi, M.G. *J. Phys. Chem. B* **101**, 9463-9475 (1997).

Dance, I. G.; Choy, A.; Scudder, M. L. J. Am. Chem. Soc. **1984**, 106, 6285-6295.
Dong Hee Son, Steven M. Hughes, Yadong Yin, A. Paul Alivisatos. Science **2004**, 306 1009-1012.

Darwent B.B., National Standard Reference Data Series, NationalBureau of Standards, no. 31, Washington, 1970.

Dietl, T. *J. Mag. Mag. Mater*. **272-276**, 1969–1973 (2004).

Dreyhsig, J. *J. Phys. Chem. Solids* **59**, 31-42 (1998).

Du, M.-H.; Erwin, S. C.; Efros, A. L., *Nano Lett.* **2008,** *8*, 2878.

Efros, A.L. *Phys. Rev. B* **46**, 7448-7458 (1992).

Ehlert, A., Dreyhsig, J., Gumlich, H.-E., & Allen, J.W. *J. Lumin.* **60-61**, 21-25 (1994).

Eilers, J.; Groeneveld, E.; Donega, C. D.; Meijerink, A., *J. Phys. Chem. Lett.* **2012,** *3*, 1663.

Embden, J.; Jasieniak, J.; Gómez D. E.;Mulvaney, P.; Michael Giersig, M.Aust. J. Chem. 2007, 60, 457–471.

Erwin, S.C., Zu, L.J., Haftel, M.I., Efros, A.L., Kennedy, T.A., & Norris, D.J., *Nature* **2005** 436, 91-94.

Erwin, S. C., *Phys. Rev. B* **2010,** *81*, 235433.

Fedorov, V. A.; Ganshin, V. A.; Korkishko, Y. N., *phys. stat. sol. (a)* **1993,** *139*, 9.

Fiore A. et. al., *J. Am. Chem. Soc.* **2009**, *131*, 2274–2282.

Furdyna, J. K.; Kossut, J. *Semiconductors and Semimetals*; Academic: New York, **1988**; Vol. 25.

García-Santamaría, F., Chen, Y., Vela, J., Schaller, R.D., Hollingsworth, J.A., & Klimov, V.I. *Nano Lett.*, ASAP (DOI:10.1021/nl901681d) (2009).

Garcia-Rodriguez, R.; Liu, H. *J. Am. Chem. Soc.* **2012**, 134, 1400−1403.

Gosse, C.; Bergaud, C.; Low, P. *Topics in Applied Physics*; Springer-Verlag Berlin: Berlin, 2009; Vol. 118, p 301.

Groeneveld, E. et. al., *ACS NANO,* **2013**, 7, 7913-7930.

Gustavo M. Dalpian and James R. Chelikowsky Phys. Rev. Lett. **2006**, 96, 226802.

Gustavo M. Dalpian and James R. Chelikowsky Phys. Rev. Lett. **2008**, 100, 179703.

Hagen, K. S.; Stephan, D. W.; Holm, R. H., *Inorg. Chem.* **1982,** *21*, 3928.

Han, B.; Hanson, W. L.; Bensalah, K.; Tuncel, A.; Stern, J. M.; Cadeddu, J. A. *Ann. Biomed. Eng.* **2009**, *37*, 1230.

Haus, J.W., Zhou, H.S., Honma, I., & Komiyama, H. *Phys. Rev. B* **47**, 1359-1365 (1993).

Heinrich, H. & Langer, J.M., Band Offsets in Heterostructures in *Advances in Solid State Physics*, edited by P. Grosse (Springer, Berlin, 1986), Vol. 26, pp. 251-275.

Hines, M.A. & Guyot-Sionnest, P. *J. Phys. Chem.* **100**, 468-471 (1996).

Hoffman, D.M.; Meyer, B.K.; Ekimov, A.I.; Merkulov, I.A.; Efros, A.L.; Rosen, M.; Counio, G.; Gacoin, T.; Boilot, J.-P. Sol. State Comm. **2000**, 114, 547.

Ithurria, S., Guyot-Sionnest, P., Mahler, B., & Dubertret, B. *Phys. Rev. Lett.* **99**, 265501 (2007).

Ivanov, S. A.; Piryatinski, A.; Nanda, J.; Tretiak, S.; Zavadil, K. R.; Wallace, W. O.; Werder, D.; Klimov, V. I. *J. Am. Chem. Soc.* **2007**, 129, 11708.

Ivanov, S.A., Nanda, J., Piryatinski, A., Achermann, M., Balet, L.P., Bezel, I.V., Anikeeva, P.O., Tretiak, S., & Klimov, V.I. *J. Phys. Chem. B* **108**, 10625-10630 (2004).

Jain, P. K.; Amirav, L.; Aloni, S.; Alivisatos, A. P., *J. Am. Chem. Soc* **2010,** *132*, 9997.

Kacman, P. *Semicond. Sci. Technol.* **16**, R25-R39 (2001).

Kim, S.; Fisher, B.; Eisler, H.J.; Bawendi, M. *J. Am. Chem. Soc.***2003,** 125, 11466.

Klimov, V. I., *Semiconductor Quantum Dots*. 2010.

Kuno, M.; Nirmal, M.; Bawendi, M. G.; Efros, A.; Rosen, M., *J. Chem. Phys.* **1998,** *108*, 4242.

Larsson, L.-E., *Mat. Sci. Engin.* **1975,** *19*, 231.

Li, H.; Zanella, M.; Genovese, A.; Povia, M.; Falqui, A.; Giannini, C.; Manna, L., *Nano Letters* **2011,** *11*, 4964.

Li, J. J.; Wang, Y. A.; Guo, W.; Keay, J. C.; Mishima, T. D.; Johnson, M. B.; Peng, X. *J. Am. Chem. Soc.* **2003**, *125*, 12567.

Lou, J. F.; Hatton, T. A.; Laibinis, P. E. *Anal. Chem.* **1997**, *69*, 1262.

Louie, A. *Chem. Rev.* **2010**, *110*, 3146.

Lovingood, D.D., et. al. *J. Am. Chem. Soc.* **2008,** 130, 17004-11.

Ludwig, G.W. & Woodbury, H.H., in *Solid State Physics*, edited by F. Seitz & D. Turnbull (Academic Press, New York, 1962), Vol. 13, pp. 298.

Luther, J. M.; Zheng, H.; Sadtler, B.; Alivisatos, A. P., *J. Am. Chem. Soc* **2009,** *131*, 16851.

Mahler, B., Spinicelli, P., Buil, S., Quelin, X., Hermier, J.-P., & Dubertret, B. *Nature Mater.* **7**, 659-664 (2008).

Magana, D.; Perera, S. C.; Harter, A. G.; Dalal, N. S.; Strouse, G. F. J. Am. Chem. Soc. **2006**, 128, 2931-2939.

McCabe, K. M.; Hernandez, M. *Pediatr. Res.* **2010**, *67*, 469.

McLaurin, E. J.; Vlaskin, V. A.; Gamelin, D. R., *J. Am. Chem. Soc* **2011,** *133*, 14978.

McLaurin, E. J.; Fataftah, M. S.; Gamelin, D. R., *Chem. Commun.* **2013,** *49*, 39.

Medintz, I. L.; Uyeda, H. T.; Goldman, E. R.; Mattoussi, H. *Nat. Mater.* **2005**, *4*, 435.

Merkulov, I.A., Yakovlev, D.R., Keller, A., Ossau, W., Geurts, J., Waag, A., Landwehr, G., Karczewski, G., Wojtowicz, T., & Kossut, J. *Phys. Rev. Lett.* **83** (7), 1431-1434 (1999).

Mikulec, F.V.; Kuno, M.; Bennati, M.; Hall, D.A.; Griffin, R.G.; Bawendi, M.G. J. Am.Chem. Soc. **2000**, 122, 2532.

Miszta, K.; Dorfs, D.; Genovese, A.; Kim, M. R.; Manna, L., *ACS Nano* **2011,** *5*, 7176.

Mocatta, D.; Cohen, G.; Schattner, J.; Millo, O.; Rabani, E.; Banin, U., *Science* **2011,** *332*, 77.

Mokari, T.; Aharoni, A.; Popov, I.; Banin, U., *Angew. Chem.* **2006,** *45*, 8001.

Mornet, S.; Vasseur, S.; Grasset, F.; Duguet, E. *J. Mater. Chem.* **2004**, *14*, 2161.

Munro, A. M.; Jen-La Plante, I.; Ng, M. S.; Ginger, D. S. *J. Phys. Chem. C* **2007**, *111*, 6220.

Murphy, K. P.; Freire, E. *Adv. Protein Chem.* **1992**, *43*, 313.

Murray, C. B.; Norris, D. J.; Bawendi, M. G., *J. Am. Chem. Soc.* **1993,** *115*, 8706.

Murray, C. B.; Kagan, C. R.; Bawendi, M. G., *Annu. Rev. Mater. Sci.* **2000,** *30*, 545.

Nanda, J., Ivanov, S.A., Htoon, H., Bezel, I., Piryatinski, A., Tretiak, S., & Klimov, V.I. *J. Appl. Phys.* **99**, 034309 (2006).

Noras, J.M., Szawelska, H.R., & Allen, J.W. *J. Phys. C* **14**, 3255-3268 (1981).

Norberg, N. S.; Gamelin, D. R., *J. Appl. Phys.* **2005,** *99*, 08M104.

Norberg, N.S., Dalpian, G.M., Chelikowsky, J.R., & Gamelin, D.R. *Nano Lett.* **6**, 2887-2892 (2006).

Norberg, N.S., Parks, G.L., Salley, G.M., & Gamelin, D.R. *J. Am. Chem. Soc.* **128**, 13195-13203 (2006).

Norris, D. J.; Efros, A. L.; Erwin, S. C., *Science* **2008,** *319*, 1776.

Nose, K.; Fujita, H.; Omata, T.; Otsuka-Yao-Matsuo, S.; Nakamura, H.; Maeda, H. *J. Lumin.* **2007**, *126*, 21.

Pandey, A. & Guyot-Sionnest, P. *Science* **322**, 929-932 (2008).

Patrick T. K. Chin, Jan W. Stouwdam, and Rene A. J. Janssen. *Nano Lett.* **2007,** *7*, 1037.

Peng, X., Schlamp, M.C., Kadavanich, A.V., & Alivisatos, A.P. *J. Am. Chem. Soc.* **119**, 7019-7029 (1997).

Peng, Z.A.; Peng, X. *J. Am. Chem. Soc.* **2001**, 123, 183.

Piepho, S. B.; Schatz, P. N., *Group Theory in Spectroscopy with Applications to Magnetic Circular Dichroism*. Wiley: New York, U.S.A., 1983.

Pilla, V.; Alves, L. P.; Munin, E.; Pacheco, M. T. T. *Opt. Commun.* **2007**, *280*, 225.

Piryatinski, A., Ivanov, S.A., Tretiak, S., & Klimov, V.I. *Nano Lett.* **7**, 108-115 (2007).

Pradhan, N.; Peng, X., *J. Am. Chem. Soc.* **2007,** *129*, 3339.

Pradhan, N., Goorskey, D., Thessing, J., & Peng, X. *J. Am. Chem. Soc.* **127**, 17586-17587 (2005).

Qu, L.; Peng, X., *J. Am. Chem. Soc* **2002,** *124*, 2049.

Quan, Z., Wang, Z., Yang, P., Lin, J., & Fang, J. *Inorg. Chem.* **46**, 1354-1360 (2007).

Radovanovic, P. V.; Gamelin, D. R *J. Am. Chem. Soc.*, **2001**, *123*, 12207-12214.

Radovanovic, P. V.; Gamelin, D. R. Proc. SPIE-Int. Soc. Opt. Eng., **2002**, 4809, 51-61.

Radovanovic, P.V., Norberg, N.S., McNally, K.E., & Gamelin, D.R. *J. Am. Chem. Soc.* **124**, 15192-15193 (2002).

Reiss, P.; Protiere, M.; Li, L. *Small* **2009**, *5*, 154.

Rivest, J. B.; Jain, P. K., *Chem. Soc. Rev.* **2013,** *42*, 89.

Robbins, D.J., Dean, P.J., Glasper, J.L., & Bishop, S.G. *Solid State Comm.* **36** (1), 61-67 (1980).

Rogach, A. L.; Nagesha, D.; Ostrander, J. W.; Giersig, M.; Kotov, N. A. *Chem. Mater.* **2000**, *12*, 2676.

Rogach, A., *Semiconductor Nanocrystal Quantum Dots. Synthesis, Assembly, Spectroscopy and Applications*. Springer: Vienna, 2008.

Ross, D.; Gaitan, M.; Locascio, L. E. *Anal. Chem.* **2001**, *73*, 4117.

Sahu, A.; Kang, M. S.; Kompch, A.; Notthoff, C.; Wills, A. W.; Deng, D.; Winterer, M.; Frisbie, C. D.; Norris, D. J., *Nano Letters* **2012,** *12*, 2587.

Santangelo, S. A.; Hinds, E. A.; Vlaskin, V. A.; Archer, P. I.; Gamelin, D. R. J. Am. Chem. Soc., **2007**, 129, 3973-3978.

Sapareto, S. A.; Dewey, W. C. *Int. J. Radiat. Oncol. Biol. Phys.* **1984**, *10*, 787.

Scholes, G. D., *Adv. Funct. Mater.* **2008,** *18*, 1157.

Schrum, K. F.; Williams, A. M.; Haerther, S. A.; Benamotz, D. *Anal. Chem.* **1994**, *66*, 2788.

Schwartz, D. A.; Norberg, N. S.; Nguyen, Q. P.; Parker, J. M.; Gamelin, D. R., *J. Am. Chem. Soc.* **2003,** *125*, 13205.

Shapira, Y.; Foner, S.; Ridgley, D. H.; Dwight, K.; Wold, A., *Physical Review B* **1984,** *30*, 4021.

Sokolov, V.I., Surkova, T.P., Kulakov, M.P., & Fadeev, A.V. *Phys. Stat. Solidi (b)* **130** (1), 267-272 (1985).

Son, D. H.; Hughes, S. M.; Yin, Y.; Alivisatos, A. P., *Science* **2004,** *306*, 1009.

Stern, N.P., Myers, R.C., Poggio, M., Gossard, A.C., & Awschalom, D.D. *Phys. Rev. B* **75**, 045329 (2007).

Suyver, J. F., Wuister, S. F., Kelly, J. J. & Meijerink, A. Phys. Chem. Chem. Phys. 2, 5445–-5448 (**2000**).

Talapin, D. V.; Rogach, A. L.; Kornowski, A.; Haase, M.; Weller, H. *Nano Letters,* **2001,** 1, 207.

Talapin D.V., et al., *Nano Letters.* **2003**, 3, 1677.

Talapin, D. V.; Nelson, J. H.; Shevchenko, E. V.; Aloni, S.; Sadtler, B.; Alivisatos, A. P. *Nano Letters.* **2007**, 7, 2951–2959.

Thakar, R., Chen, Y., & Snee, P.T. *Nano Lett.* **7**, 3429-3432 (2007).

Uchiyama, S.; de Silva, A. P.; Iwai, K. *J. Chem. Ed.* **2006**, *83*, 720.

Vlaskin, V. A., Beaulac, R., & Gamelin, D.R. *Nano Lett.* 9, 4376-4382 (2009).

Vlaskin, V. A.; Janßens, N.; van Rijssel, J.; Beaulac, R.; Gamelin, D. R., *Nano Lett.* **2010,** *10*, 3670.

Vlaskin, V. A.; Barrows, C. J.; Erickson, C. S.; Gamelin, D. R. *J. Am. Chem. Soc.*, **2013**, *135*, 14380-14389.

Walker, G.; Sundar, V.; Rudzinski, C.; Wun, A.; Bawendi, M.; Nocera, D. *App. Phys. Lett.* **2003**, *83*, 3555.

Wang, S., Jarrett, B.R., Kauzlarich, S.M., & Louie, A.Y. *J. Am. Chem. Soc.* **129**, 3848-3856 (2007).

Wang, S. P.; Westcott, S.; Chen, W. *J. Phys. Chem. B* **2002**, *106*, 11203.

Wood, V., Halpert, J.E., Panzer, M.J., Bawendi, M.G., & Bulović, V. *Nano Lett.* **9**, 2367–2371 (2009).

Wu, X. Y.; Liu, H. J.; Liu, J. Q.; Haley, K. N.; Treadway, J. A.; Larson, J. P.; Ge, N. F.; Peale, F.; Bruchez, M. P. *Nat. Biotechnol.* **2003**, *21*, 41.

Yang, Y., Chen, O., Angerhofer, A., & Cao, Y.C. *J. Am. Chem. Soc.* **130**, 15649–15661 (2008).

Yang, H. & Holloway, P.H. *J. Phys. Chem. B* **107**, 9705-9710 (2003).

Yang, H. & Holloway, P.H. *Adv. Funct. Mater.* **14**, 152-156 (2004).

Yu, W. W.; Qu, L.; Guo, W.; Peng, X., *Chem Mater.* **2003,** *15*, 2854.

Yu, W. W.; Peng, X., *Angew. Chem.* **2002,** *41*, 2368.

Yu, Z.G., Guo, L., Du, H., Krauss, T., & Silcox, J. *Nano Lett.* **5**, 565-570 (2005).

Zhang, C. S.; Xing, D. *Nucleic Acids Res.* **2007**, *35*, 4223.

Zhong, X.; Han, M.; Dong, Z.; White, T. J.; Knoll, W., *J. Am. Chem. Soc.* **2003,** *125*, 8589.

Zhong, H.; Scholes G. D. *J. Am. Chem. Soc.* **2009.** 131, 26, 9171.

Zhong, X.; Feng, Y.; Zhang, Y.; Gu, Z.; Zou, L. *Nanotechnology*, **2007**, 18, 385606.

Zhong, X., Xie, R., Zhang, Y., Basché, T., & Knoll, W. *Chem. Mater.* **17**, 4038-4042 (2005).